

MEASUREMENT OF SM ELECTRO-WEAK PARAMETERS IN REACTOR  
ANTINEUTRINO-ELECTRON SCATTERING IN TEXONO EXPERIMENT

A THESIS SUBMITTED TO  
THE GRADUATE SCHOOL OF NATURAL AND APPLIED SCIENCES  
OF  
MIDDLE EAST TECHNICAL UNIVERSITY

BY

MUHAMMED DENİZ

IN PARTIAL FULFILLMENT OF THE REQUIREMENTS  
FOR  
THE DEGREE OF DOCTOR OF PHILOSOPHY  
IN  
PHYSICS

MAY 2007

Approval of the Graduate School of Natural and Applied Sciences.

---

Prof. Dr. Canan Özgen  
Director

I certify that this thesis satisfies all the requirements as a thesis for the degree of Doctor of Philosophy.

---

Prof. Dr. Sinan Bilikmen  
Head of Department

This is to certify that we have read this thesis and that in our opinion it is fully adequate, in scope and quality, as a thesis for the degree of Doctor of Philosophy.

---

Assoc. Prof. Dr. Meltem  
Serin  
Supervisor

Examining Committee Members

Prof. Dr. Henry Tsz-King Wong

Assoc. Prof. Dr. Meltem Serin

Prof. Dr. Li Jin

Prof. Dr. A. Ulvi Yilmazer

Prof. Dr. Mehmet T. Zeyrek

“I hereby declare that all information in this document has been obtained and presented in accordance with academic rules and ethical conduct. I also declare that, as required by these rules and conduct, I have fully cited and referenced all material and results that are not original to this work.”

Name, Last name : MUHAMMED DENİZ

Signature :

## ABSTRACT

### MEASUREMENT OF SM ELECTRO-WEAK PARAMETERS IN REACTOR ANTINEUTRINO-ELECTRON SCATTERING IN TEXONO EXPERIMENT

DENİZ, MUHAMMED

Ph.D., Department of Physics

Supervisor: Assoc. Prof. Dr. Meltem Serin

May 2007, 156 pages.

In this thesis a search for  $\bar{\nu}_e - e^-$  scattering cross-section and Weinberg Angle measurements were performed at KS Nuclear Power Station with 200 kg CsI(Tl) scintillating crystal detector located at a distance of 28 m from the 2.9 GW reactor core giving total flux of  $6.52 \times 10^{12} \text{ cm}^{-2}\text{s}^{-1}$  in average at the experimental site. New analysis techniques and background suppression methods were developed. In the region of  $3 - 8 \text{ MeV}$  a measurement of SM cross section of  $(1.235 \pm 0.577) \times R_{SM}$  and Weinberg Angle of  $0.264 \pm 0.075$  which is quite consistent with the SM value of  $0.23120(15)$  [1] were obtained. These are the best results with world wide level sensitivities at untested low energy region by using reactor anti-neutrinos.

Keywords: Neutrino, Weinberg Angle, CsI(Tl) Scintillating Crystal, TEXONO.

## ÖZ

### SM ELEKTRO-ZAYIF PARAMETRELERİN TEXONO DENEYİNDE REAKTÖR ANTİNÖTRİNO-SU-ELEKTRON SAÇILIMINDAN ÖLÇÜLMESİ

DENİZ, MUHAMMED

Doktora , Fizik Bölümü

Tez Yöneticisi: Doç. Dr. Meltem Serin

Mayıs 2007, 156 sayfa.

Bu tezde  $\bar{\nu}_e - e^-$  saçılım tesir kesitini ve Weinberg açını ölçmek için KS de bulunan 200 kg CsI(Tl) kristal detektörü ile yapılan araştırma anlatılmıştır. CsI(Tl) kristal detektörü 2.9 GW gücündeki reaktör çekirdeğinden 28 m uzaklıkta yerleştirilmiştir ve deney setindeki ortalama nötrino flux  $6.52 \times 10^{12} \text{ cm}^{-2} \text{ s}^{-1}$  dir. Yeni analiz metodları ve arka plan gürültü bastırma çalışmaları geliştirildi. SM saçılım tesir kesiti  $3 - 8 \text{ MeV}$  enerji aralığında  $(1.207 \pm 0.577) \times R_{SM}$  ve Weinberg açısı  $0.260 \pm 0.076$  olarak ölçülmüştür. Bu değer SM değeri 0.23120(15) ile çok uyumludur[1]. Bu değerlerle reaktör nötrinosu ile test edilmemiş düşük enerjilerde dünya çapında en iyi hassasiyet ölçüm seviyesine ulaşılmıştır.

Anahtar Kelimeler: Nötrino, Weinberg Açısı, CsI(Tl) sintilasyon kristal detektörü, TEXONO.

*DEDICTED TO MY FAMILY*

## ACKNOWLEDGMENTS

I want to thank Prof. Dr. Henry Tsz-King Wong for accepting me to study in the TEXONO Experiment at Academia Sinica and also for continuous support, great interest and profound guidance throughout this research. I would like to thank him for helpful and delightful discussions and also for his useful suggestions. He always shed light to the unsolved and challenging problems to show the correct path and push me always forward.

I am thankful to National Science Council (NSC) and Academia Sinica Institute of Physics for the funding support for three years during this research.

I am thankful to Prof. Dr. Mehmet Zeyrek for leading me to study in the TEXONO Experiment and for his useful suggestions. He always lead me challenging and enjoable unsolved questions. I want to thank Prof. Dr. Perihan Tolun for leading and supporting me to study neutrino physics. I would like to thank Assoc. Prof. Dr. Meltem Serin for her invaluable and intense help. As my supervisor she always helped me kindly and solved my problems wisely. I am thankful to Prof. Dr. Ali Ulvi Yilmazer for his kind interest and his comments on this study.

I would like to thank Prof. Dr. Li Jin for useful discussions and sharing his experience with me and also for inviting me to China and introducing IHEP with great hospitality.

I would like to thank our group secretary Ms. Cherie Chang for her hospitality and her help in all documentations. Thank her for solving my problems

with great kindness and making my life easier and more colourful in Taiwan.

Also I want to thank all members of the TEXONO and High Energy Physics Group as my friend, especially Li Hau Bin, Liao Heng Yi, Lin Shih Kai, Venkatesh Singh, Chang Hsi Ming, Don Ke Jun, Fan Bin Bin, Won Han Shawn, Wang You Ren, Zhu Yue Feng, and all people who treat me friendly to make my life easier and more enjoyable in Taiwan. I would like to thank Chou Mu Han for his friendship and nice figures of Power Plant and sheilding, and Wu Shih Chiang for his help to understand DAQ system. I am very thankfull to Lin Chung Wei, Wong Yui Jen, Lin Feng Kai for their help in making calibration. My special thanks go to Dr. Lin Shin Ted for his suggestions and great help in this work.

I would like to thank my friends, especially Rıza Kandemir, Cem Hayırlı, Özlem Pehlivan, Damla Şendoğdu for their support despite of the distance. Also I want to thank my friends in Taiwan Dr. Imameddin Amiraslan, Dr. Famil Veliyev and Dr. Riyayet Ismailof for their companionship and moral support to make my life very colourful and enjoyable in Taiwan. I would like to thank them for their sweet and educational discussions. I am also very thankful to Wong Chien-Huan, Wong Chien-Hsaing and Wong Ming-Der for their hospitality and friendship.

Finally, I offer sincere thanks to my family especially my wife Güliz for their great support and encouragement. Each of them supports me very kindly and sincerely, and give me strength with their love and passion. Thanks a lot to each member of my family for their supports in any condition.



## TABLE OF CONTENTS

ABSTRACT . . . . .	iv
ÖZ . . . . .	v
DEDICATION . . . . .	vi
ACKNOWLEDGMENTS . . . . .	vi
TABLE OF CONTENTS . . . . .	ix
CHAPTER	
1 INTRODUCTION . . . . .	1
2 NEUTRINOS AND PROPERTIES OF NEUTRINOS . . . . .	7
2.1 Discovery of Neutrino . . . . .	9
2.1.1 Discovery of Different Neutrino Flavours . . . . .	14
2.2 Helicity Of Neutrinos . . . . .	16
2.3 Neutrino Mass, Mixing, Oscillation and Physics Beyond Standard Model . . . . .	20
2.3.1 Probability of Neutrino Oscillation . . . . .	26
2.3.2 Experimental Status . . . . .	33
3 NEUTRINO ELECTRON SCATTERING . . . . .	44
4 THE TEXONO EXPERIMENT OVERVIEW . . . . .	54
4.1 Experimental Set-Up . . . . .	55

4.1.1	The ULB-HPGe Detector . . . . .	64
4.1.2	CsI(Tl) Crystal Scintillating Detector . . . . .	67
5	DATA ANALYZING TECHNIQUES . . . . .	72
5.1	The Performance of CsI(Tl) Detector . . . . .	75
5.2	Calibration Methods . . . . .	82
5.3	Event Selection and Defining Basic Cuts . . . . .	85
5.3.1	Single Hit Cut . . . . .	86
5.3.2	Cosmic Ray Veto Cut . . . . .	87
5.3.3	Pulse Shape Discrimination (PSD) Cut . . . . .	88
5.3.4	Z-position Cut . . . . .	90
5.3.5	The Cut Efficiency and Suppression Factors . . . . .	90
6	BACKGROUND UNDERSTANDING AND SUPPRESSION METHODS . . . . .	97
6.1	Study of the Intrinsic Radiopurity in the CsI(Tl) crystal[83] . . . . .	99
6.2	Understanding Environmental Background . . . . .	109
6.3	Angular Correlation of Gamma Radiation[85] . . . . .	111
6.4	Single Hit (SH) Prediction via Multiple Hit (MH) Analysis . . . . .	117
7	RESULTS AND CONCLUSION . . . . .	132
	REFERENCES . . . . .	147
	VITA . . . . .	154

# CHAPTER 1

## INTRODUCTION

The neutrinos are still the most mysterious particles in the particle physics. Their properties and interactions with matter, as well as experimental conception have not been fully understood yet. This motivation is the locomotive of further experimental studies to discover the neutrino properties and its interaction with matter. After their hypothesized existence from radioactive beta decay process by W. Pauli in 1930 new physics was born. Neutrinos came to picture to explain the missing energy and momentum of nuclear beta decay process but they came with a lot of unanswered questions. Up to now they still keep their secrets. There are very interesting and challenging questions still out there, what is the absolute mass scale or their mass hierarchy, how many mass eigenstate exist and what are the individual mass eigenstates; do neutrinos really change flavour, if yes what is the mixing angles in the mixing matrix; is there any other type of neutrino like sterile neutrino exist; whether they are their own antiparticle or not; do neutrinos violate CP invariance?

Neutrinos were first considered by Pauli as massless particles and also in the Standard Model of weak interaction they are assumed to be massless. However, in Grand Unification Theory neutrinos have to be massive particles. Today it is believed that they should have a small mass. Recent experiments have strong evidence of neutrino oscillations and mixing[1, 2] which are due to neutrino masses. The experiments, Super-Kamiokande, Sudbury Neutrino Observatory, KamLAND and MINOS have shown they have non-zero but small masses. Finding mass of neutrinos would help us to explain of some unsolved physical problems like the dark matter problem in astrophysics[3].

The crucial question is that how can very small neutrinos' masses be measured. There are several precise experimental techniques to find the masses of neutrinos. One of these techniques is based upon the idea that if neutrino oscillation occurs, the neutrinos must be massive. Today's experimental method to measure the very small neutrino mass is based on the detection of what is known as neutrino oscillation. Recently it has been observed that neutrino flavours are mixing but still the mechanism of the mixing is under discussion. The other technique to determine neutrino mass is called direct measurement based on nuclear beta decay. A direct measurement of the neutrino mass can be obtained by measuring the difference between the available energy in a nuclear beta decay (linked by  $E = (\Delta m)c^2$  to the mass difference between the initial and final nuclei) and the highest energy observed in the  $\beta$  rays. The resulting difference is

the energy spend in the neutrino mass, according to the energy-mass equation. Although the masses of neutrinos are not known exactly yet, the experimental limits on the masses can be determined.

Unlike the other leptons neutrinos do not carry charge and the probability of interaction with matter is very low. This makes them very hard to detect. The detection of neutrinos are very difficult since the interaction cross section of neutrinos with matter is very small (i.e.  $100 \text{ fb}$  at  $100 \text{ GeV}$  to  $< 10^{-4} \text{ fb}$  at  $1 \text{ MeV}$ ). In other words, for simplification, the mean free path in water for  $\bar{\nu}_e$  from reactors is  $250 \text{ light} - \text{years}$  at the typical energy range of  $2 \text{ MeV}$ . This disadvantage is covered by huge massive detectors and intense source of neutrinos. In order to detect them you need high flux of neutrino and very big detectors.

The neutrino properties and their interactions with matter is very important for cosmology, astrophysics, nuclear and particle physics[4]. The neutrinos are very important because of their huge amount since early universe. Since the neutrinos interact with matter rarely, there still must be huge number of them, so they can contribute considerable amount of mass to the universe. In this sense, they can play an important role in the evolution of universe. The combined neutrino and cosmology data[5] indicate that our Universe is at critical density and that neutrinos constitute to at least 0.5% of this density, comparable to the fraction shared by visible matter[6]. Neutrinos play a role in our

Table 1.1: The free parameters in Standard Model which have to be determined experimentally.

	<i>name</i>	<i>parameters</i>
<i>constants</i>	the coupling constants	$e, \alpha_s, \sin^2 \theta_W$
<i>mass</i>	bosons	$m_W, m_H$
	leptons	$m_e, m_\mu, m_\tau$
	quark	$m_u, m_d, m_s, m_c, m_b, m_t$
<i>matrix elements</i>	CKM	three angles and a phase $\delta$

existence. Therefore, understanding of neutrino properties is very crucial since we can learn much more about universe as well as structure of matter. Neutrinos have very important role in measuring some important physical quantities of nuclear structures as well. In this sense, neutrinos can be used as a probe of nuclear structure. By studying neutrino-nucleus scattering one can make precise measurement of various electro-weak parameters and structure of the nucleon. For this reason, experimentally and theoretically well understood some mechanisms are studying, in which the energy spectrum and composition of the beam are known well. As a result, the neutrinos link the very small and very big scale physics, from particle physics and nuclear physics to astrophysics and cosmology[3].

There are 18 free parameters which have to be determined experimentally including Weinberg Angle  $\sin^2 \theta_W$ , which is one fundamental parameter of Glashow-Weinberg-Salam (GWS) model. In modelling, massless neutrinos are assumed but neutrino's mass parameters should be added to the list as well[7]. These parameters are listed in Table 1.1.

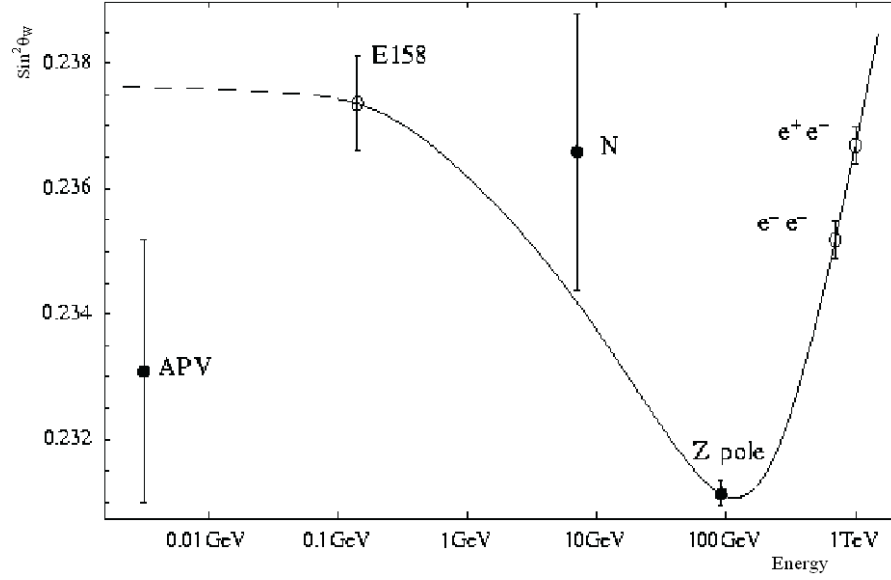


Figure 1.1: The world status of the measurement of Weinberg Angle together with theoretical expectation shown in black curve.

The Weinberg Angle was measured in high energies by using accelerators very precisely. However, there is no significant measurement at low energies with reactor neutrino yet. The world status of the measurements of Weinberg Angle for various (combinations of) observables together with the all data value of 0.23122 is given in Ref. [1] and the measurement status is shown in Figure 1.1. The black curve represents the theoretical expectation calculated by Czarnecki and Marciano in 2000.

In this study, TEXONO Experiment is presented. I will focus on the measurement of neutrino-electron scattering cross section which is fundamental interaction providing information on the Standard Model weak interaction parameters ( $g_V$ ,  $g_A$ , and  $\sin^2 \theta_W$ ). This interaction was observed but there is no significant

measurement at low energy regions yet. With this motivation in the TEXONO Experiment a 200 *kg* of CsI(Tl) scintillating crystal detector was placed to near one of the core of Kuo-Sheng Nuclear Power Plant in Taiwan for studies of electron-antineutrino scattering measurements. The main physics goal is to perform a measurement of the electron-neutrino cross section and subsequently determine the  $\sin^2 \theta_W$  value at low energies with reactor neutrinos[8].

This thesis is divided into the following sections: In the second chapter, an introduction to neutrino physics was given. Properties of neutrino, mixing of neutrino flavours, oscillations and beyond the SM were discussed; In the third chapter, neutrino-electron scattering, particularly in untested lower energy region, in MeV range at Kou-Sheng Nuclear Power Plant was presented. The neutrino sources and expected neutrino spectrum were given; In the fourth chapter, the TEXONO Experiment was presented. Technical design of the detectors, shielding and electronic systems, such as trigger, data acquisition and remote monitoring system were discussed; In the fifth chapter, data analyzing techniques were presented. Properties and performance of our CsI(Tl) scintillating crystal detector, calibration and analysis methods were given; In the sixth chapter, background understanding and suppression methods were discussed. Based on multiple-hit analysis background estimations due to cosmic and  $Tl - 208$  were given; and finally in the chapter seven, the status and results on the measurement of  $\sin^2 \theta_W$  value were presented.



## CHAPTER 2

### NEUTRINOS AND PROPERTIES OF NEUTRINOS

After discovery of electron in 1897 by J. J. Thompson and theory of atom in 1911 by Rutherford, the structure of matter was constructed and elementary particle physics was started. In those times atom was considered as a fundamental block of matter. However, following years by using higher energies the understanding of fundamental matter was changed and in the accelerators a lot of new fundamental particles were found. Today the Standard Model ( $SM$ ) is modeling the mathematical and physical structure of particles. In the SM there are six quarks and six leptons considering as a building blocks of matter shown in Table 2.1. The interaction between them is lead by four fundamental forces, gravitation, electromagnetism, weak and strong forces. In the modelling these interactions are governed by the four force carrier bosons, graviton, gamma,  $Z, W^\pm$  and gluon, respectively given in Table 2.2. The interactions can be classified according to the value of a characteristic dimensionless constant related through a coupling constant to the interaction cross section and interaction time. The

Table 2.1: (a) The elementary particle families in the Standard Model with increasing mass. B, baryon number;  $I$ , isospin and its third component  $I_3$ ; Q, charge;  $B^*$ , bottom; T, top; S, strangeness; C, charm. (b) Properties of Leptons. L flavour-related lepton number.

(a) <b>Flavour</b>	<b>Spin</b>	<b>B</b>	$I$	$I_3$	<b>S</b>	<b>C</b>	<b><math>B^*</math></b>	<b>T</b>	<b>Q[e]</b>
<b>u</b>	1/2	1/3	1/2	1/2	0	0	0	0	2/3
<b>d</b>	1/2	1/3	1/2	-1/2	0	0	0	0	-1/3
<b>s</b>	1/2	1/3	0	0	-1	0	0	0	-1/3
<b>c</b>	1/2	1/3	0	0	0	1	0	0	2/3
<b>b</b>	1/2	1/3	0	0	0	0	-1	0	-1/3
<b>t</b>	1/2	1/3	0	0	0	0	0	1	2/3

(b) <b>Lepton</b>	<b>Q[e]</b>	<b><math>L_e</math></b>	<b><math>L_\mu</math></b>	<b><math>L_\tau</math></b>	<b>L</b>
<b><math>e^-</math></b>	-1	1	0	0	1
<b><math>\nu_e</math></b>	0	1	0	0	1
<b><math>\mu^-</math></b>	-1	0	1	0	1
<b><math>\nu_\mu</math></b>	0	0	1	0	1
<b><math>\tau^-</math></b>	-1	0	0	1	1
<b><math>\nu_\tau</math></b>	0	0	0	1	1

stronger the interaction, the larger is the interaction cross section and shorter is the interaction time. Because of its much smaller strength, the gravitational force can usually be neglected in particle physics. Theoretically, the SM group corresponds to a direct product of three groups,  $SU(3) \otimes SU(2) \otimes U(1)$ , where  $SU(3)$  belongs to the colour group of quantum chromodynamics ( $QCD$ ),  $SU(2)$  to the weak isospin and  $U(1)$  belongs to hypercharge, corresponding quantum numbers shown in Table 2.1. The electro-weak  $SU(2) \otimes U(1)$  section, called the Glashow-Weinberg-Salam (GWS) model[9, 10, 11] or quantum flavour dynamics ( $QFD$ ) consists of the weak isospin  $SU(2)$  and the hypercharge group  $U(1)$ [7].

The neutrinos as an elementary particle have half-integer spin-1/2, therefore the neutrinos are in the fermion family. It has been observed all neutrinos in

Table 2.2: The four fundamental forces in the Standard Model. Natural units  $\hbar = c = 1$  are used.

Interaction Type	Strength	Range	Force Carriers
Gravitation	$G_N \simeq 5.9 \times 10^{-39}$	$\infty$	Graviton
Electromagnetic	$\alpha \simeq 1/137$	$\infty$	$\gamma$
Weak	$G_F \simeq 1.02 \times m_p^{-2}$	$\approx m_w^{-1} \simeq 10^{-3} fm$	$Z, W^\pm$
Strong (nuclear)	$g_\pi^2/4\pi \approx 14$	$m_\pi^{-1} \approx 1.5 fm$	Gluons
Strong (color)	$\alpha_s \simeq 1$	confinement	Gluons

left-handed and all antineutrinos in right-handed chirality. They have small, tiny but non-zero masses. Since the neutrinos are electrically neutral lepton and colorless, the interactions of neutrino neither by way of the strong nor the electromagnetic force, but only through the weak force and gravity[12].

## 2.1 Discovery of Neutrino

After Chadwick discovered a continuous energy spectrum of electrons emitted from  $\beta$ -decay[13], in order to conserve energy and momentum a new particle was postulated theoretically by W. Pauli in 1930. In the study of nuclear beta decay process a nucleus  $A$  is transformed into a slightly lighter nucleus  $B$ , accompanied with the emission of an electron. It seemed to be a two body decay in the first glance. In the two body decay process outgoing energies can be kinematically determined to be constant in the centre of mass frame. Choosing *the parent nucleus*  $A$  is at rest, then *the daughter nucleus*  $B$  and  $e^-$  come out back to back with equal and opposite momenta. From conservation of energy, the electron energy  $E_e$  is then

$$E_e = \left( \frac{m_A^2 - m_B^2 + m_e^2}{2m_A} \right) c^2 \quad (2.1)$$

One can notice that  $E_e$  is fixed since the three masses are well defined. However, experiments show that there is no fixed energy of the emitted electron. The energy of the electron varies and reaches a maximum value as obtained from the formula (2.1). Also physicists do not observe back to back events. It seems violation of energy and momentum conservation. At this point Pauli suggested the existence of a new spin-1/2 neutral particle which carries the missing energy and momentum to save the energy and momentum conservation. Then three body decay with the mysterious third particle would explain why physicists do not observe the fixed energy of the electron and the lack of back to back emission. It was concluded that it had to be electrically neutral to explain why it left no track. Thus charge is also conserved. Pauli named this new particle as a *neutron*. In 1932 Chadwick use this name for neutral nucleons in the structure of the nucleus. Later it was called *neutrino*[14] (which means little and neutral) by Fermi who presented a theory of beta decay. In modern terminology, the fundamental beta decay process is that neutron decays into a proton, electron and a anti electron type neutrino[15].

$$n \rightarrow p^+ + e^- + \bar{\nu}_e \quad (2.2)$$

And inverse beta decay process for the proton is

$$p^+ + \bar{\nu}_e \rightarrow n + e^+ \quad (2.3)$$

where  $\nu_e$  refers to electron type neutrino and  $\bar{\nu}_e$  refers to its antiparticle.

20 years later in 1953 first experimental evidence for neutrinos was found in nuclear recoil experiment and finally in 1958 discovery took place at nuclear reactor experiment via  $\bar{\nu}_e - p$  scattering. Reines and Cowan[16] first detected the neutrino by designing a classical detector with liquid scintillator tanks and water target doped with Cadmium. What happens in the detector is that neutrino interact with a nucleus through the weak force and a proton turns into a neutron via Equation (2.4).

$$\bar{\nu} + N (n, p) \rightarrow e^+ + N (n + 1, p - 1) \quad (2.4)$$

where n equals the number of neutrons and p equals the number of protons.

Reines and Cowan planned to build a counter filled with liquid scintillator and surrounded with photomultiplier tubes (PMTs), the “eyes” that would detect the positron from inverse beta decay, which is the signal of a neutrino-induced event. The Figure 2.1 illustrates how the liquid scintillator converts a fraction of the energy of the positron into a tiny flash of light. The light is shown traveling through the highly transparent liquid scintillator to the PMTs, where the photons are converted into an electronic pulse that signals the presence of the positron. Inverse beta decay (1) begins then an antineutrino (red dashed line)

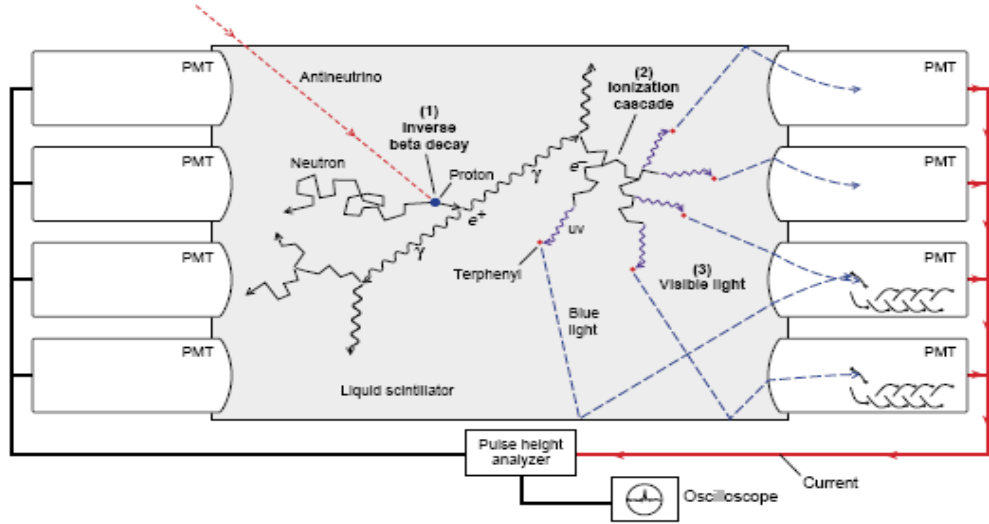


Figure 2.1: Reines and Cowan Experiment on Liquid Scintillation Counter for Detecting the Positron from Inverse Beta Decay.

interacts with one of the billions and millions of protons (hydrogen nuclei) in the molecules of the liquid. The weak charge-changing interaction between the antineutrino and the proton causes the proton to turn into a neutron and the antineutrino to turn into a positron. The neutron wanders about undetected. The positron, however, soon collides with an electron, and the particle-antiparticle pair annihilates into two gamma rays ( $\gamma$ ) that travel in opposite directions. The experiment based on the measurement of 511 keV annihilation photons and a neutron capture reaction after  $10 \mu\text{sec}$ . The scintillators detect the coincidence of 511 keV annihilation photons and  $\gamma$ -rays emitted by the neutron capture on Cd-113. Each gamma ray loses about half its energy each time it scatters

from an electron (Compton scattering). The resulting energetic electrons scatter from other electrons and radiate photons to create an ionization cascade (2) that quickly produces large numbers of ultraviolet ( $uv$ ) photons. The scintillator is a highly transparent liquid (toluene) purposely doped with terphenyl. When it becomes excited by absorbing the  $uv$  photons, it scintillates by emitting visible photons as it returns to the ground (lowest-energy) state (3). Because the liquid scintillator is transparent to visible light, about 20 percent of the visible photons are collected by the PMTs lining the walls of the scintillation counter. The rest are absorbed during the many reflections from the counter walls. A visible photon releases an electron from the cathode of a phototube. That electron then initiates the release of further electrons from each dynode of the PMT, a process resulting in a measurable electrical pulse. The pulses from all the tubes are combined, counted, processed, and displayed on an oscilloscope screen[17]. At their detector the antineutrino flux was calculated to be  $5 \times 10^{13}$  particles per square centimeter per second. Despite the huge intensity, only two or three events occurred every hour[7]. The experiment results on observation cross-section agrees well with the theoretically predicted cross section for inverse beta decay on protons which is  $6.3 \times 10^{-44}$ . On June 14, 1956, after all the tests had been completed, Reines and Cowan sent a telegram to Pauli at Zurich University: “We are happy to inform you that we have definitely detected neutrinos from fission fragments by observing inverse beta decay of protons. Observed

cross section agrees well with expected six times ten to minus forty-four square centimeters.” [17]

### 2.1.1 Discovery of Different Neutrino Flavours

In  $\beta$  decay of an atomic nucleus, or in a nuclear reaction within a star, the emitted electron is associated with a neutrino which is an electron neutrino. A similar decay process, the pion decay, discovered by Powell and his group [18], is another source of neutrino production. In 1959 Pontecorvo ask question whether the neutrino emitted in  $\beta$ -decay is the same as the one emitted in pion decay [19]. In case of  $\nu_\mu$  and  $\nu_e$  are identical particles, then one must observe these reaction (2.5) with the same rate.

$$\begin{aligned} \nu_\mu + n &\rightarrow \mu^- + p & \text{and} & & \nu_\mu + n &\rightarrow e^- + p \\ \bar{\nu}_\mu + p &\rightarrow \mu^+ + n & \text{and} & & \bar{\nu}_\mu + p &\rightarrow e^+ + n \end{aligned} \quad (2.5)$$

In pion decay at rest the muon could emerge at any angle to the coming pion direction. The earliest picture of Powell showing the track of a pion in a photographic emulsion exposed to cosmic rays at high altitude, the pion decays into a muon and a neutrino which leaves no track since it is electrically neutral. The process is;

$$\pi^- \rightarrow \mu^- + \nu_\mu \quad (2.6)$$

The muon energy in the pion decay process is found to be constant within experimental uncertainties. This means that the pion decay is a two body decay.



Afterwards, the muon coming from decay of pion decays to an electron. The decay process is;

$$\mu^- \rightarrow e^- + \nu_\mu + \bar{\nu}_e \quad (2.7)$$

When this process was observed repeatedly it was found that the energy of emitted electron varied. It was concluded that the muon decay must be three body decay which means two neutrinos were emitted. One is muon type neutrino ( $\nu_\mu$ ) and the other is electron type antineutrino ( $\bar{\nu}_e$ ).

The experiment was done at the Brookhaven AGS using a 15 *GeV* proton beam hitting a Beryllium target[20]. As a result totally 29 muon-like events and 6 electron like events were observed showing that  $\nu_\mu \neq \nu_e$ . In pion decay the emitted muon is accompanied, as in beta decay, by a neutrino. However, the emitted neutrino is not the same as the one which accompanied  $e^-$  in the  $\beta$  decay. In 1962 Danby et al.[20] showed that they produced  $\mu^+$  via  $\bar{\nu}_\mu + p \rightarrow \mu^+ + n$  but not  $e^+$  via  $\bar{\nu}_\mu + p \rightarrow e^+ + n$ . The latter process is never observed. Also  $\mu^-$  decay into  $e^-$  via the process  $\mu^- \rightarrow e^- + \gamma$  is not observed. Similarly, considering the pair production process  $\gamma + A \rightarrow e^+ + e^- + A'$  and  $\gamma + A \rightarrow \mu^+ + \mu^- + A'$ , these are observed separately but never the mixed one  $\gamma + A \rightarrow \mu^+ + e^- + A'$ . Thus we can distinguish the electron and its partner neutrino from the muon and its partner neutrino; in other words  $\nu_\mu$  is different from  $\nu_e$ . Therefore, we must attach *electron like* and *muon like* labels to the corresponding neutrinos.

After the discovery of the  $\tau$  lepton, the analysis of weak interaction has

shown the existence of the three different kinds or flavours of neutrinos and lepton family grown to 12, the electron, the muon, the tau, their respective neutrinos, and the corresponding antiparticles. Alternatively, different neutrinos are associated with the charged lepton similar to the electron, but with a bigger mass, the muon and the tau[15].

## 2.2 Helicity Of Neutrinos

Up to 1950's physicist believe that the parity is conserved in all reaction. Parity can be defined as a mirror transformation by replacing  $\vec{x} \rightarrow -\vec{x}$ . Parity conservation implies that the physical process and its mirror one have same probability. Parity violation means that the physical process are different for both cases. In 1956 Lee and Yang shows that parity is not conserved in weak interaction[21]. The pseudoscalar which are product of a polar and an axial vector do the same thing meaning that they change sign under parity transformation. The helicity  $H$  can be defined as product of spin and momentum, meaning that helicity is the component of the spin in the direction of the motion, Equation (2.8). In the other words, the value of  $m_s$  for the axis along momentum direction is called the helicity of the particle[22].

$$H = \frac{\vec{S} \cdot \vec{P}}{|\vec{S}| \times |\vec{P}|} \quad (2.8)$$

Spin 1/2 particles can have helicity  $\lambda = \pm 1$ , corresponding to spin projection parallel or antiparallel to the direction of motion. By analogy with polarized

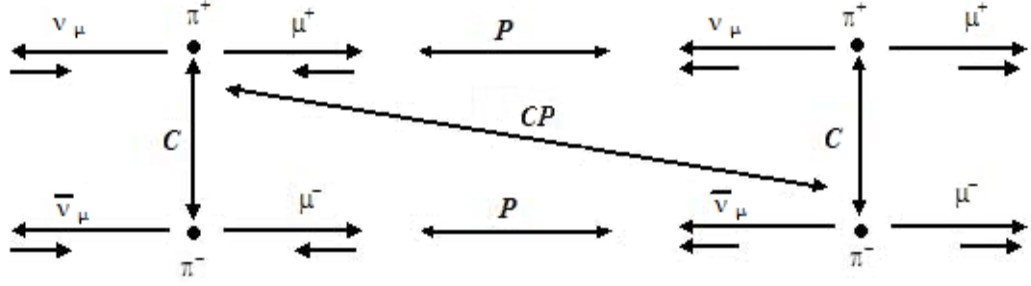


Figure 2.2: Schematic view of pion decay at rest. The spin and momentum is shown after applying parity transformation (P), charge conjugation (C) and CP operation.

light, the positive helicity state is often termed *right handed* and the negative helicity state *left handed*. Thus the fermion whose spin is  $1/2$  can have a helicity of  $+1$  ( $J_3 = 1/2$ ) or  $-1$  ( $J_3 = -1/2$ ). As an example we can consider positive pion decay at rest[23] via Equation (2.9).

$$\pi^+ \rightarrow \mu^+ + \nu_\mu \quad (2.9)$$

Since pion decay at rest from conservation of momentum outgoing particles move back to back in space. Furthermore, since pion carries spin-0, the spins of the muon and neutrino also must be opposed to each other. The schematic drawing of pion decay at rest is illustrated in Figure 2.2 under Charge Conjugate(C), Parity Transformation (P) and CP operations.

The helicities  $H(\mu^+) = H(\nu_\mu) = -1$  turn into  $+1$  after applying parity transformation. Parity invariance would imply that both helicities should have the

same probability and no longitudinal polarization of the muon should be observed. Parity violation would already be established if there were some polarization. By measuring only  $H(\mu^+) = +1$  it turned out that parity is maximally violated. these observations finally led to the V-A theory of weak interaction[7].

The neutrinos as a spin-1/2 particles can be described by four-spinors  $\psi(x)$  which obey the Dirac Equation, corresponding to particle anti-particles with two spins  $J_3 = \pm 1/2$  in quantum field theory. The Dirac Equation is nothing but the relativistic wave equation for spin-1/2 particles and given by Equation (2.10). However, experimental observations show that only left-handed neutrinos ( $H = -1$ ) and right-handed anti-neutrinos ( $H = +1$ ) exist. Therefore, we can say that two-component spinor can describe the neutrinos in principle[24, 25].

$$\left(i\gamma^\mu \frac{\partial}{\partial x^\mu} - m\right)\psi = 0 \quad (2.10)$$

here  $\psi$  denotes a four-component spinor and the  $4 \times 4$   $\gamma$ -matrices are given in the form of Equation (2.11)

$$\gamma_0 = \begin{pmatrix} 1 & 0 \\ 0 & -1 \end{pmatrix} \text{ and } \gamma_i = \begin{pmatrix} 0 & \sigma_i \\ -\sigma_i & 0 \end{pmatrix} \quad (2.11)$$

where  $\sigma_i$  correspond to the  $2 \times 2$  Pauli matrices.

The wave function  $\psi$  can be rewritten in terms of left- and right-handed components as in Equation (2.12);

$$\psi = (P_L + P_R)\psi = P_L\psi + P_R\psi = \psi_L + \psi_R \quad (2.12)$$

here the projection operators  $P_L$  and  $P_R$  can be express as in Equation (2.13)

$$P_L = \frac{1}{2}(1 - \gamma_5) \text{ and } P_R = \frac{1}{2}(1 + \gamma_5) \quad (2.13)$$

The matrix  $\gamma_5$  is given by Equation (2.14)

$$\gamma_5 = i\gamma_0\gamma_1\gamma_2\gamma_3 = \begin{pmatrix} 0 & 1 \\ 1 & 0 \end{pmatrix} \quad (2.14)$$

The Equation (2.10) can be expressed in these projection of wavefunction in Equation (2.12) as Equation (2.15)

$$\begin{aligned} \left( i\frac{\partial}{\partial x^0} - i\sigma_i\frac{\partial}{\partial x_i} \right) \psi_R &= m\gamma_0\psi_L \\ \left( i\frac{\partial}{\partial x^0} + i\sigma_i\frac{\partial}{\partial x_i} \right) \psi_L &= m\gamma_0\psi_R \end{aligned} \quad (2.15)$$

Both equations in Equation (2.15) decouple in case of vanishing mass,  $m = 0$  and turn into Weyl Equation. For non-vanishing mass case decoupling of Equation (2.15) is no longer possible. This means that the eigenspinors  $\psi_L$  and  $\psi_R$  no longer describe particles with fixed helicity and helicity is no longer a good conserved quantum number[7].

Particles are distinguished from their own antiparticles by comparing some physical properties like charge and helicity. For neutrinos the situation is not so clear. Neutrinos do not carry electric charge. Neutrinos can be differed from antineutrinos only by the help of helicity. If particle and its antiparticle are different, they are called Dirac-particle. If particle and its antiparticle are the same, they are called Majorana particles. In the Dirac case  $\nu_L$  is converting into

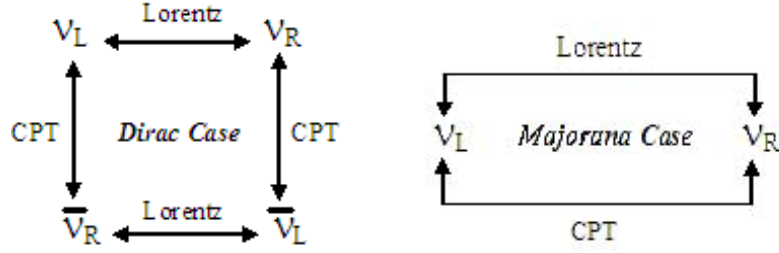


Figure 2.3: Schematic view of the massive Dirac and Majorana neutrinos.

$\bar{\nu}_R$  via CPT transformation. On the other hand, in Majorana case under both CPT and Lorentz transformation  $\nu_L$  turn into  $\nu_R$  since neutrino is its antiparticle as shown in Figure 2.3. Furthermore, if neutrinos are Majorana type, the lepton number conservation is violated since initial and final state lepton number are not the same in nuclear beta decay anymore.

### 2.3 Neutrino Mass, Mixing, Oscillation and Physics Beyond Standard Model

In the Standard Model[26, 27, 28] all elementary particles can be grouped into two families, *the quarks* and *the leptons*. Each family has six members. If we group the two families into pairs regarding the masses and charges we have three pairs of family. These families are listed in Table 2.3 based on the recent experiments and data from reference [1].

All stable matters in the known universe are made up of  $e^-$  and one pair of quarks, up and down. However, they are not enough to build whole universe. The other elementary particles which form unstable matter occur in the high

Table 2.3: The elementary particle families in the Standard Model.

<i>Particle</i>	<i>Mass (MeV)</i>	<i>Particle</i>	<i>Mass (MeV)</i>
<i>u</i>	1.5 to 3.0	<i>s</i>	$95 \pm 25$
<i>d</i>	3 to 7	<i>c</i>	$1250 \pm 90$
<i>e</i>	$0.510998918 \pm 0.000000044$	$\mu$	$105.6583692 \pm 0.0000094$
$\nu_e$	$< 2.25 \times 10^{-6}$	$\nu_\mu$	$< 0.17$

<i>Particle</i>	<i>Mass (GeV)</i>
<i>b</i>	$4.20 - 4.7 \pm 0.07$
<i>t</i>	$174.2 \pm 3.3$
$\tau$	$1.77699^{+0.00029}_{-0.00026}$
$\nu_\tau$	$< 0.0182$

energy process naturally in the universe or artificially in laboratories.

The various matter and force-carrying particles have a range of masses. This is another puzzle in physics. The *photon*, carrier of the electromagnetic force, and the *gluons* carrying the strong force are massless. On the other hand, the mediators of the weak force, the  $W^\pm$  and  $Z$  particles are very massive particles whose weigh  $80.4 \text{ GeV}$  and  $91.187 \text{ GeV}$  respectively, as much as a reasonably sized nucleus. Furthermore,  $W^\pm$  have charge also unlike the other mediators. Indeed, how particles get masses and its mechanism at all are not totally understood.

Although Standard Model explains most phenomenon in particle physics and match with experiment with high accuracy, also successfully unify the two fundamental forces of electromagnetism and weak interaction, still it is believed that Standard Model is not a complete theory. Discovery of the neutrino mass shows us a new physics beyond the Standard Model and it plays a very important role in the development of modern particle physics. Non-vanishing neutrino mass

require mixing and oscillation (neutrino flavour changes)[1, 2] considering weak eigenstates  $\nu_\alpha$  not identical to the mass eigenstates  $\nu_i$ , as in the quark sector which are connected by a unitary matrix called Cabibbo-Kobayashi-Maskawa (CKM), the  $\nu_\alpha$  is connected  $\nu_i$  by Pontecorvo-Maki-Nakagawa-Sakata (PMNS) matrix[7]. Thus when such a particle is propagated, it behaves like a wave with time-dependence related to the mass of the particle considered. This principle is the basis of the neutrino oscillation[29]. Neutrinos are always created or detected with a well defined flavor (electron, muon, tau). However, in a phenomenon known as neutrino flavor oscillation, neutrinos are able to oscillate between the three available flavors while they propagate through space. Specifically, this occurs because the neutrino flavor eigenstates are not the same as the neutrino mass eigenstates (simply called 1, 2, 3). This allows for a neutrino that was produced as an electron neutrino at a given location to have a calculable probability to be detected as either a muon or tau neutrino after it has traveled to another location. This effect was first noticed due to the number of electron neutrinos detected from the Sun's core failing to match the expected numbers, a discrepancy dubbed the "solar neutrino problem". The existence of flavor oscillations implies a non-zero neutrino mass, because the amount of mixing between neutrino flavors at a given time depends on the differences in their squared-masses (mixing would be zero for massless neutrinos). Despite their massive nature, it is still possible that the neutrino and antineutrino are in



fact the same particle, a hypothesis first proposed by the Italian physicist Ettore Majorana[30]. The most rigid limits on Majorana neutrino mass come from the Heidelberg-Moscow experiments. Neutrinoless double beta decay which violates lepton number conservation was searched in  $^{76}\text{Ge}$  decay and they claim for evidence of that. However, their correctness is still under discussion since their observed signal may probably be an unknown background peak.

There are several ways to show the existence of neutrino oscillation. One is the measurement of the solar neutrino flux[31, 32]. The natural phenomena is that some of the neutrinos produced in the Sun as an electron type, transform into a different type of neutrinos. One can measure how many of them are transformed and disappear on the way between the Sun and Earth; this is clearly evidence of the neutrino oscillation. Another method is the search for oscillation using reactions of neutrinos produced by transformation from the original type in neutrino beams from particle accelerators.

In the experiments on solar neutrinos, the observed flux is significantly lower than that of expected one according to the solar model based on the astrophysics knowledge[33]. Part of the  $\nu_e$  transform into neutrinos of a different type on their way from the Sun to the Earth. Such experiments searching for neutrino oscillation which are based on disappearance of the neutrinos are called *disappearance experiments*. On the other hand, *appearance experiments* make a measurement of neutrinos of a different type than the original ones. Therefore,

in the case of solar neutrinos, instead of the measuring the reduced flux of  $\nu_e$ , appearance of unexpected  $\nu_\mu$  is investigated. Unfortunately, appearance experiments are practically impossible for solar neutrinos. To be detectable the  $\nu_\mu$  should interact with the detector and produce its corresponding charged partner, the  $\mu$ . However, this is impossible kinematically, since from the energy mass equation the muon rest mass energy is higher than the energy of the neutrinos emitted in nuclear reaction within the Sun. The only way of making appearance experiment is by particle accelerators which supply sufficient energy to produce the particles associated with the other neutrino type. The fundamental weak interaction not only can generate neutrinos as in the case in nuclear reactions within the Sun, but it can also make them observable when they interact in an experimental apparatus, producing various electrically charged particles that can be detected.

Considering the neutrinos as bunches of waves rather than as particles with well-defined momentum according to the quantum mechanics laws, neutrino eigenstates in propagation are represented by waves, and their phases are related to their energy. Thus, if neutrinos have different masses, their corresponding phases must be also different.

As an example, consider neutrinos which come from the Sun that are the electron type neutrinos. Following them on their way towards the Earth we can observe their mass eigenstates since the waves propagate with a distinct phase

according to the neutrino mass. If the masses of the eigenstates are the same, the corresponding waves comes to the Earth with the same phase. If not, the corresponding waves are propagated with a different phase. For simplicity, first consider two neutrino types,  $\nu_e$  and  $\nu_\mu$ . The most probable mixing for  $\nu_e$  is with  $\nu_\mu$  since in the elementary particle classification masses of the electrically charge particles associated with the neutrinos, which are  $e^-$  and  $\mu^-$  respectively, are the closest to each other. Thus, the waves of the neutrinos produced by the Sun could not reach the Earth as a pure flavour state  $\nu_e$ , but rather due to  $\nu_e \rightarrow \nu_\mu$  mixing with a  $\nu_\mu$  component developed on the way. As a quantum mechanics postulates, the waves become  $\nu_e$  at times and  $\nu_\mu$  at other times depending on the size of the mixing. Mixing is in the quantum mechanical sense, depending on the parameters of mixing, one of them will be seen at times and at other times the other. However, mixing of neutrinos is considered not in terms of flavour eigenstates such as  $\nu_e$  and  $\nu_\mu$  but in terms of mass eigenstates which are the so-called  $\nu_1$  and  $\nu_2$ .

To understand the mixing process, we consider a system of Cartesian coordinates of which the base vectors  $x$  and  $y$  are the flavour eigenstates and another system of Cartesian coordinates of which the base vector  $x'$  and  $y'$  are the mass eigenstate rotated by a small angle with respect to the system  $x - y$ . Consider a point for the pure flavour eigenstate which is on  $x$  axis,  $P(x, 0)$ . This has a large component along the  $x'$  and a small component along the  $y'$ . In other

words, the point which is in the  $x$  axis only is represented by a combination or a mixing of two components  $x'$  and  $y'$ . The parameter of the mixing is only the rotational angle of one Cartesian system with respect to the other which is called the *mixing angle*. If the mixing angle is small, the eigenstates almost overlap each other. This means that if the value of the mixing angle is considered to be very small (not yet proved so), the mass eigenstates can be considered as almost pure flavour eigenstate[34].

### 2.3.1 Probability of Neutrino Oscillation

Neutrino oscillation implies that neutrinos must have mass. In order to measure neutrino's masses and consequently to observe oscillation, one can measure neutrino interaction with matter. Neutrinos are quite difficult to observe because of the very low probability of their interactions with matter. Since the cross section in weak nuclear interactions is very small, neutrinos can pass through matter almost unhindered. For typical neutrinos produced in the Sun (with energies of a few MeV), it would take approximately one light year ( $\sim 10^{16}m$ ) of lead to block half of them[12]. Detection of neutrinos is therefore challenging, requiring large detection volumes or high intensity artificial neutrino beams[30].

Consider the charged current weak interaction of neutrinos as in the expression (2.16). In this type interaction the neutrino creates an associated charged lepton of the same flavour. Oscillations of flavour occurs in time since the mass

eigenstates have different phases. We can write an equation like Equation (2.17) that flavour eigenstate can be considered as a superposition of a mass eigenstate if there is no degenerate states that is  $m_1 \neq m_2 \neq m_3$ .

$$\nu_\ell + A \rightarrow \ell + B \quad (2.16)$$

$$|\nu_\ell\rangle = \sum_m U_{\ell m} |\nu_m\rangle \quad (2.17)$$

where the mixing matrix  $U$  is unitary. In two dimension the mixing matrix can be written as in the expression (2.18) with mixing angle  $\theta_{\ell\ell'}$ .

$$U_{\ell m} = \begin{pmatrix} \cos \theta_{\ell\ell'} & \sin \theta_{\ell\ell'} \\ -\sin \theta_{\ell\ell'} & \cos \theta_{\ell\ell'} \end{pmatrix} \quad (2.18)$$

In general formalism,

$$|\nu_\ell\rangle = \sum_m U_{\ell m} |\nu_m\rangle \iff |\nu_m\rangle = \sum_l (U)_{m\ell}^\dagger |\nu_l\rangle = \sum_l (U)_{m\ell}^* |\nu_l\rangle \quad (2.19)$$

In the case of antineutrinos flavour eigenstate can be express like in Equation (2.17)

$$|\bar{\nu}_\ell\rangle = \sum_m U_{\ell m}^* |\bar{\nu}_m\rangle \quad (2.20)$$

For the case of two neutrino mixing, the flavour eigenstate can be expressed as a superposition of the mass eigenstates,  $\nu_1$  and  $\nu_2$ .

$$\begin{pmatrix} |\nu_\ell\rangle \\ |\nu_{\ell'}\rangle \end{pmatrix} = \begin{pmatrix} \cos \theta_{\ell\ell'} & \sin \theta_{\ell\ell'} \\ -\sin \theta_{\ell\ell'} & \cos \theta_{\ell\ell'} \end{pmatrix} \begin{pmatrix} |\nu_1\rangle \\ |\nu_2\rangle \end{pmatrix} \quad (2.21)$$

While there are only three known weak eigenstates, there may be more than three mass eigenstates. For example, if there are four mass eigenstates then one linear combination of them does not have a weak eigenstate partner meaning that  $\nu_s$  is not couple to the  $W^\pm$  or  $Z$  bosons. Such a neutrino which does not have any weak couplings is called "sterile neutrinos".

To understand the neutrino oscillation in vacuum, let us consider how a neutrino born as the  $\nu_\ell$  of Equation (2.17) evolves in time[35]. Since mass eigenstates have definite phases, we can write

$$|\nu_m(x, t)\rangle = e^{-iE_m t} |\nu_m(x, 0)\rangle = e^{-iE_m t} e^{i\vec{p} \cdot \vec{x}} |\nu_m\rangle \quad (2.22)$$

after travel a distance  $L$  the neutrino evolves as

$$|\nu_m(t)\rangle = e^{-i(E_m t - P_m L)} |\nu_m\rangle \quad (2.23)$$

here  $E_m$  and  $P_m$  are the energy and momentum of  $\nu_m$  in the laboratory frame, respectively. Because the neutrino is highly relativistic so we can consider  $E_m = \sqrt{p_m^2 + M_m^2} \approx p + M_m^2/2p$  since  $M_m \ll p$  and  $t \approx L$ . Here we consider  $\nu_\ell$  has been produced with a definite momentum  $p$ , so that all of its mass-eigenstate components have this common momentum. Also highly relativistic neutrinos implies that  $E \approx p$ . After substituting these approximations into Equation (2.23) one can obtain;

$$|\nu_m(L)\rangle = e^{-i(M_m^2/2E)L} |\nu_m\rangle \quad (2.24)$$

after a neutrino born as a  $\nu_\ell$ , has propagated a distance  $L$ , its state vector becomes;

$$|\nu_\ell(L)\rangle = \sum_m U_{\ell m} e^{-i(M_m^2/2E)L} |\nu_m\rangle \quad (2.25)$$

By inverting Equation (2.17), using the unitary matrix of  $U^\dagger$  and inserting into Equation (2.25), the equation becomes

$$|\nu_\ell(L)\rangle = \sum_{\ell'} \left( \sum_m U_{\ell m} e^{-i(M_m^2/2E)L} U_{\ell' m}^\dagger \right) |\nu_{\ell'}\rangle \quad (2.26)$$

We see from Equation (2.26) that  $\nu_\ell$  after travelling the distance  $L$ , has turned into a superposition of all other flavours of  $\nu_{\ell'}$ . Then we can calculate the probability of the neutrino oscillation, turning flavour from  $\ell$  to  $\ell'$ ;  $P(\nu_\ell \rightarrow \nu_{\ell' \neq \ell}, L)$  is given by

$$\begin{aligned} P(\nu_\ell \rightarrow \nu_{\ell' \neq \ell}, L) &= |\langle \nu_{\ell'} | \nu_\ell(L) \rangle|^2 \\ &= \left| \sum_m U_{\ell m} e^{-i(M_m^2/2E)L} U_{\ell' m}^\dagger \right|^2 \end{aligned} \quad (2.27)$$

Using the matrix in Equation (2.21) for the calculation for the probability of oscillation one can obtain that

$$\begin{aligned} P(\nu_\ell \rightarrow \nu_{\ell' \neq \ell}, L) &= \frac{1}{2} \sin^2 2\theta_{\ell\ell'} \left[ 1 - \cos \left( \frac{M_2^2 - M_1^2}{2E} L \right) \right] \\ &= \sin^2 2\theta_{\ell\ell'} \sin^2 \left( \frac{\Delta M_{1,2}^2 (eV/c^2)^2 L(km)}{4E (GeV)} \right) \end{aligned} \quad (2.28)$$

where  $\Delta M_{1,2}^2 = M_2^2 - M_1^2$ . When we put previously omitted factors of  $\hbar$  and  $c$ , then

$$\frac{\Delta M_{1,2}^2}{4} \left( \frac{L}{E} \right) \cong 1.27 \Delta M_{1,2}^2 \left( \frac{L}{E} \right) \quad (2.29)$$

It can be found from expression (2.28) that to obtain a large probability of oscillation we must satisfy the condition:

$$\left(\frac{L}{E}\right)^{-1} = \left(\frac{2}{\pi}\right) 1.27 \Delta M_{1,2}^2 \quad (2.30)$$

We can see that only if  $\Delta M^2$  and  $\theta$  are not vanishing in Equation (2.28), the oscillation occurs.

When neutrinos travel through matter instead of vacuum the probability of oscillation is different due to  $\nu$  scattering from or interaction with particles. This effect is known as Mikheyev-Smirnov-Wolfenstein (MSW) effect[7].

In the case of three dimension, there are only three neutrino mass eigenstates and corresponding three neutrino flavour, the mixing can be written as;

$$\begin{pmatrix} \nu_e \\ \nu_\mu \\ \nu_\tau \end{pmatrix} = \begin{pmatrix} U_{11} & U_{12} & U_{13} \\ U_{21} & U_{22} & U_{23} \\ U_{31} & U_{32} & U_{33} \end{pmatrix} \begin{pmatrix} \nu_1 \\ \nu_2 \\ \nu_3 \end{pmatrix} \quad (2.31)$$

and the unitary mixing matrix, called Pontecorvo-Maki-Nagakawa-Sakata lepton mixing matrix, in three dimension is

$$U_{PMNS} = \begin{matrix} & \nu_1 & \nu_2 & \nu_3 \\ \begin{matrix} \nu_e \\ \nu_\mu \\ \nu_\tau \end{matrix} & \begin{pmatrix} c_{12}c_{13} & s_{12}c_{13} & s_{13} \\ -s_{12}c_{23} - c_{12}s_{23}s_{13}e^{i\delta} & c_{12}c_{23} - s_{12}s_{23}s_{13}e^{i\delta} & s_{23}c_{13}e^{i\delta} \\ s_{12}s_{23} - c_{12}c_{23}s_{13}e^{i\delta} & -c_{12}s_{23} - s_{12}c_{23}s_{13}e^{i\delta} & c_{23}c_{13}e^{i\delta} \end{pmatrix} \end{matrix} \\ \times \text{diag} \begin{pmatrix} e^{i\alpha_1/2} & e^{i\alpha_2/2} & 1 \end{pmatrix} \end{matrix} \quad (2.32)$$



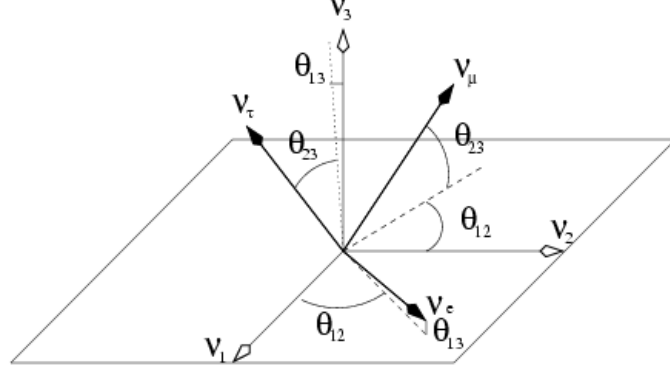


Figure 2.4: Graphical representation of mixing matrix elements between flavor and mass eigenstates.

where three angles  $\theta_{ij}$  are mixing angles,  $c_{ij} = \cos \theta_{ij}$  and  $s_{ij} = \sin \theta_{ij}$ , ( $i = 1, 3$ ) and the quantities  $\delta$  is a Dirac  $CP$  violating phase,  $\alpha_1, \alpha_2$  are possible Majorana  $CP$  violating phases. The last term in the unitary matrix is for Majorana neutrinos to distinguish whether neutrinos and anti-neutrinos are different or the same. As in Equation (2.33) these phases do not effect neutrino oscillation. A graphical illustration of the mixing matrix elements ignoring the  $CP$ -phase is shown in Figure 2.4.

The transition probability in the case of three dimension can be written as

$$\begin{aligned}
P(\nu_\alpha \rightarrow \nu_\beta)(t) &= \sum_i^3 \sum_j^3 U_{\alpha i}^* U_{\beta i} U_{\alpha j} U_{\beta j}^* e^{-i(E_i - E_j)t} \\
&= \delta_{\alpha\beta} - 4 \sum_{i>j=1}^3 \text{Re}(U_{\alpha i}^* U_{\beta i} U_{\alpha j} U_{\beta j}^*) \sin^2 \left( \frac{\Delta m_{ij}^2 L}{4 E} \right) \\
&\quad + 2 \sum_{i>j=1}^3 \text{Im}(U_{\alpha i}^* U_{\beta i} U_{\alpha j} U_{\beta j}^*) \sin \left( \frac{\Delta m_{ij}^2 L}{2 E} \right) \quad (2.33)
\end{aligned}$$

with  $\Delta m_{ij} = m_i^2 - m_j^2$  is in  $eV^2$ ,  $L$  is in  $km$ , and  $E$  is in  $GeV$ .

Assuming that  $CPT$  holds,

$$P(\bar{\nu}_\alpha \rightarrow \bar{\nu}_\beta) = P(\nu_\beta \rightarrow \nu_\alpha) \quad (2.34)$$

However, from Equation (2.33) we see that

$$P(\nu_\beta \rightarrow \nu_\alpha; U) = P(\nu_\alpha \rightarrow \nu_\beta; U^*) \quad (2.35)$$

Then  $CPT$  holds,

$$P(\bar{\nu}_\alpha \rightarrow \bar{\nu}_\beta; U) = P(\nu_\alpha \rightarrow \nu_\beta; U^*) \quad (2.36)$$

That is, the probability for oscillation of an antineutrino is the same as that for a neutrino, except that the mixing matrix  $U$  is replaced by its complex conjugate. Thus, If  $U$  is not real, the neutrino and antineutrino oscillation probabilities can differ by having opposite values of the last term in Equation (2.33). When  $CPT$  holds, any difference between these probabilities indicates a violation of  $CP$  invariance[35].

Using  $CP$  invariance ( $U$  is real), Equation (2.33) simplified and the probability of oscillation in three dimensions can be rewritten as;

$$\begin{aligned} P(\nu_\alpha \rightarrow \nu_\beta)(t) &= \sum_i^3 U_{\alpha i}^2 U_{\beta i}^2 + 2 \sum_{i>j=1}^3 U_{\alpha i} U_{\beta i} U_{\alpha j} U_{\beta j} \cos\left(\frac{\Delta m_{ij}^2 L}{2E}\right) \\ &= \delta_{\alpha\beta} - 4 \sum_{i>j=1}^3 U_{\alpha i} U_{\beta i} U_{\alpha j} U_{\beta j} \sin^2\left(\frac{\Delta m_{ij}^2 L}{4E}\right) \end{aligned} \quad (2.37)$$

where  $\alpha, \beta = e, \mu, \tau$ .

### 2.3.2 Experimental Status

There are two different approaches for neutrino oscillation experiment, appearance and disappearance method. In appearance method the experiment focus on observation of new neutrino flavour, on the other hand in disappearance method the experiment focus on observation less than the expected or theoretical number of neutrinos. For neutrino oscillation several neutrino sources can be used for different purposes. The most important ones are the Sun for  $\nu_e$ , the nuclear power plants for  $\bar{\nu}_e$ , accelerators and the atmosphere for  $\nu_e$ ,  $\nu_\mu$ ,  $\bar{\nu}_e$ ,  $\bar{\nu}_\mu$ .

Determination of flavours relies on the detection of charged lepton produced via charged current interactions of

$$\nu_\ell + N \rightarrow \ell^- + X \quad (2.38)$$

where  $\ell = e, \mu, \tau$ .

In Figure 2.5 the oscillation probability  $P(\nu_\alpha \rightarrow \nu_\beta)$  is illustrated as a function of  $L/E$  for  $\sin^2 2\theta = 0.83$ . That means  $L/E \gtrsim 4/\Delta M^2$  is the necessary condition to observe oscillations. In  $L/E < 4/\Delta M^2$  case the detector is too close to the source and the oscillations have no time to develop[7].

**(a)** no oscillations  $L/E \ll 1/\Delta M^2$

**(b)** oscillation  $L/E \approx 1/\Delta M^2$

**(c)** oscillation  $L/E \gg 1/\Delta M^2$

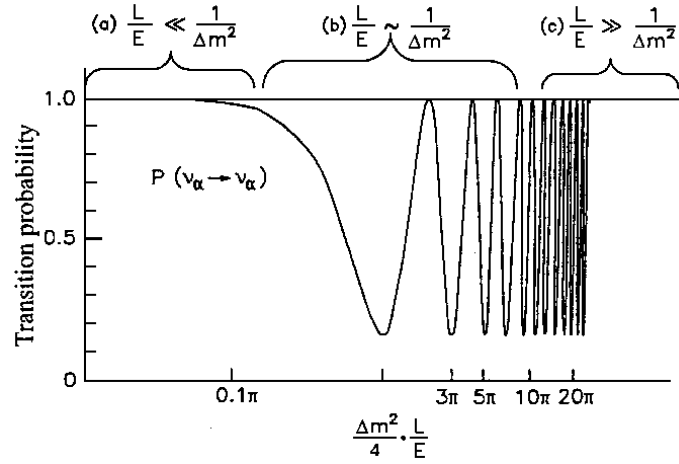


Figure 2.5: Logarithmic plot of the oscillation probability  $P(\alpha \rightarrow \alpha)$  as a function of  $L/E$  for  $\sin^2 2\theta = 0.83$ . The brackets denote three possibilities (a) no oscillations ( $L/E \ll 1/\Delta m^2$ ); (b) oscillation ( $L/E \approx 1/\Delta m^2$ ); (c) average oscillations for ( $L/E \gg 1/\Delta m^2$ ).

There are strong evidences that neutrino really change flavour in nature; the atmospheric neutrinos do so, solar neutrinos do so, reactor neutrinos do so and accelerator neutrinos studied by the Liquid Scintillator Neutrino Detector (LSND) experiment do so.

The LSND was a scintillation counter at Los Alamos National Laboratory that measured the number of neutrinos being produced by an accelerator neutrino source. The experiment collected data from 1993 to 1998. The detector consisted of a tank filled with 167 tons (50000 gallons) of mineral oil and 14 pounds of b-PDB (butyl-phenyl-bipheny-oxydiazole) organic scintillator material. Cerenkov light emitted by particle interactions was detected by an array of 1220 photomultiplier tubes. The LSND project was created to look for evidence

of neutrino oscillation, and its results conflict with the standard model expectation of only three neutrino flavours, when considered in the context of other solar and atmospheric neutrino oscillation experiments[30, 36].

In the CHORUS Experiment[44, 45, 46, 47]  $\nu_\mu \rightarrow \nu_\tau$  oscillation was studied. It was planned to find out the existence of the rare and important phenomenon of neutrino oscillation due to the different non-zero values of neutrino masses. CHORUS Detector is designed to give a direct observation of the  $\tau^-$  neutrino and the existence of  $\nu_\mu \rightarrow \nu_\tau$  oscillation by observing  $\nu_\tau + N \rightarrow \tau^- + X$  interaction.  $\tau^-$  detection was planned via the decay channels of the  $\tau^-$  lepton, which are

$$\begin{aligned}\tau^- &\rightarrow \mu^- + \bar{\nu}_\mu + \nu_\tau \text{ with } B.R = 17.4\% \\ \tau^- &\rightarrow h^-(n\pi^0) + \nu_\tau \text{ with } B.R = 49.8\%\end{aligned}\tag{2.39}$$

In the CHORUS Experiment, the interactions due to the nearly pure  $\nu_\mu$  beam which was generated by the CERN SPS accelerator with the average energy of 25 GeV were analyzed. The detector was designed to have high sensitivity to detect the presence of another type of neutrino,  $\nu_\tau$  which would be the sign for neutrino oscillation. Also the oscillation would prove the existence of the neutrino's mass and it would give the value of the mass of the  $\tau^-$  neutrino. The physics motivation is that if neutrino oscillations are observed, the  $\tau^-$  neutrino mass can be calculated from kinematics of  $\tau^-$  decays. For this purpose, the CERN neutrino beam is sent towards the 800 kg of nuclear emulsion target in a hybrid detector system in order to search for the appearance of  $\nu_\tau$  CC

interaction in the emulsion. The nuclear emulsion target provides very good spatial resolution of few  $\mu m$  for observing short-lived particles. The signature of  $\nu_\mu \rightarrow \nu_\tau$  oscillation is a decay kink on a secondary track due to a short-lived  $\tau^-$  decay to its daughters.

The nuclear emulsion target was scanned with the automatic scanning system completely and sensitivities of the limits are improved. No signal was found and upper limit of 2.4  $\tau$ -decays is given[48]. This can be converted to an oscillation probability of

$$P(\nu_\mu \rightarrow \nu_\tau) \leq 3.4 \times 10^{-4} \quad (2.40)$$

On the other hand, NOMAD (Neutrino Oscillation MAgnetic Detector)[49] at CERN used drift chambers as a target and tracking medium, with the chamber walls as interaction targets and the chambers for precise tracking. In the experiment kinematical criteria is used to search for  $\nu_\tau$  and did not observe any oscillation signal as well[50, 51]. In NOMAD experiment 55 candidates observed with the expectation of 58 background events and an upper limit for the oscillation probability was given as[7]

$$P(\nu_\mu \rightarrow \nu_\tau) \leq 2 \times 10^{-4} \quad (2.41)$$

In the studies of atmospheric neutrinos, oscillation of  $\nu_\mu \rightarrow \nu_\tau$  and  $\nu_2 \leftrightarrow \nu_3$  mixing were studied. The atmospheric neutrinos are produced in the Earth's atmosphere by cosmic rays, and then detected in an underground detector. Incident on this detector are neutrinos coming from all directions in the same rate,

created all around the Earth in the atmosphere. For neutrino energies above a few  $GeV$ , the flux of cosmic rays which produce the atmospheric neutrino is isotropic. Consequently, these neutrinos are being created at the same rate all around the Earth. The most compelling evidence that something very interesting happens to these atmospheric neutrinos is that the detected upward-going atmospheric  $\nu_\mu$  flux  $\phi_U$  differs from the corresponding downward-going flux  $\phi_D$ . The underground Super-Kamiokande (SK) detector finds that for multi- $GeV$  atmospheric muon-neutrinos there is strong disagreement with the requirement that upward and downward flux be equal[37].

$$\frac{\text{Flux up } (-1.0 < \cos \theta_Z < -0.2)}{\text{Flux down } (+0.2 < \cos \theta_Z < +1.0)} = 0.54 \pm 0.04 \quad (2.42)$$

Thus, some mechanism must be changing the  $\nu_\mu$  flux as the neutrinos travel to the detector. In principle, upward-going (long distance travelling) muon neutrinos could be disappearing, not as a result of oscillation, but also through decay into invisible daughters. This possibility is theoretically less likely than oscillation. The most attractive candidate for this mechanism is the oscillation  $\nu_\mu \rightarrow \nu_\tau$  of the muon neutrinos into neutrinos  $\nu_\tau$  of another flavour. Since the upward-going muon neutrinos come from the atmosphere on the opposite side of the Earth from the detector, they travel much farther than the downward-going ones to reach the detector. Thus, they have more time to oscillate away into the other flavour, which explains why  $Flux\ Up < Flux\ Down$ . From reactor experimental limits on  $P(\bar{\nu}_e \rightarrow \bar{\nu}_\mu)$  [38], which assuming  $CPT$  invariance, are

also limits on  $P(\nu_e \rightarrow \nu_\mu)$ , we know that  $\nu_?$  is not a  $\nu_e$ . Thus,  $\nu_?$  is a  $\nu_\tau$ , a sterile neutrino  $\nu_s$ , or sometimes one sometimes the other. All of the detailed SK atmospheric neutrino data are well-described by the hypothesis that the oscillation is purely  $\nu_\mu \rightarrow \nu_\tau$ , and that is a quasi-two-neutrino oscillation[39] with splitting  $\Delta m_{atm}^2$  in the 90% CL range of

$$1.3 \times 10^{-3} eV^2 \lesssim \Delta m_{atm}^2 \lesssim 3.0 \times 10^{-3} eV^2$$

and a mixing angle  $\theta_{atm}$  with

$$\sin^2 2\theta_{atm} > 0.9 \tag{2.43}$$

The oscillation interpretation of the atmospheric neutrino data has received support from the KEK to Kamioka (K2K) long-baseline experiment. This experiment produces a  $\nu_\mu$  beam using an accelerator, measures the beam intensity with a complex of near detectors, and then measures the  $\nu_\mu$  flux still in the beam 250 *km* away using the SK detector. Whereas 80  $\nu_\mu$  events would be expected in SK if there were no oscillation, and 52 events would be expected if oscillation were occurring with the parameters that fit the atmospheric data, 56 events are detected[40]. In spite of low statistics, this result is very consistent with oscillation.

The K2K evidence for oscillation is strengthened by this experiment's result analysis of the shape of the  $\nu_\mu$  energy spectrum at both the near and SK (far) detectors[41]. When the spectral information is taken into account, it is found



that for maximal mixing, the 90%  $CL$  allowed range for the  $(mass)^2$  splitting  $\Delta m_{atm}^2$  is

$$1.5 \times 10^{-3} eV^2 \lesssim \Delta m_{atm}^2 \lesssim 3.9 \times 10^{-3} eV^2 \quad (2.44)$$

This is very consistent with the range given in Equation (2.43) found from the atmospheric data[35].

In the studies of the solar neutrinos, various experiments (Homestake, Kamio-kande, GALLEX, SAGE, Super-Kamiokande, SNO etc.) showed that observed solar neutrino flux is less than the theoretical calculations of SM flux predictions[33]. Finally SNO Experiment in Canada solved the solar neutrino puzzle. The Sudbury Neutrino Observatory (SNO) Experiment using a deuteron target in the form of heavy water studies the measurements of solar neutrino flux in three different channels. While the flavour-dependent Elastic Scattering (ES) and Charged-Current (CC) channels are not match theoretical prediction, the flavour-independent Neutral-Current (NC) channel agree with the predictions of SM[42]. This results shows that the theoretical predictions of SM flux of neutrino is calculated correctly and when the neutrinos are travelling on the way to Earth they change the flavour, implies that neutrino oscillation. In addition in KamLAND experiment in Japan, the oscillation is observed by using reactor anti-neutrinos emitted from the many nuclear power reactors with an average distance of 180  $km$ [43]. From the combined fit of the solar and reactor neutrino

data the solar neutrino mass and mixing angle is obtained as[6]

$$\begin{aligned}\Delta m_{\odot}^2 &= 8.0 \pm_{0.4}^{0.6} \times 10^{-5} \text{ eV}^2 \\ \tan^2 \theta_{\odot} &= 0.45 \pm_{0.07}^{0.09}\end{aligned}\tag{2.45}$$

Considering the atmospheric and solar neutrino results given in Equations (2.43) and (2.45) are due to  $\nu_2 \leftrightarrow \nu_3$  and  $\nu_1 \leftrightarrow \nu_2$  oscillations, respectively;

$$\begin{aligned}\Delta m_{23}^2 &= \Delta m_{atm}^2; & \theta_{23} &= \theta_{atm} \\ \Delta m_{12}^2 &= \Delta m_{\odot}^2; & \theta_{12} &= \theta_{\odot}\end{aligned}\tag{2.46}$$

Although the oscillation of  $\nu_e \rightarrow \nu_{\tau}$  and  $\nu_1 \leftrightarrow \nu_3$  mixing are not observed experimentally yet, only upper limit from reactor experiment CHOOZ exists for  $\theta_{13}$ . From bounds on the oscillation of reactor  $\bar{\nu}_e$ ;

$$\begin{aligned}\Delta m_{13}^2 &\simeq \Delta m_{23}^2 = (1.3 - 3.0) \times 10^{-3} \text{ eV}^2 \\ \sin^2 \theta_{13} &\lesssim 0.03\end{aligned}\tag{2.47}$$

with 90% *CL*[52].

The results from the oscillation experiments in  $(\Delta m^2, \theta)$  parameter space are summarized in Figure 2.6.

From Equation (2.43) with the assumption of maximal atmospheric neutrino

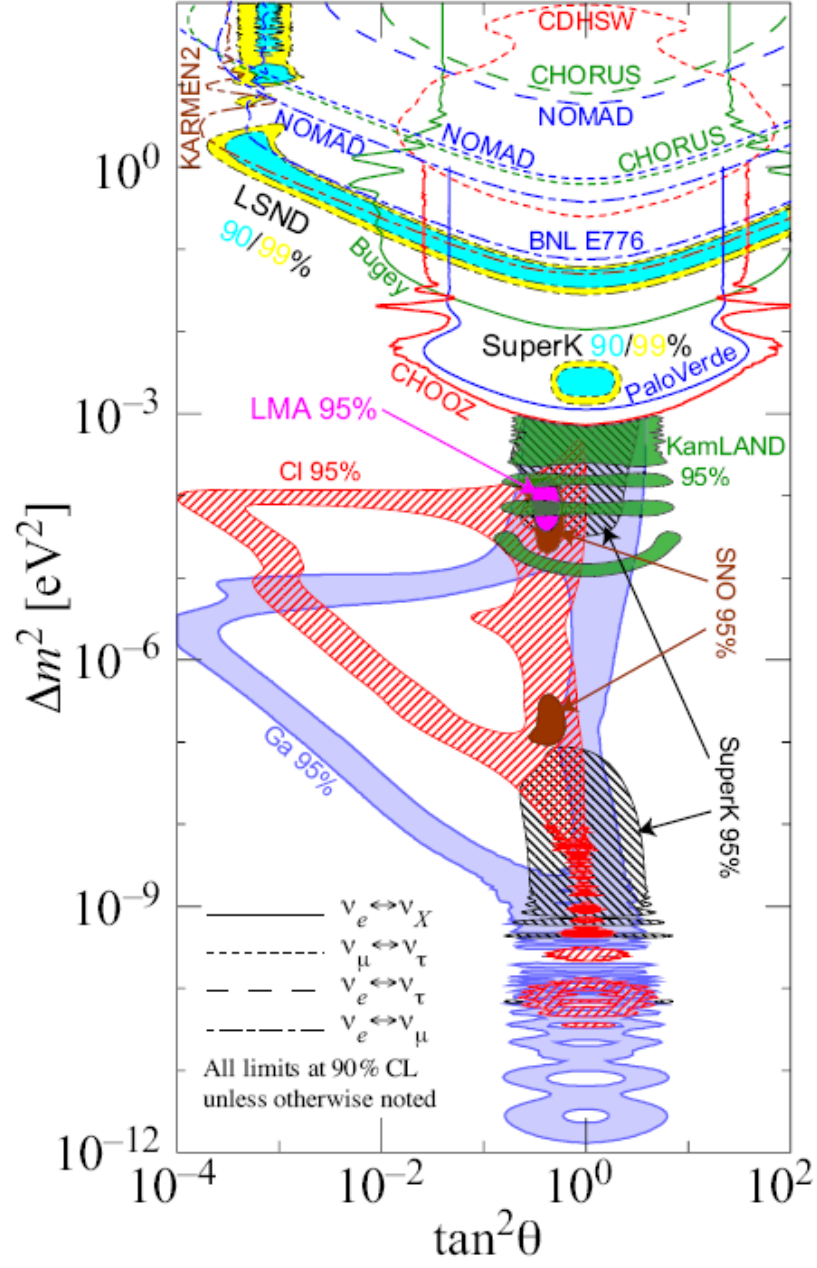


Figure 2.6: The exclusion plot of the neutrino experiments in  $(\Delta m^2, \theta)$  parameter space for different flavor oscillation. The allowed regions of the experiments are shown with different shading region.

mixing angle,  $\theta_{23} \simeq 45^\circ$ , the mixing matrix  $U$  in Equation (2.32) simplifies to

$$U \sim \begin{array}{c} \nu_e \\ \nu_\mu \\ \nu_\tau \end{array} \begin{array}{ccc} \nu_1 & \nu_2 & \nu_3 \\ \left( \begin{array}{ccc} \cos \theta_{12} & \sin \theta_{12} & e^{i\delta} \sin \theta_{13} \\ -\sin \theta_{12}/\sqrt{2} & \cos \theta_{12}/\sqrt{2} & 1/\sqrt{2} \\ \sin \theta_{12}/\sqrt{2} & -\cos \theta_{12}/\sqrt{2} & 1/\sqrt{2} \end{array} \right) \end{array} \quad (2.48)$$

with unknown mixing angle  $\theta_{13}$  and the CP-violating phase  $\delta$ . Here solar mixing angle is  $\theta_\odot = \theta_{12}$  defined in Equation (2.45) such that  $\theta_{12} \simeq 34^\circ$  and  $\theta_{13}$  is small such that  $\cos \theta_{13} \simeq 1$ . A three-neutrino (mass)<sup>2</sup> spectrum that accounts for the flavour changes of the solar and atmospheric neutrinos is depicted in Figure 2.7. The colour-codes denote the compositions of the various mass eigenstates for normal and inverted hierarchies. Since the oscillation experiment results are only sensitive to  $\Delta m^2$ 's, absolute scale of mass eigenstates of  $m_i$  remains unknown.

The future afford on neutrino oscillation experiments is to determine the unknown parameters,  $\theta_{13}$  and  $\delta$  in  $U$ , construct the mass eigenstate scale to differentiate the two possible mass hierarchies, and to diagnose the neutrino is whether Dirac or Majorana type. For these purposes there are some experiments with accelerator neutrinos such as from Fermilab to the MINOS experiment 730 *km* away, planned experiment from CERN to ICARUS and OPERA Experiments at Grand Sasso also 730 *km* away, and another planned experiment T2K from Tokai, Japan to Super-Kamiokande detector 295 *km* away. The

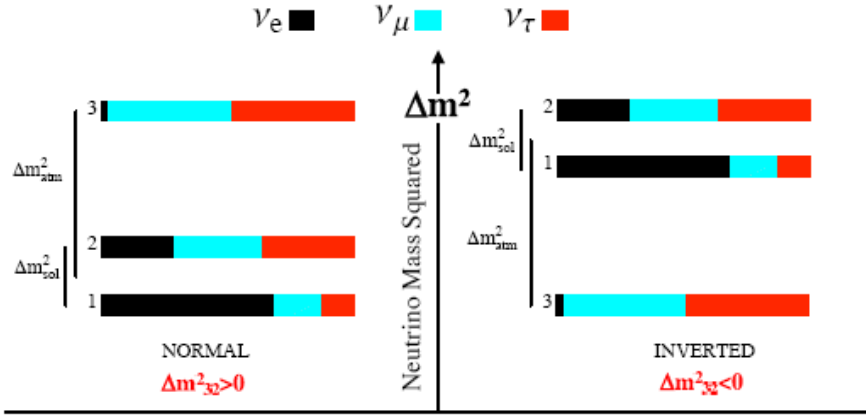


Figure 2.7: The neutrino normal and inverted hierarchy mass spectra showing how to constitute of the neutrino flavour based on positive results from neutrino oscillation experiments. The inverted scheme is characterized by a  $\Delta m_{23}^2 = m_3^2 - m_2^2 < 0$ .

goals will be improve on the  $\Delta m_{23}^2$  and  $\theta_{23}$  measurement, detect  $\nu_\tau$  appearance explicitly to confirm  $\nu_\mu \rightarrow \nu_\tau$  oscillation, and measure  $\theta_{13}$  by searching for  $\nu_\mu \rightarrow \nu_e$  oscillation[6]. Another experimental effort to measure  $\theta_{13}$  is the Daya Bay Neutrino Experiment in China. The Daya Bay Neutrino Experiment is a neutrino-oscillation experiment designed to measure the mixing angle  $\theta_{13}$  using anti-neutrinos produced by the reactors of the Daya Bay Nuclear Power Plant. The goal of the Daya Bay experiment is a measurement of  $\sin^2 2\theta_{13}$  to 0.01 or better, an order of magnitude better sensitivity than the CHOOZ limit. A 1% or better measurement will require high statistical precision and good measures to reduce systematic uncertainties[53].

## CHAPTER 3

### NEUTRINO ELECTRON SCATTERING

The basic electroweak process for  $\nu - e^-$  scattering can be of the form[7]

$$\begin{aligned}
 \nu_x + e^- &\rightarrow \nu_x + e^- & \bar{\nu}_x + e^- &\rightarrow \bar{\nu}_x + e^- \\
 \nu_e + e^- &\rightarrow \nu_e + e^- & \bar{\nu}_e + e^- &\rightarrow \bar{\nu}_e + e^-
 \end{aligned} \tag{3.1}$$

where  $\nu_x$  represents  $\mu$  or  $\tau$  type neutrino. The  $\mu$  or  $\tau$  type neutrino-electron scattering can only happen via neutral current ( $NC$ ) interaction, on the other hand, electron type neutrino-electron scattering can happen both neutral and charged current ( $CC$ ) interactions. So that in the  $\nu_e + e^-$  scattering both  $NC$  and  $CC$ , and their interference terms contribute to the cross sections. The Feynman diagrams of this interaction are shown in Figure 3.1.

The Lagrangian of  $NC$  for  $\nu - e^-$  scattering can be written as;

$$\mathcal{L}^{NC} = -\frac{G_F}{\sqrt{2}} [\bar{\nu}_e \gamma^\alpha (1 - \gamma_5) \nu_e] [\bar{e} \gamma_\alpha (g_V - g_A \gamma_5) e] \tag{3.2}$$

with coupling constants  $g_V, g_A$  from the prediction of Glashow-Weinberg-Salam

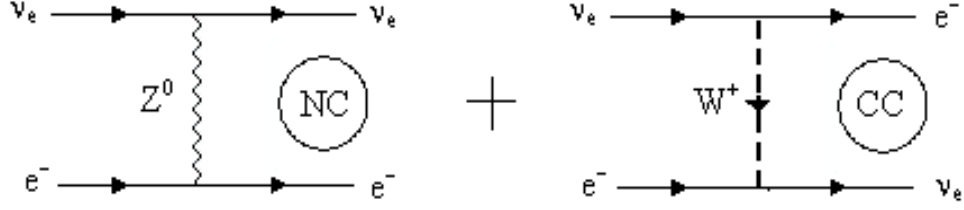


Figure 3.1: Feynman diagrams for neutrino-electron  $NC$  and  $CC$  interactions.

(GWS) model which are;

$$g_V = 2 \sin^2 \theta_W - \frac{1}{2} \quad \text{and} \quad g_A = -\frac{1}{2}$$

In addition  $CC$  interaction term can be written of the form;

$$\begin{aligned} \mathcal{L}^{CC} &= -\frac{G_F}{\sqrt{2}} [\bar{e} \gamma^\alpha (1 - \gamma_5) \nu_e] [\bar{\nu}_e \gamma_\alpha (1 - \gamma_5) e] \\ &= -\frac{G_F}{\sqrt{2}} [\bar{\nu}_e \gamma^\alpha (1 - \gamma_5) \nu_e] [\bar{e} \gamma_\alpha (1 - \gamma_5) e] \end{aligned} \quad (3.3)$$

After a detailed calculation[54] expected differential cross sections can be obtained for  $\bar{\nu}_e - e$  scattering as;

$$\frac{d\sigma_{SM}}{dT}(\bar{\nu}_e e) = \frac{G_F^2 m_e}{2\pi} \left[ \begin{aligned} &(g_V - g_A)^2 + (g_V + g_A + 2)^2 \left(1 - \frac{T}{E_\nu}\right)^2 \\ &- (g_V - g_A)(g_V + g_A + 2) \frac{m_e T}{E_\nu^2} \end{aligned} \right] \quad (3.4)$$

and in case of magnetic moment, the magnetic moment  $\mu_\nu$  term given in Equation (3.5) should be added to the cross section;

$$\left( \frac{d\sigma}{dT} \right)_{\mu_\nu} = \frac{\pi \alpha_{em}^2 \mu_\nu^2}{m_e^2} \left[ \frac{1 - T_e/E_\nu}{T_e} \right] \quad (3.5)$$

where  $T_e$  is the kinetic energy of the electron and  $E_\nu$  is the energy of neutrino. The magnetic moment  $\mu_\nu$  term given in Equation (3.5) has a  $1/T$  dependence. By decreasing energy the magnetic moment term become dominant in the

cross section. Accordingly, experimental searches for neutrino magnetic moment should focus on the reduction of the threshold (usually background-limited) for the lower recoil electron energy.

The signature of the signal is a single electron in the final state[17]. In other words, in the experiments what can be measured is the recoil energy of electron. Therefore, the cross sections for the process of  $\bar{\nu}_e - e^-$  and  $\nu_e - e^-$  provide information on the electro-weak parameters of  $g_V$ ,  $g_A$  and  $\sin^2 \theta_W$ ; are sensitive to the small neutrino magnetic moments ( $\mu_\nu$ ) and mean square charged radius  $\langle r^2 \rangle$ . By measuring the cross sections (3.6) the constants  $g_V$ ,  $g_A$  and  $\sin^2 \theta_W$  can be determined. They are the most realistic systems, where the interference effects between  $Z$  and  $W$  exchanges can be studied. For each fixed measured value of  $\sigma(\nu e)/\sigma_0$  one obtains an ellipsoid in the  $g_V$ ,  $g_A$  plane as shown in Figure 3.2 where  $\sigma_0$  is the predicted integrated  $V - A$  cross section which is  $2G_F^2 m_e (\hbar c)^2 E_\nu / (3\pi) = 5.744 \times 10^{-42} \text{cm}^2 \times E_\nu / \text{GeV}$ . Therefore, investigations of  $\bar{\nu}_e e$  cross sections with reactor neutrino allow one can study electro-weak physics at the  $\text{MeV}$  range, to probe charged and neutral currents interference, and look for an anomalous neutrino magnetic moment[55].

Since nuclear Power Plants are abundant sources of  $\bar{\nu}_e$  at  $\text{MeV}$  range, by using nuclear power plant's neutrinos one can measure weak interaction parameters in that untested lower energy. The small cross section requires experiments with a large mass detector and a high intensity neutrino beam to get a measurable



and reasonable event rate. Reactor neutrinos provide a sensitive probe for laboratory searches of  $\mu_{\bar{\nu}_e}$ , taking advantages of the high  $\bar{\nu}_e$  flux, low  $E_\nu$  and better experimental control via the reactor *ON/ OFF* comparison, as well[56]. Previous experiments focused on the interactions of  $\bar{\nu}_e + p \rightarrow e^+ + n$  since this channel have large cross sections and very distinct experimental signature of prompt  $e^+$  followed by a delayed neutron capture. Using this interaction, the reactor neutrino spectrum has been measured to a precision of 2% in the  $3 - 7 \text{ MeV}$  range from Bugey Experiment[57]. The only other processes measured at the  $\text{MeV}$  range for  $\bar{\nu}_e$  are  $\bar{\nu}_e - e^-$ [58, 59, 60] and  $\bar{\nu}_e - \text{deuteron}$ [61, 62] interactions, and their accuracies are at the 30 – 50% and 10 – 20% range, respectively. The experimental situations are summarized in Table 7.1.

Using nuclear power plants as strong source of  $\bar{\nu}_e$ , the reaction  $\bar{\nu}_e + e^- \rightarrow \bar{\nu}_e + e^-$  was observed using a 15.9 *kg* of plastic scintillation target in a composite plastic-NaI-liquid detector exposed to a  $\bar{\nu}_e$  flux of  $2.2 \times 10^{13} \text{ cm}^{-2} \text{ sec}^{-1}$  from an 1800 *MW* fission reactor by F. Reines et al. in Savannah-River Experiment[58].

The cross sections of

$$\begin{aligned} \sigma(\bar{\nu}_e e) &= (0.87 \pm 0.25) \times \sigma_0 & 1.5 < E_e < 3.0 \text{ MeV} \\ \sigma(\bar{\nu}_e e) &= (1.70 \pm 0.44) \times \sigma_0 & 3.0 < E_e < 4.5 \text{ MeV} \end{aligned} \quad (3.6)$$

were obtained. In particularly, a re-analysis[63] of Savannah-River Experiment results[58], based on an improved reactor neutrino spectrum and the Standard Model  $\sin^2 \theta_W$  value, suggested that the measured  $\bar{\nu}_e - e$  cross sections at 1.5–3.0

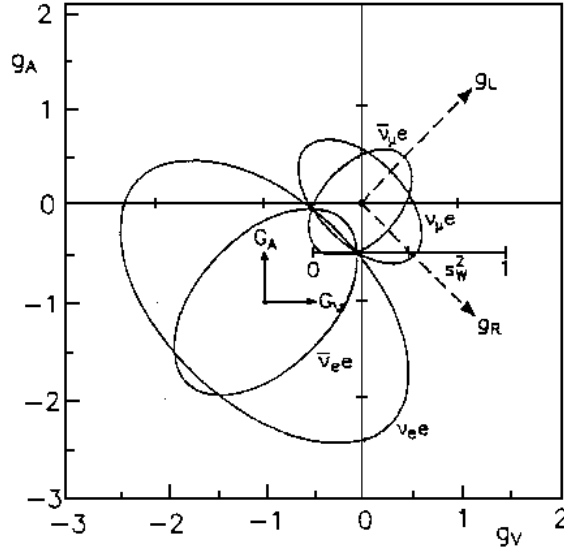


Figure 3.2: Sensitivities of  $\nu_\mu e$ ,  $\bar{\nu}_\mu e$ ,  $\nu_e e$  and  $\bar{\nu}_e e$  cross-section measurements to the different region in the  $g_A - g_V$  parameter space.

and  $3.0 - 4.5 \text{ MeV}$  are  $1.35 \pm 0.4$  and  $2.0 \pm 0.5$  times larger than the expected values, respectively. There are motivations to make an improvement on these measurements to get better results and to investigate detection techniques[55].

The TEXONO physics program with CsI(Tl) scintillating crystal detector is based on the reactor neutrino to measure electron-neutrino scattering cross section and consequently determine the  $\sin^2 \theta_W$  value. The measurable nuclear and electron recoil energy spectra due to reactor  $\bar{\nu}_e$  due to  $SM$  [ $\bar{\nu}_e e(SM)$ ] and for the effects of magnetic moment  $\mu_\nu$  [ $\bar{\nu}_e e(MM)$ ] in the  $\bar{\nu}_e - e$  scatterings[63] as well as in neutrino coherent scatterings on the nuclei [ $\bar{\nu}_e N(SM)$  and  $\bar{\nu}_e N(MM)$ ], respectively are shown in Figure 3.3.

It was recognized that due to the uncertainties in the modelling of the

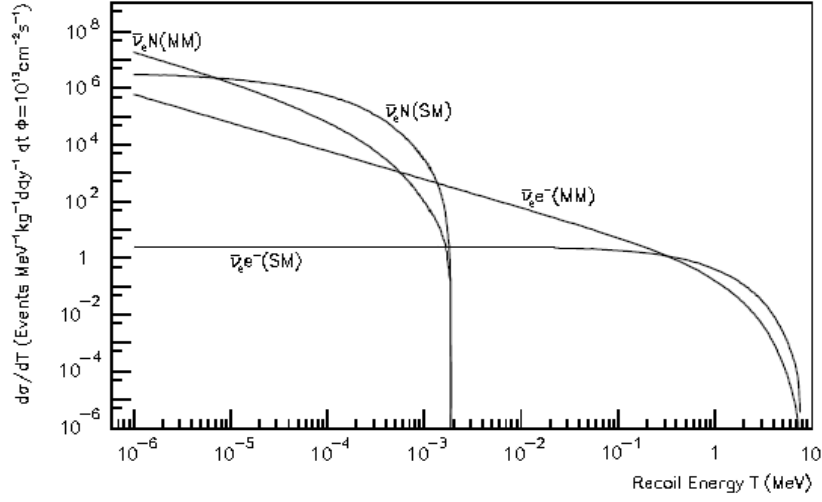


Figure 3.3: Differential cross section of SM [ $\sigma(SM)$ ] and in case of magnetic moment of  $10^{-10} \mu_B$  [ $\sigma(\mu_\nu)$ ] with respect to recoil energy for  $\bar{\nu}_e - e^-$  and coherent  $\bar{\nu}_e - N$  scatterings at a reactor neutrino flux of  $10^{13} \text{cm}^{-2} \text{s}^{-1}$ .

low-energy part of the reactor neutrino spectra[66], experiments to measure  $\sigma[\bar{\nu}_e e(SM)]$  with reactor neutrinos should focus on the higher electron recoil energies ( $T > 1.5 \text{ MeV}$ ), while magnetic moment  $\mu_\nu$  searches should base on measurements with  $T < 100 \text{ keV}$ . The goal is to push the detection threshold as low as possible to enhance the sensitivities in magnetic moment search[67]. In addition, observation of the  $\bar{\nu}_e N(SM)$  would require detectors with sub-keV sensitivities[68].

Electron anti-neutrinos are produced in a nuclear reactor through  $\beta$ -decays from unstable nuclei fission products of the four major elements in the fuel:  $^{235}\text{U}$ ,  $^{238}\text{U}$ ,  $^{239}\text{Pu}$ ,  $^{241}\text{Pu}$  and  $^{239}\text{U}$ , following the neutron capture on the  $^{238}\text{U}$  fuel. Hundreds of different daughter nuclei are involved, each having its own

decay life-times and branching ratios as well as Kurie distributions which are not completely known. To calculate the overall  $\phi(\bar{\nu}_e)$ , one must base on inputs derived from two alternative approaches: (I) modellings on the level densities and nuclear effects[69], or (II) the measurements of  $\beta$ -spectra due to neutron hitting the fissile isotopes[70].

In particularly, there is no measurement of  $\phi(\bar{\nu}_e)$  below  $E_\nu \sim 2.8 \text{ MeV}$ , and theoretically this energy range has not been calculated in a systematic way. There is only one modelling which is based on summation of the allowed beta decays of all fission fragments[63], with its rather complicated spectrum discontinuities due to the end-point effects of the many  $\beta$ -spectra. The modeling of the  $\bar{\nu}_e$  energy spectra above  $3 \text{ MeV}$  is consistent with measurements at the  $< 5\%$  level Bugey-3 Experiment[57], while the low energy portion is subjected to much bigger uncertainties since the evaluation of  $\phi(\bar{\nu}_e)$  at energy below  $2 \text{ MeV}$  is much more complicated and there are many effects which one may have to take into account. Many input parameters remain unknown and there are no measurements to cross-check. Consequently, the  $\phi_e(SM)$  recoil spectra below the  $\text{MeV}$  range in Figure 3.3 were subjected to large uncertainties[56]. The errors in the evaluation of  $\phi(\bar{\nu}_e)$  at low energies have high tendencies to be under-estimations, that is due to some physical process are not accounted for. This would give rise to an excess of events which may mimic positive signatures for anomalous effects. Therefore, one should be cautious on the derivations of

the low energy part of  $\phi(\bar{\nu}_e)$  and the estimation of their uncertainties, as well as on the conceptual design of experiment and the interpretation of data where the low energy part plays a role, such as in neutrino-electron scatterings[66].

By the standard parametrization for the reactor  $\bar{\nu}_e$  spectra, the typical fission rate at the reactor core with a thermal of  $P_{th}$  in  $GW$  is  $0.3 \times 10^{20} P_{th} s^{-1}$ , while an average about  $6 \bar{\nu}_e/fission$  are emitted. In a realistic achievable setting at a location  $10\text{ m}$  from a core with  $P_{th} = 4.5\text{ GW}$ , the  $\bar{\nu}_e$ -flux is  $6.4 \times 10^{13} cm^{-2}s^{-1}$ [71]. The Kuo-Sheng Neutrino Laboratory is located at a distance of  $28\text{ m}$  from Core#1 whose nominal thermal output is  $2.9\text{ GW}$ . The standard operation includes about 18 months of Reactor *ON* time at nominal power followed by about 50 days of Reactor outage *OFF* period when about a third of the fuel elements are replaced. Reactor operation data on the thermal power output and control rod status as functions of time and locations within the core were provided to the experiment by the Power Station. A set of software programs[72] was specifically developed, in association with the commercial *SIMULATE-3* and *COSMO-3* codes[73], both of which are extensively used in the field of nuclear reactor core analysis.

The summary of the data taking periods is listed in Table 3.1. The variations of the thermal power output for Period-II and Period-III data taking time are displayed in Figures 3.4a-b, as well as the fission rates and  $\bar{\nu}_e$ -flux of the fissile isotopes during the Period-III data taking time are illustrated in Figures 3.4c-d.

Table 3.1: Summary of the key information on the three data taking periods with HPGe.

Periods	Data Taking Calendar Time	Reactor ON Real Time (days)	Reactor OFF Real Time (days)	Average $\bar{\nu}_e$ flux ( $10^{12}cm^{-2}s^{-1}$ )
I	July 2001-Apr.2002	188.2	55.1	6.29
II	Sept.2002-Apr.2003	125.8	34.4	6.53
III	Sept.2004-Oct.2005	303.9	48.7	6.51
Total	July 2001-Oct.2005	617.9	138.2	6.44

At steady state operation, the total fission rates and the total neutrino fluxes were constant to better than 0.1% and 0.2%, respectively. Data taken during the short durations of unscheduled reactor stops were included into the Reactor-*OFF* category.

The  $\phi(\bar{\nu}_e)$ 's of the five channels, as depicted in Figure 3.5a, were adopted from Ref.[63] for the fission  $\bar{\nu}_e$ 's, while those following  $^{238}U$  neutron capture were derived from standard  $\beta$ -spectra of  $^{239}U$  and  $^{240}Np$ . The components were summed according to the relative contributions per fission, and the evaluated resulting total  $\phi(\bar{\nu}_e)$  is shown in Figure 3.5b. This spectrum was used as input in deriving the expected electron recoil spectra in Figure 3.3. The evaluated  $\bar{\nu}_e$ -fluxes for the three periods are given in Table 3.1, where the weighted average is  $6.44 \times 10^{12}cm^{-2}s^{-1}$ [56].

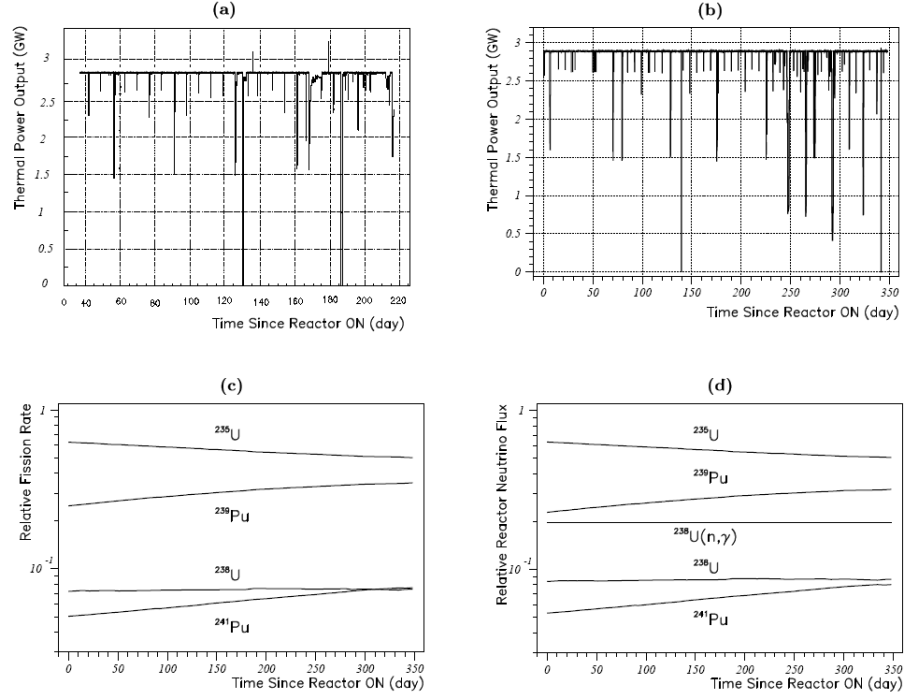


Figure 3.4: The variation of (a) and (b) the thermal power output of P-II and P-III data taking, respectively, (c) relative fission rates and (d)  $\bar{\nu}_e$ -flux of the fissile isotopes over Period-III of data taking. The reactor outage OFF period was completed on Day-0.

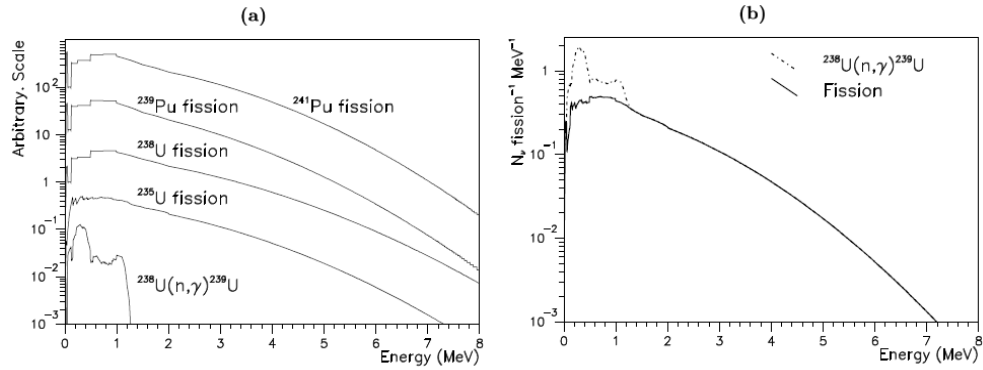


Figure 3.5: (a) Spectral shape for reactor neutrinos due to individual production channels. (b) Total spectrum at the typical power reactor operation.

## CHAPTER 4

### THE TEXONO EXPERIMENT OVERVIEW

The **T**aiwan **E**Xperiment **O**n **N**eutrin**O** (TEXONO) Collaboration was constituted in 1997, comprising scientists from Taiwan, China, Turkey, India and U.S.A. to study on Neutrino and Astrophysics[74]. Turkey, Middle East Technical University (METU) joined the TEXONO Collaboration in 2004. The Kuo-Sheng (KS) Reactor Neutrino Laboratory has been formed and performed an operation since 2001. The TEXONO Experiment commence the program by using two different detector systems, CsI(Tl) Scintillating Crystal and Ge detectors, to study on neutrino properties and interactions with matter in low energy, few  $MeV$  region. Period-I data taken by active target mass of 1.06  $kg$  of Ultra Low Background High Purity Germanium (ULB-HPGe) detector analysis was completed in 2002. The world-level sensitivities and giving the best limits on neutrino magnetic moment were achieved and the radiative decay lifetimes were measured with the international recognition[75]. For Period-II data taking (from 2002 to 2003) 186  $kg$  of CsI(Tl) crystal scintillators were added to study on



### Kuo-Sheng Nuclear Power Station : Reactor Building

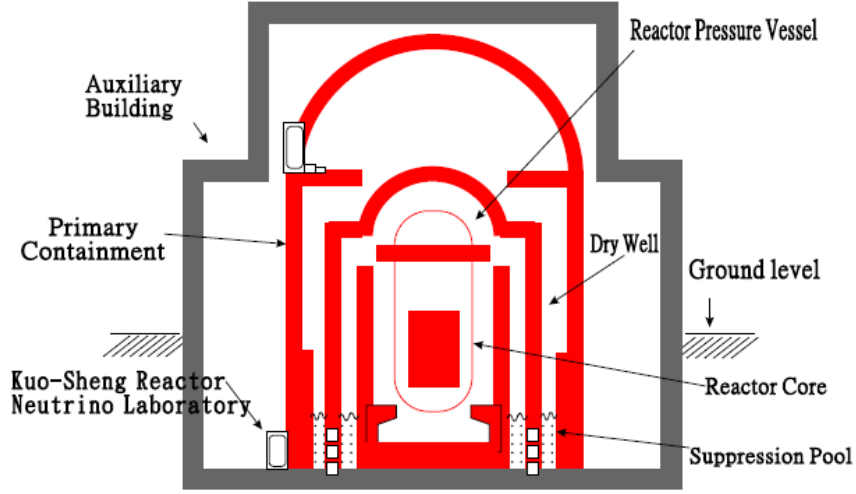


Figure 4.1: Schematic side view, not drawn to scale, of the Kuo-Sheng Reactor Building indicating the experimental site.

neutrino-electron scattering cross sections measurement. Both detector systems are operated in parallel with the same data acquisition system but independent triggers.

#### 4.1 Experimental Set-Up

The experimental set-up is placed in Kuo-Sheng Nuclear Power Plant Station at Taiwan. The reactor neutrino laboratory is located at a distance of 28 *m* from one of the reactor core and 102 *m* from the other one to study on low energy low background neutrino interactions and perform a measurement of neutrino-electron scattering cross section to determine the  $\sin^2 \theta_W$  value at the untested



Figure 4.2: The multi-purpose inner target volume where both ULB-HPGe and CsI(Tl) scintillating crystal detectors were placed with dimension of  $100 \times 80 \times 75 \text{ cm}^3$  showing the HPGe detector and shielding materials.

MeV range. Each of the cores is a boiling water reactor with 2.9 *GW* thermal power giving a total flux of about  $6.4 \times 10^{12} \text{ cm}^{-2} \text{ s}^{-1}$  at the detector site. The experimental set-up is placed the lowest level of the power plant around 12 *m* below the sea-level. Schematic view of the Nuclear Power Plant showing the experimental site, not drawn in scale, is illustrated in Figure 4.1. The inner target volume was designed for different detectors for different scientific goals. The multi-purpose inner target volume as shown in Figure 4.2 with a dimension of  $100 \text{ cm} \times 80 \text{ cm} \times 75 \text{ cm}$ , where both ULB-HPGe and CsI(Tl) scintillating crystal detectors were placed, is enclosed by  $4\pi$  passive shielding materials which have a total weight of 50 *tons*. The shielding provides attenuation to the ambient neutron and gamma background, and consists of from inside

to outside, 5 *cm* of Oxygen-Free-High-Conductivity (OFHC) copper, 25 *cm* of boron-loaded polyethylene, 5 *cm* of steel, 15 *cm* of lead, and 16 panels of 2.5 *cm* thick cosmic-ray veto (CRV) plastic scintillators with PMTs surrounding all the detector and shielding. The front view of the experimental set-up showing cosmic-ray veto panels and shielding are illustrated in Figure 4.3. Cosmic rays and their related events will be vetoed by CRV scintillator panels located in the outermost layer of shielding. 3 *m*  $\times$  1 *m* of plastic scintillators are located at top, left and right side, and 1.5 *m*  $\times$  1 *m* of them are located at front and back side. PMTs at the both ends are set into coincidence to avoid noise effect and the veto rate is kept around 5 *kHz*. Ambient radioactivity is suppressed by 15 *cm* of lead and 5 *cm* of steel. The steel layer also provides the mechanical structures to the system. Neutrons mostly cosmic-induced are slowed down by the lead and steel and then absorbed by 25 *cm* of boron-loaded polyethylene. The inner 5 *cm* of OFHC copper serves to suppress residual radioactivity from the shielding materials itself. The CsI(Tl) scintillator crystal target is placed inside an electrically shielded and air-tight box made of copper sheet. The entire target space is covered by a plastic bag flushed with dry nitrogen to prevent from background events due to the diffusion of the radioactive radon gas leak into the target region[55]. The schematic view of the shielding design is depicted in Figure 4.4.

The detectors are read out versatile electronics and data acquisition (DAQ)

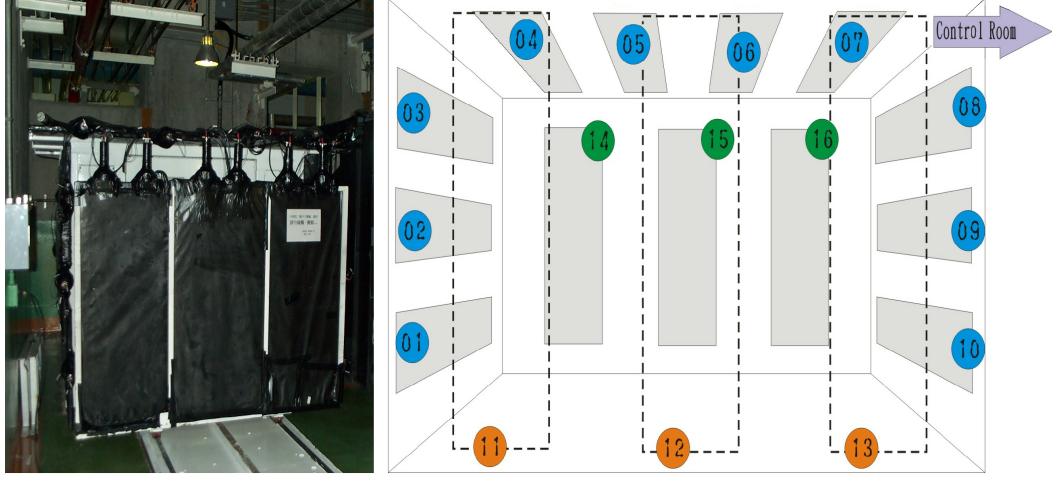


Figure 4.3: Front view of the experimental site showing the shielding and 16 cosmic ray veto pannels.

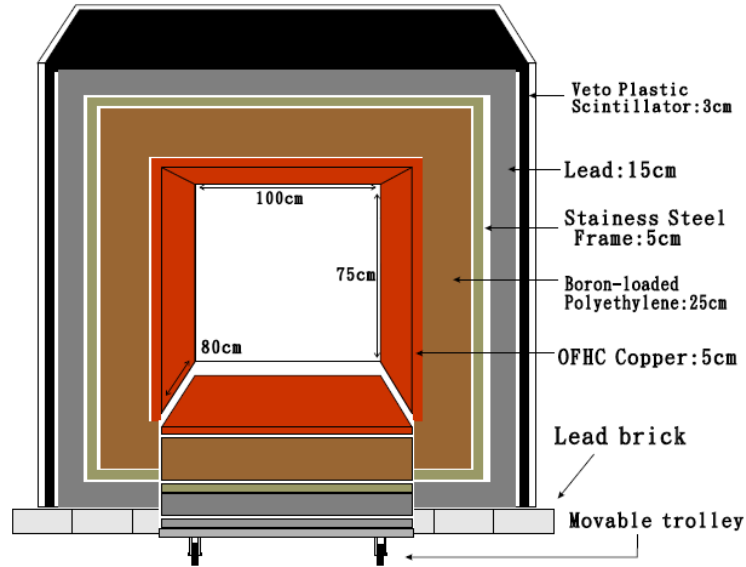


Figure 4.4: Design of the shielding for the Kuo-Sheng Neutrino Laboratory. The detectors and inner shieldings were placed inside the shielding.

systems[76] based on Flash-Analog-to-Digital-Converter (FADC) modules with 16—channels running at a clock rate of 20  $MHz$  and 8—bit resolution. Software procedures have been developed to extend the effective dynamic range from the nominal 8—bit measurement range provided by the FADC[77]. The schematic block-diagram of electronics and data acquisition system for CsI(Tl) and ULB-HPGe are illustrated in Figure 4.5 and Figure 4.6, respectively. The signals are fed to amplifiers and shapers, and finally digitized by FADC modules. The trigger condition is having anyone or more channels above a pre-set “high threshold” (typically 50 – 100  $keV$  equivalent). However, if more than 3 FADC Modules fired at the same time, the signal will be ignored. Once these conditions are fulfilled, all channels with signals above a “lower threshold” (typically 10 – 300  $keV$  equivalent) will be read out. A typical raw CsI(Tl)+PMT pulse and FADC output signal of CsI(Tl) crystal events are depicted in Figure 4.7. The logic control circuit enables complete acquisition of delayed signatures up to several  $ms$ , to record cascade events coming from decay series like  $^{238}U$ ,  $^{235}U$  or  $^{232}Th$ .

The trigger system selects relevant events to be read out, while the logic control system provides a coherent timing and synchronization for the different electronics modules. The readout allows full recording of all relevant pulse shape and timing information for as long as 500  $\mu s$  after initial trigger with a resolution of 1  $\mu s$ . After initial trigger the events are digitized for as long as 256 time-bins

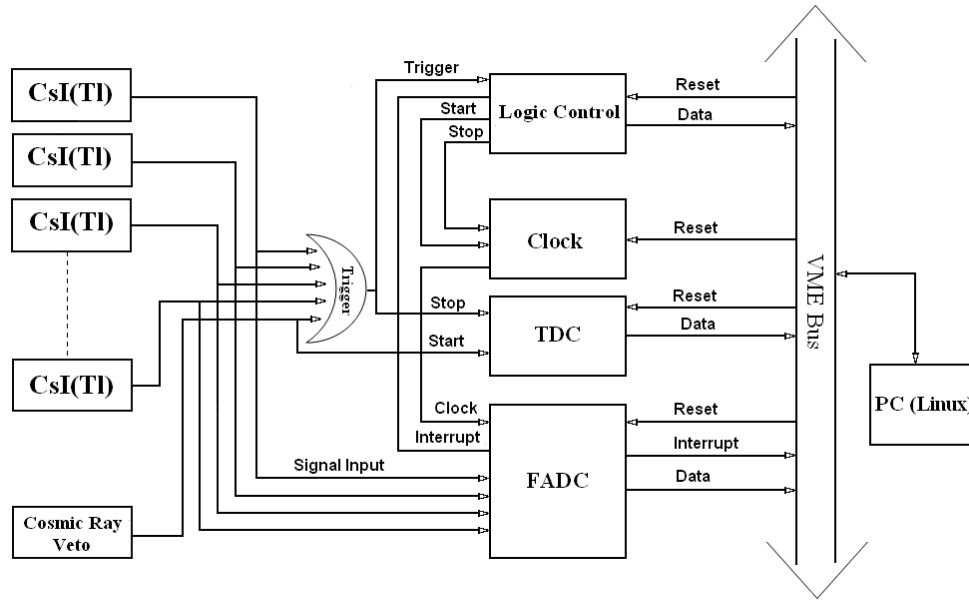


Figure 4.5: The schematic block-diagram of electronics and data acquisition system for CsI(Tl) scintillating crystal detector.

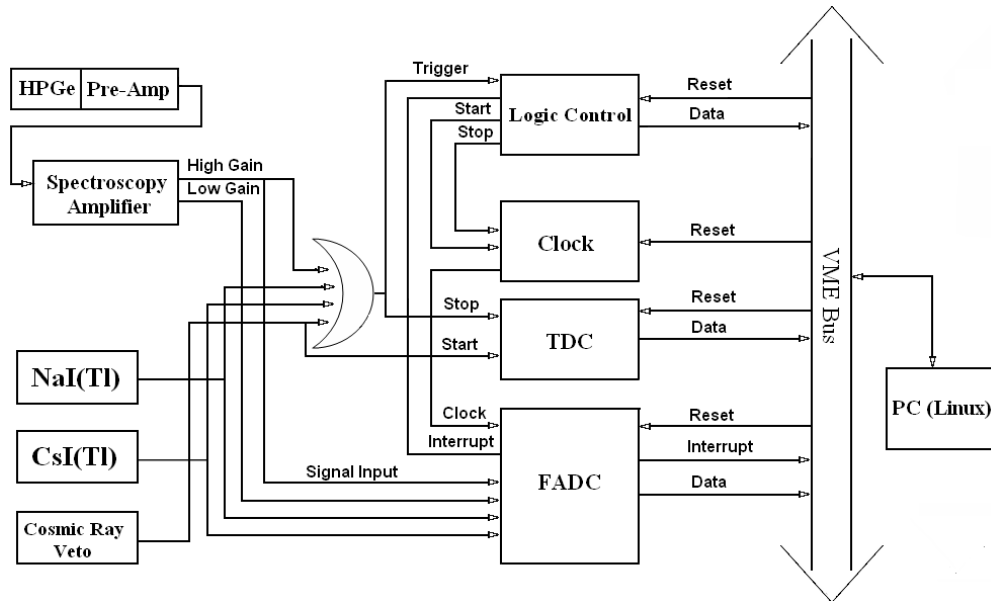


Figure 4.6: The schematic block-diagram of electronics and data acquisition system for ULB-HPGe detector.

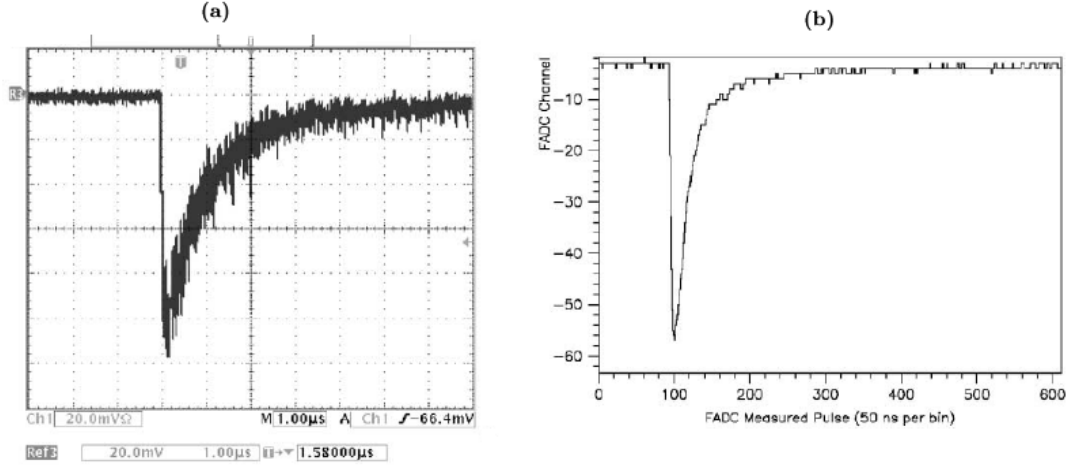


Figure 4.7: (a) Raw input signal from CsI(Tl)+PMT as recorded by a 100  $MHz$  digital oscilloscope with time axis of 1  $\mu s$  per division. (b) Output signal after shaping from the Amplifier-Shaper as recorded by the FADC with time axis of 5  $\mu s$  per 100 FADC time bin.

(12.8  $\mu s$ ) and wait for other events. To see whole part of pulse, the valid data is traced back for as long as 100 time-bins (5  $\mu s$ ) before the initial trigger. Finally, the data is read out and transferred to the host computer. The average DAQ dead time is 5.13  $\mu s$  per event. The timing information for event was recorded with a resolution of 1  $ms$ . The time differences between subsequent events and between different triggers within an event can be evaluated. The schematic view of the timing sequence in a typical event is illustrated in Figure 4.8.

The FADC, the trigger units, logic control and calibration modules are read out and controlled by a VME-based data acquisition system connected by a PCI-bus to PC running with LINUX operating system. The DAQ system provides control to the experimental running parameters, access valid data from the VME

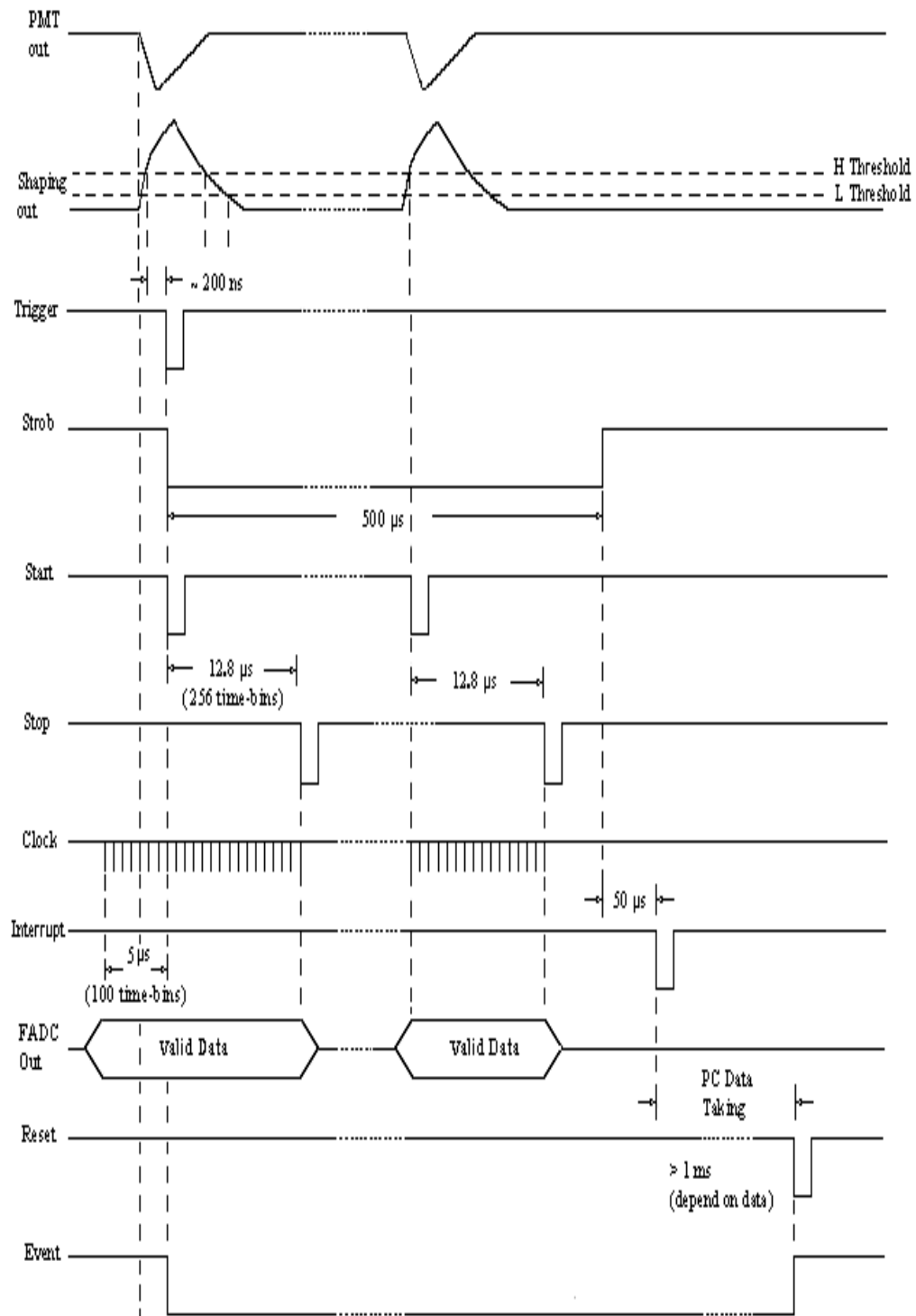


Figure 4.8: The timing sequence in a typical event for data taking.



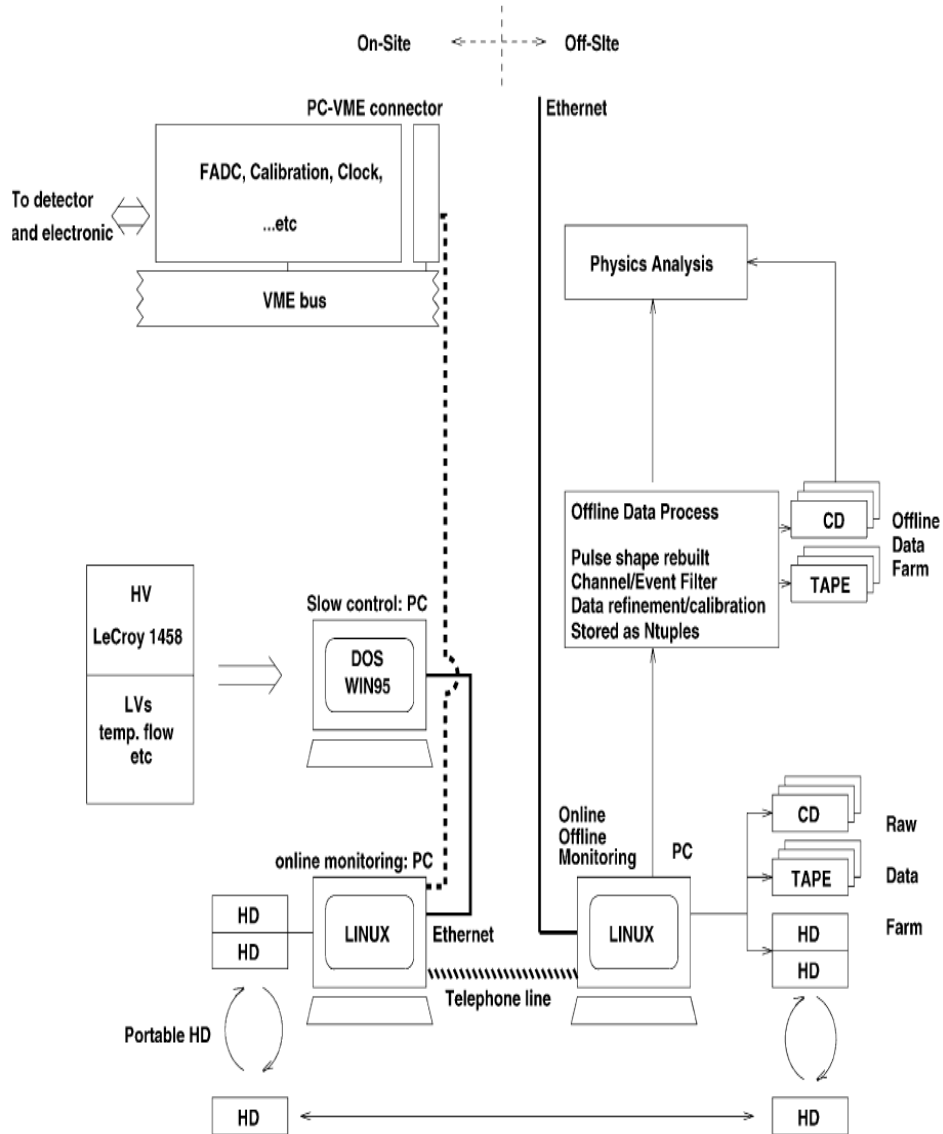


Figure 4.9: The schematic layout of the on-line monitoring and data acquisition system and its interfacing with the off-line software packages. The neutrino laboratory at reactor building is connected to the home-base laboratories at AS.

electronics modules, and save them on hard disks. The online and offline software architecture together with their inter connections is shown in Figure 4.9. On-site data taking conditions are remotely monitoring regularly from the home-based laboratories via telephone line. Data is saved in hard disks on-site and replaced at the once-per-week interval. They are duplicated and stored in cluster of multi-layer disks arrays with several *Tbyte* of memory as well as CDs for subsequent off-line analysis[55].

Data taking for both detectors were optimized with these strategies. An ULB-HPGe detector was used for measurement of anomalous neutrino interactions, magnetic moment and radiative decay lifetimes, while 200 *kg* of CsI(Tl) crystal scintillator detector was used for measurement of the Standard Model neutrino-electron scattering cross-section, and subsequently  $\sin^2 \theta_W$  value at low energies.

#### 4.1.1 The ULB-HPGe Detector

In the TEXONO Experiment a 1.06 *kg* of ULB-HPGe detector was used from July 2001 till Oct. 2005. In 2006 the Ge detector was replaced by  $4 \times (5 \text{ g})$  ULB-HPGe detector for the next generation of data taking to study on neutrino-nucleus coherent scattering. As shown in Figure 4.10, the 1.06 *kg* of ULB-HPGe detector is surrounded by NaI(Tl) and CsI(Tl) crystal scintillators as anti-Compton detectors and whole set-up is further enclosed by another 3.5 *cm*

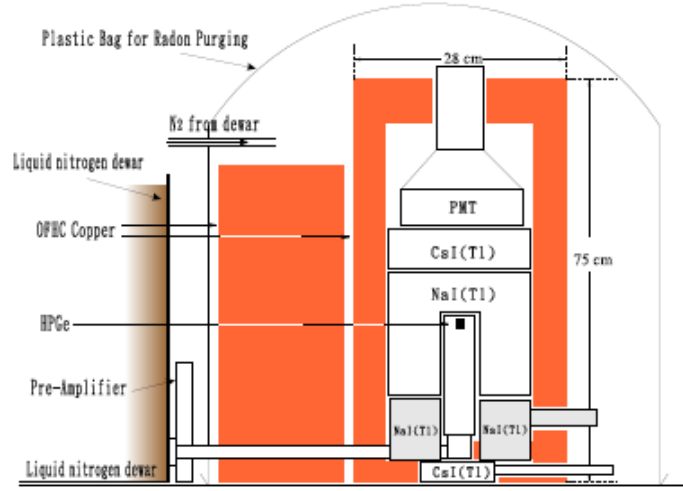


Figure 4.10: Schematic view of the HPGe detector showing with anti-Compton detectors as well as inner shieldings and radon puge system.

of OFHC copper and lead blocks, and housed in a radon shielding.

Scatterings of  $\bar{\nu}_e - e$  inside the Ge target would manifest as "*lone-events*" uncorrelated with the other detector systems. These events were extracted from raw data through selection criteria including pulse shape analysis (PSA), anti-Compton (ACV) and cosmic-ray vetoes (CRV). The efficiencies and background suppression of these cuts are listed in Table 4.1. The selection criteria and selected regions for the lone-events in data analysis techniques as well as the measured spectra in Period-III before and after the ACV and CRV cuts for the Reactor *ON* data are illustrated in Figure 4.11. As displayed in the correlation plot between pulse area and amplitude in Figure 4.11a, spurious background due to accidental and delayed "*cascade*" events were suppressed by PSA. The ACV and CRV cuts 4.11b,c suppressed Compton scattering and cosmic-ray induced

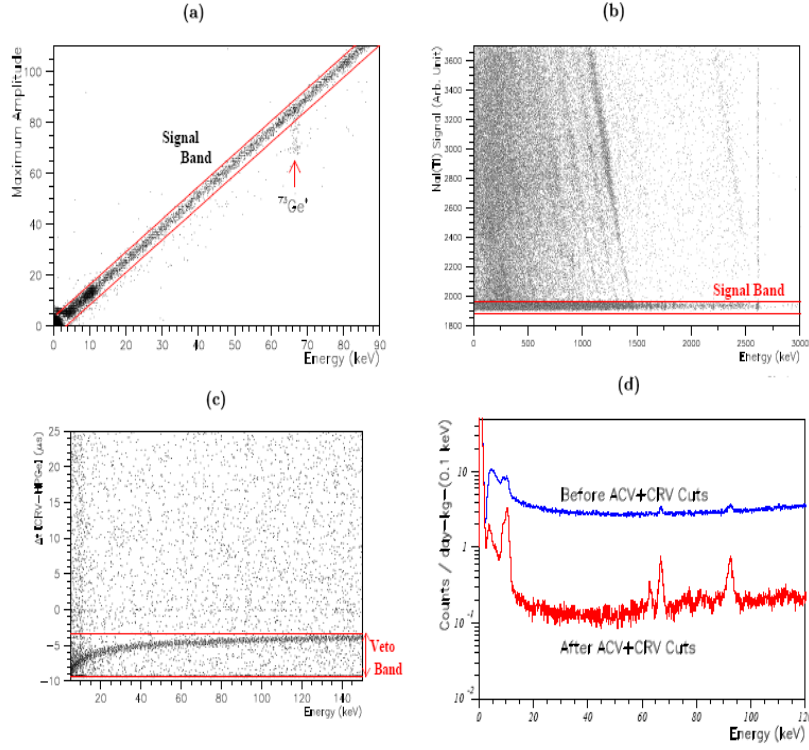


Figure 4.11: Selection procedures of the recorded pulse (a) Pulse Shape Analysis (PSA), (b) anti-Compton veto (ACV) selection, (c) Cosmic Ray Veto (CRV), (d) Measured spectra before and after the ACV and CRV cuts for the Reactor ON data in Period III.

events, respectively.

After suppression of cosmic-induced background by CRV, anti-Compton vetoes and convoluted events by PSA, a detection threshold of  $5 \text{ keV}$  and a background level of  $1 \text{ keV}^{-1} \text{ kg}^{-1} \text{ day}^{-1}$  near threshold were achieved. These are the levels comparable to underground Dark Matter Experiments. After the all cuts of ACV, CRV and PSA, the measured low energy single hit spectra in full range and below  $120 \text{ keV}$  region showing the Reactor *ON* and *OFF* periods,

Table 4.1: Summary of the event selection procedures as well as their background suppression and signal efficiency factors.

Event Selection	Background Suppression			Signal Efficiency		
Period	I	II	III	I	II	III
Raw Data	1.0	1.0	1.0	1.0	1.0	1.0
Pulse Shape Analysis (PSA)	>0.99	>0.99	>0.99	>0.99	>0.99	>0.99
Anti-Compton Veto (ACV)	0.054	0.051	0.058	0.99	0.99	0.99
Cosmic-Ray Veto (CRV)	0.92	0.85	0.80	0.95	0.94	0.93
Combined	0.050	0.043	0.046	0.95	0.93	0.92

where the magnetic moment studies carried on, are depicted in Figure 4.12. Based on 570.7 and 127.8 days Reactor *ON* and *OFF* data, respectively, at an average Reactor *ON* electron anti-neutrino flux of  $6.4 \times 10^{12} \text{ cm}^{-2} \text{ s}^{-1}$ , comparison of *ON* and *OFF* spectra shows no excess and the limit on the neutrino magnetic moments of  $\mu_{\bar{\nu}_e} < 7.2 \times 10^{-11} \mu_B$  at 90% confidence level was derived.

The combined residual spectrum for the three periods of the Reactor *ON* data over the background profiles together with the best fit  $2\sigma$  region is depicted in Figure 4.13a. As a result, the summary of the results in  $\mu_{\bar{\nu}_e}$  searches versus the achieved threshold in reactor experiments is depicted in Figure 4.13b[56].

#### 4.1.2 CsI(Tl) Crystal Scintillating Detector

A 186 kg (or 93 crystals) CsI(Tl) scintillating crystal array was used for data taking in Period-II (Jan. 2003-Nov 2003) and by adding 7 more crystals as a veto crystal on the top total weight was increased to 200 kg (or 100 crystals) and also several layer of copper bricks were added to the shielding surrounding the CsI(Tl) scintillating crystal array for the other period data taking. The

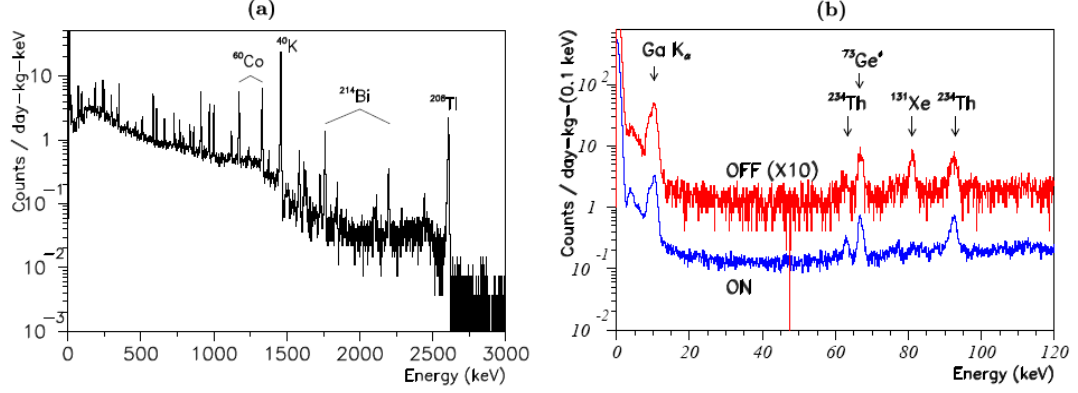


Figure 4.12: Measured spectra in Period-III after all the selection criteria were applied for (a) the full energy range and (b) the range below 120 keV relevant to the magnetic moment studies for the both Reactor ON and OFF spectra.

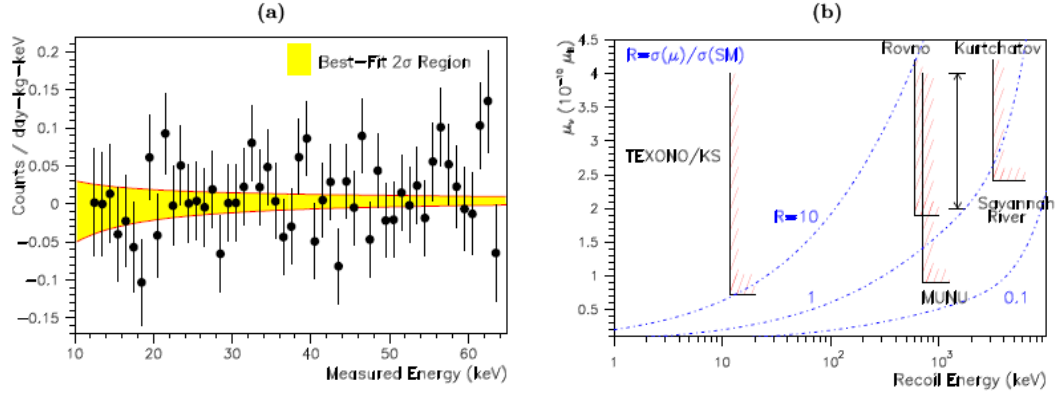


Figure 4.13: (a) The residual plot on the Reactor ON data of all period combined over the background spectra, (b) Summary of the results in the searches of the neutrino magnetic moments with reactor neutrinos in which both limits and detection thresholds of the various experiments are shown.

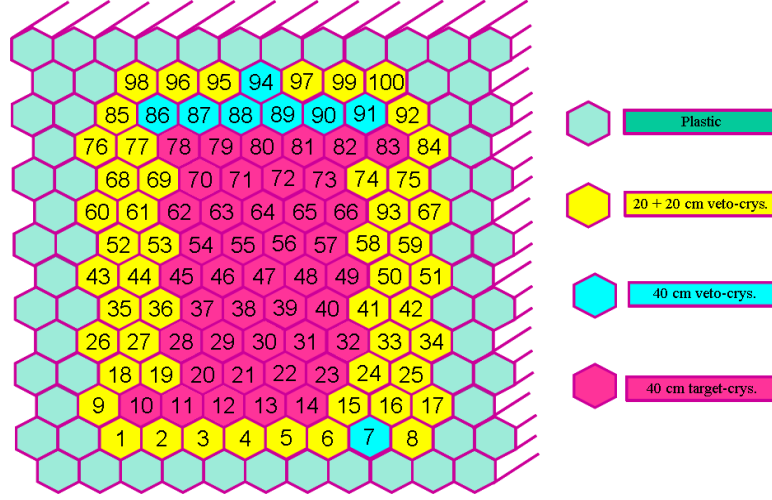


Figure 4.14: Schematic view of the CsI(Tl) scintillating crystal detector design showing 40 cm as well as 20+20 cm modules. Read out at the both ends are performed by custom design PMTs with low-activity glass.

main physics goal is to measure the Standard Model neutrino-electron scattering cross-section, and thereby to provide a measurement of  $\sin^2 \theta_W$  in the untested low-energy,  $MeV$  range. The strategy[66] is to focus on data at high ( $> 3MeV$ ) recoil energies where the uncertainties due to the reactor neutrino spectra are small.

A CsI(Tl) crystal scintillators were placed as an array and arranged in a  $12 \times 9$  matrix inside the inner target volume. The detector consists of 200  $kg$  of scintillating crystals each of which have a hexagonal-shaped cross-section with 2  $cm$  side and 40  $cm$  in length giving 2  $kg$  in mass. There are two different types of crystal modules inside the crystal array; one kind is single crystal with 40  $cm$  in length and the other kind is optically glued two pieces of 20  $cm$  crystal modules

Table 4.2: Characteristic properties of the common crystal scintillators and their comparison with typical liquid and plastic scintillators.

Properties	CsI(Tl)	NaI(Tl)	BGO	Liquid	Plastic
Density ( $g\ cm^{-3}$ )	4.51	3.67	7.13	0.9	1.0
Relative yield	0.45	1.00	0.15	0.4	0.35
Radiation length ( $cm$ )	1.85	2.59	1.12	$\sim 45$	$\sim 45$
$dE/dx$ for MIP ( $MeV\ cm^{-1}$ )	5.6	4.8	9.2	1.8	1.9
Emission peak ( $nm$ )	565	410	480	425	425
Decay time ( $ns$ )	1000	230	300	2	2
Reflecting index	1.79	1.85	2.15	1.5	1.6
Hygroscopic	slightly	yes	no	no	no

to form a 40  $cm$  module. The schematic view of the CsI(Tl) crystal array is depicted in Figure 4.14. The light output are read out at the both ends ( $Q_L$  and  $Q_R$ ) by custom designed 29  $mm$  diameter Photo-Multiplier Tubes (PMTs) with low-activity glass.

Due to some intrinsic properties, crystal scintillators are being widely used as an electromagnetic calorimeter in high energy physics for studying low background low energy experiments. The CsI(Tl) crystal scintillators offer some advantages such as it has high light yield and high photon absorption, in other words, they have short radiation length -the Tl concentration at the 400 to 2000  $ppm$  range can provide a reasonable scintillation yield. Although the modular size is smaller compare to those of liquid and plastic scintillators, it provides more efficient light transmission and collection despite of higher refractive index. The high gamma attenuation also allows full  $\gamma$  energy deposition; they are not hygroscopic, no need to use any container to seal the detector or protect crystal from ambient humidity (as required, for instance for NaI(Tl)) -this minimizes



radioactive background as well as energy loss in the passive elements which will degrade energy resolution; they are mechanically stable and easy to maintenance; their production technology is well-developed and the cost is reasonable to build a big detector for reactor neutrino experiment. The properties of CsI(Tl) crystal scintillators[78], together with those of few common scintillators, are listed in Table 4.2. The detection threshold is lower and the energy resolution of CsI(Tl) is better than typical liquid or plastic scintillator with the same modular mass, both of which are necessary for low-energy measurements[79].

With its high Z-nuclei, CsI(Tl) crystal provides strong attenuation for  $\gamma$ 's, especially at the low energy range below 500 *keV* and very good separation between  $\gamma$  and  $\alpha$  events, as well. For instance, the attenuation lengths for a 100 *keV*  $\gamma$  ray are 0.12 and 6.7 *cm* for CsI(Tl) and liquid scintillators, respectively. That is, 10 *cm* of CsI(Tl) has the same attenuation power as 5.6 *m* of liquid scintillators at this low energy. Consequently, the effects of external ambient  $\gamma$  background, like those from readout device, electronic components, construction materials, and radon diffusion are negligible after several *cm* of active veto layer. Therefore, the background at low energy will mostly originate within the fiducial volume due to internal components[55].

## CHAPTER 5

### DATA ANALYZING TECHNIQUES

The entire pulse shape, amplitude or integrated area of the pulses from the each individual crystal module, as well as the relative timing between pulses from different detector channels are recorded by DAQ system based on 16 *channel*, 20 *MHz*, 8 *bit* FADC modules. The  $n - bit$  resolution per time-bin and sampling rate of the FADC are important parameters effecting the characterization and performance of the experiment such as detector resolution, DAQ dead time, data size, data processing time, cost and so on. With 8 - *bit* resolution, FADC has dynamic range of  $2^n - 1 = 255$ . That means above this saturation level, the pulse can not be recorded totally. The pulse which has amplitude higher than 255 level is called saturated pulse, and less than 255 level is called unsaturated pulse. Typical unsaturated and saturated pulses are illustrated in Figure 5.1. Some important information of saturated pulses such as total area, rising and falling times will be lost and need to be reconstructed. By using “*Charge Summation Correction Method*” the energy reconstruction and particle identification

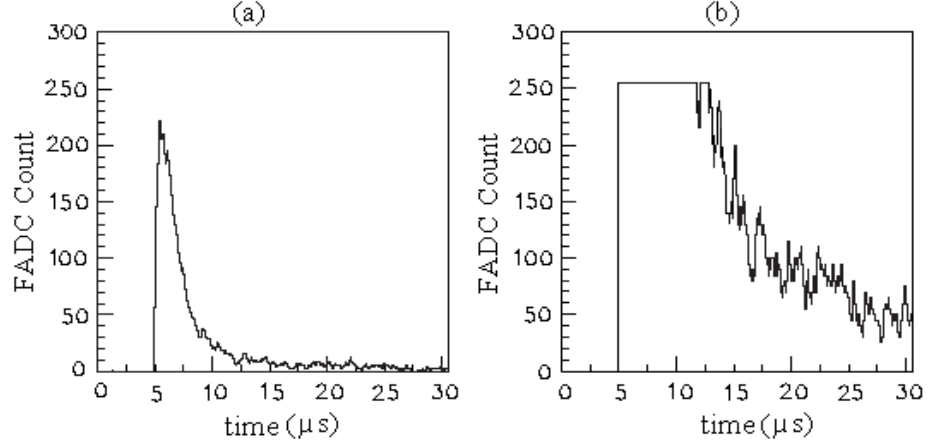


Figure 5.1: Typical (a) unsaturated and (b) saturated pulses recorded by the FADC.

for saturated events were achieved.

Special data was taken to invent techniques and develop software algorithms to reconstruct the missing part of the saturated pulses. A  $5 \times 5 \times 5 \text{ cm}^3$  CsI(Tl) crystal was used and signals were read out by a single PMT and a FADC channel with an identical settings to the KS experiment. The trigger was set at  $t_0 = 100^{\text{th}}$  FADC time-bin, such that the pulse information of  $\delta t_- = 5 \mu\text{s}$  (100 *time-bins*) and  $\delta t_+ = 25.6 \mu\text{s}$  (512 *time-bins*) before and after the trigger were recorded, respectively. Both  $\alpha$  and  $\gamma$  events were taken by activating the CsI(Tl) crystal with  $^{241}\text{Am} - \text{Be}$  and  $^{137}\text{Cs}$  sources, respectively.

The amplitude of the pulse was adjusted by selecting the appropriate PMT high voltage. A large sample of unsaturated events are added together to produce a smooth reference pulse shape of  $\alpha$  and  $\gamma$  shown in Figure 5.2a. From

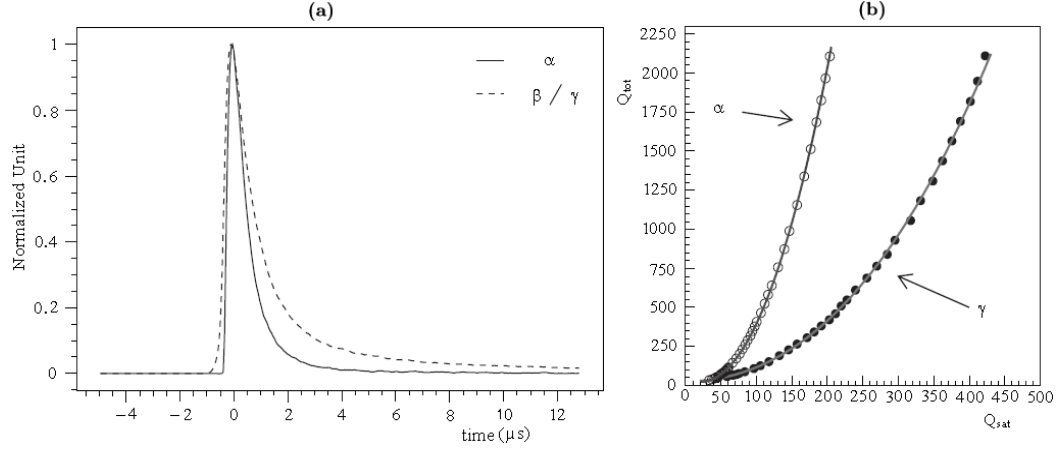


Figure 5.2: (a) Reference pulses of  $\gamma$  and  $\alpha$ , (b) the total charge  $Q_{tot}$  as a function of the saturated charge  $Q_{sat}$ , for both  $\gamma$  and  $\alpha$  events. The data are fitted to a polynomial function for parametrization.

a standard reference pulse shape, a relationship is obtained between “saturated charge ( $Q_{sat}$ )” defined by the integration of the saturated events and the “total charge ( $Q_{tot}$ )” from that of the raw fully recorded pulses. The relationship can be described by a polynomial as

$$Q_{tot} = \sum_{i=0}^3 \alpha_i Q_{sat}^i \quad (5.1)$$

for both the  $\alpha$  and  $\gamma$ -samples as displayed in Figure 5.2b. The coefficients  $\alpha_i$  are obtained from maximum  $\chi^2$ -fits. This function in Equation (5.1) is then used to compensate the missing area in saturated events[77].

One can use this feature to perform consistency checks on data sample where the total charge is known. An unsaturated event is made saturated by software. The algorithm is applied to the simulated saturated event, and the corrected total charge is compared with the raw measurements. For this purpose a test

measurement was done. A level of saturated amplitude  $L_{test} = 100$  was chosen. A new set of  $\alpha_i$  was obtained from a data set of  $\gamma$ -events taken with a  $^{137}\text{Cs}$  source. The PMT high-voltage was adjusted such that the amplitude for the  $662\text{ keV}$  line is below the actual saturation level of 255 but significantly above  $L_{test}$ , the spectrum is displayed in Figure 5.3a. The same data was then made saturated by redefining the saturated amplitude  $L_{test}$ , and the spectra is shown in Figure 5.3b, while that for the reconstruction events after the correction procedures is shown in Figure 5.3c. There is excellent agreement on the  $^{137}\text{Cs}$  peaks in terms of their integrated charge[78], resolution and area between Figure 5.3a and Figure 5.3c.

## 5.1 The Performance of CsI(Tl) Detector

The typical left signal  $Q_L$  versus right signal  $Q_R$  distribution after cosmic ray vetoes and reconstruction of the saturated events by using correction factors for single-site events is depicted in Figure 5.4. The colored dots corresponds to reconstructed saturated events. As seen in this figure unsaturated and saturated events after reconstruction match perfectly. There are evidence of internal radioactivity due to residual  $^{137}\text{Cs}$ , such that the distributions of the  $662\text{ keV}$  events are uniform along the  $40\text{ cm}$  crystal length. Events due to  $\gamma$ -background from  $^{40}\text{K}$  ( $1460\text{ keV}$ ) and  $^{208}\text{Tl}$  ( $2614\text{ keV}$ ), on the other hand, occur more frequently near both edges, indicating that they are from sources external to the

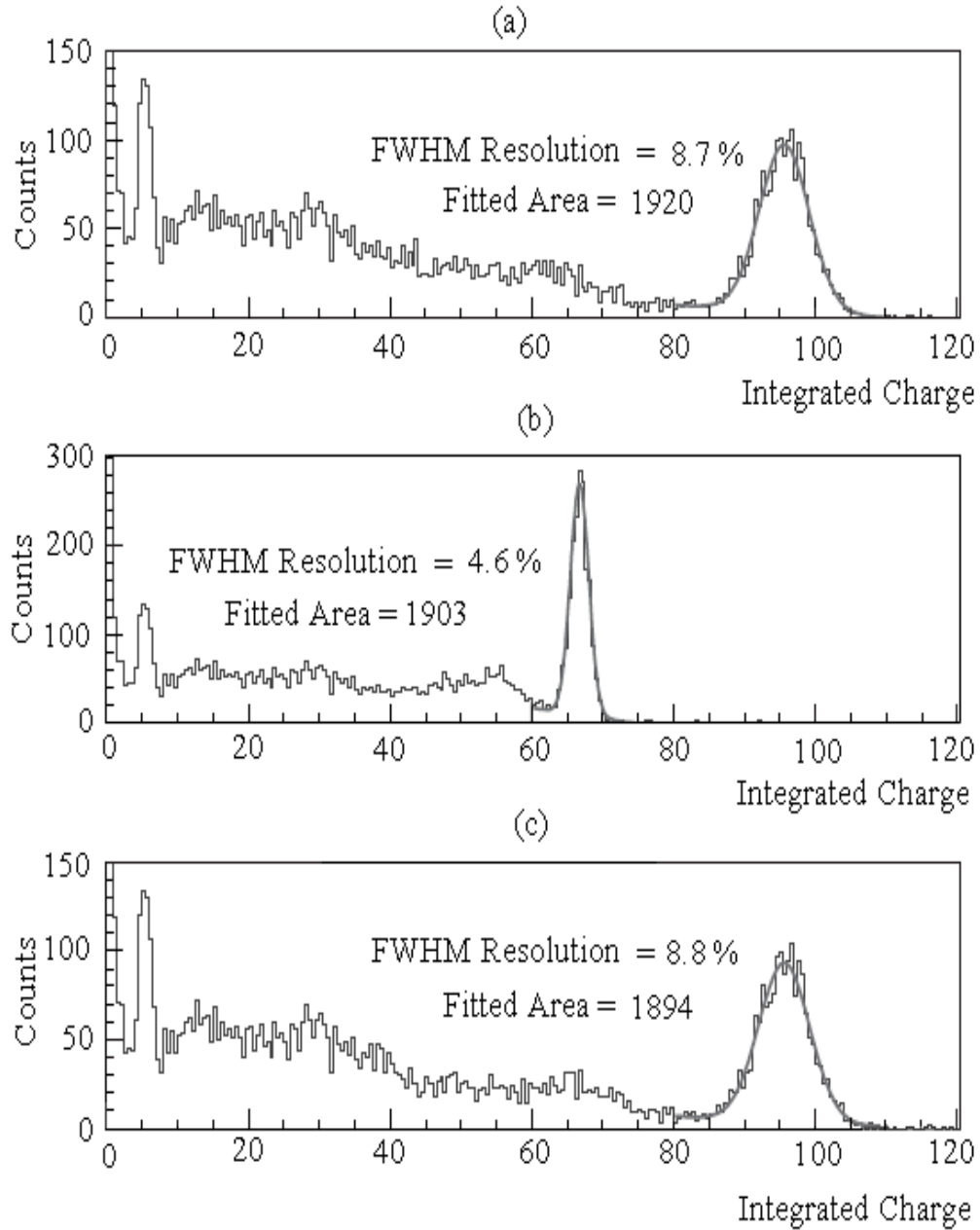


Figure 5.3: Energy spectra for  $^{137}\text{Cs}$ , (a) raw spectra of unsaturated events, (b) spectra of events made saturated by software, and (c) spectra of saturated events after the corrections are applied.

crystals. Low background level above 3  $MeV$  enables us making a measurement of  $\sigma[\bar{\nu}_e - e(SM)]$ .

The sum of the PMT signals gives information about energy, on the other hand, the difference of both side signals gives information about longitudinal Z-position of the events and it is proportional to  $R = (Q_L - Q_R) / (Q_L + Q_R)$ . The variation of collected light for  $Q_L$ ,  $Q_R$  and  $Q_L + Q_R$  as a function of position within one crystal module is shown on Figure 5.5a. The charge unit is normalized to unity at the  $^{137}\text{Cs}$  photo-peak (662  $keV$ ) for both  $Q_L$  and  $Q_R$  at their respective ends, while the error is denote the FWHM width at that energy. The variation of  $R$  along the crystal is displayed in Figure 5.5b, showing the capacity to provide a position measurement. The ratio of the RMS errors in  $R$  relative to the slope gives the longitudinal position resolution[79]. The performance of the prototype modules was published in the reference [78]. The discontinuity at  $L = 20\text{ cm}$  is due to the optical mismatch between the glue ( $n = 1.5$ ) and the CsI(Tl) crystal ( $n = 1.8$ )[55].

Performing a measurement on the crystal prototype modules, the energy and spatial resolutions as a function of energy were obtained, as shown in Figure 5.6, respectively. For energy 10% FWHM energy resolution is achieved at around  $^{137}\text{Cs}$  energy peak (662  $keV$ ); and for the longitudinal position  $\sim 2\text{ cm}$  and 3.5  $cm$  of resolution is obtained at 662 and 200  $keV$ , respectively.

In addition, CsI(Tl) scintillating crystal provides powerful PSD capabilities[80]

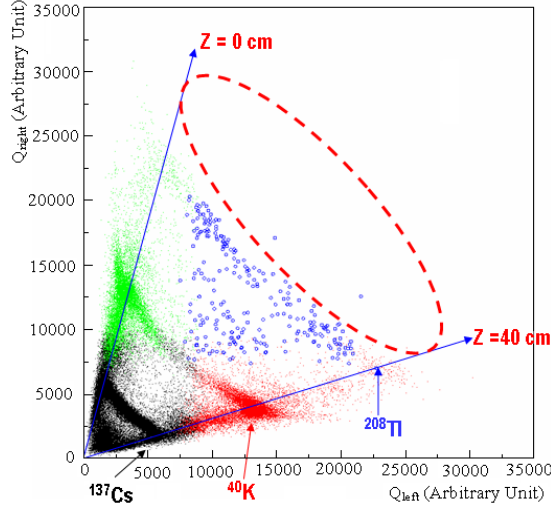


Figure 5.4: Typical  $Q_L$  vs.  $Q_R$  distributions for single site events after applying active cosmic ray vetoes showing the background events of natural sources. Different colour in one band shows one side saturation pulse after correction of energy and circular region is pointed at 3 MeV the region of interest.

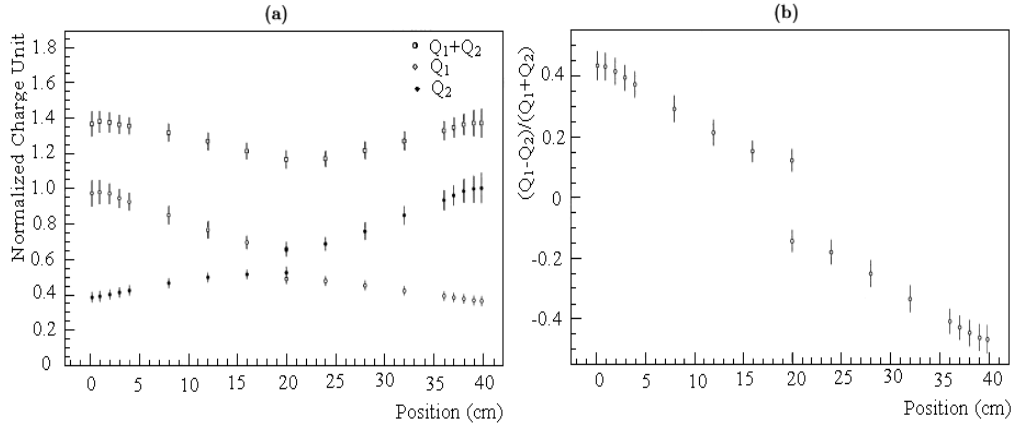


Figure 5.5: The measured variation of (a)  $Q_L$ ,  $Q_R$ , and  $Q_{tot} = Q_L + Q_R$  along the longitudinal position of the crystal module, showing the capability to provide a energy measurement, and (b)  $R = (Q_L - Q_R)/(Q_L + Q_R)$  along the longitudinal position of the crystal module, showing the capability to provide a position measurement.



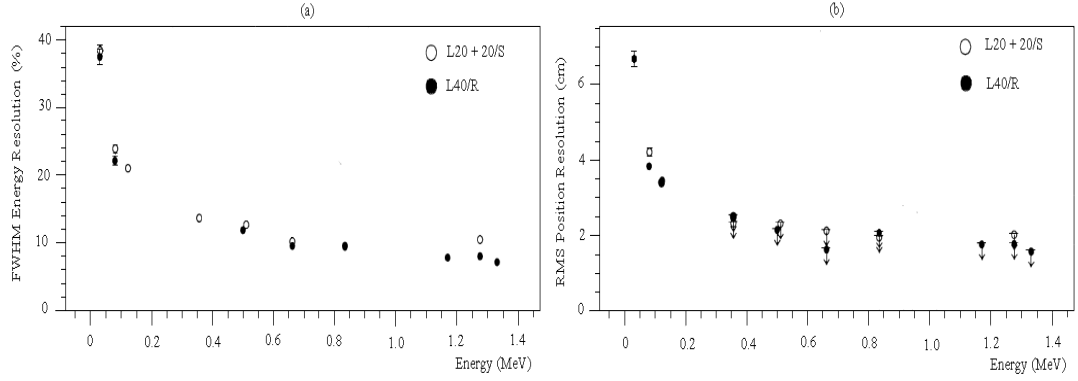


Figure 5.6: The variation of (a) FWHM energy resolution (b) RMS position resolution with respect to energy for the CsI(Tl) crystal modules.

to differentiate  $e/\gamma$  from  $\alpha$  events, with an excellent separation of  $>99\%$  above 500 keV. The pulse shape discrimination techniques and methods in CsI(Tl) scintillating crystals are discussed in reference [81] in detail. In the scintillating CsI(Tl) crystals the light emission behavior of  $\gamma$  and  $\beta$  (that is, minimum ionizing particle) is different than that of heavily ionizing particles like  $\alpha$ -particles and nuclear recoils. Heavily ionizing events due to  $\alpha$ -particles and nuclear recoils have faster decays than those from  $e/\gamma$ 's -this behavior is opposite in liquid scintillators. The light output for  $\alpha$ 's in CsI(Tl) is quenched less than that in liquid scintillators. The comparison of typical scintillating average pulse shapes recorded by the trigger system due to  $\alpha$ , nuclear recoils and  $e/\gamma$  are illustrated in Figure 5.7, where  $t = 0$  is defined by the trigger time. Fitted to an analytic form of the pulse shape ( $y$ ) as a function of time ( $t$ ) for the light profile from  $e/\gamma$  events in Equation (5.2), one obtains the fitted-values of rise time ( $\tau_0$ ) and fall

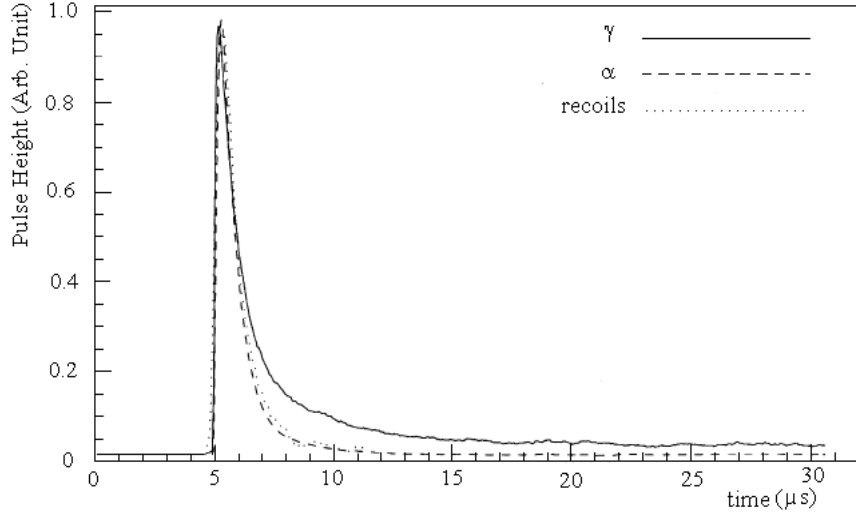


Figure 5.7: The comparison of average pulse shapes due to  $\alpha$  - particles at 5.4 MeV, nuclear recoils at 45 keV and  $\gamma$  - rays at 660 keV.

Table 5.1: Fitted rise and decay time constants as well as the ratio between slow and fast decay components for  $\alpha$  and  $\gamma$  events measured CsI(Tl).

Event type	Rise Time [ $\tau_0$ (ns)]	Decay Time Constants		Ratio (r)
		Fast Comp. [ $\tau_1$ ( $\mu$ s)]	Slow Comp. [ $\tau_2$ ( $\mu$ s)]	
$\alpha$	$203 \pm 3$	$0.54 \pm 0.1$	$2.02 \pm 0.02$	$0.29 \pm 0.02$
$\gamma$	$261 \pm 2$	$0.87 \pm 0.1$	$5.20 \pm 0.04$	$0.61 \pm 0.01$

times ( $\tau_1, \tau_2$ ) as well as the ratio between the fast and slow decay components ( $r$ ) as tabulated[78] in Table 5.1. By the help of characterization of these pulse shapes, one can effectively separate  $\alpha$  events from  $e/\gamma$  one.

$$y = cons \times \left[ 1 - e^{(-\frac{t}{\tau_0})} \right] \times \left[ \frac{1}{\tau_1} e^{(-\frac{t}{\tau_1})} + \frac{r}{\tau_2} e^{(-\frac{t}{\tau_2})} \right] \quad (5.2)$$

One of the effective methods for separation of the  $\gamma$  pulses from the  $\alpha$  one is the “double charge method”[82]. In this method, the comparison of the “total

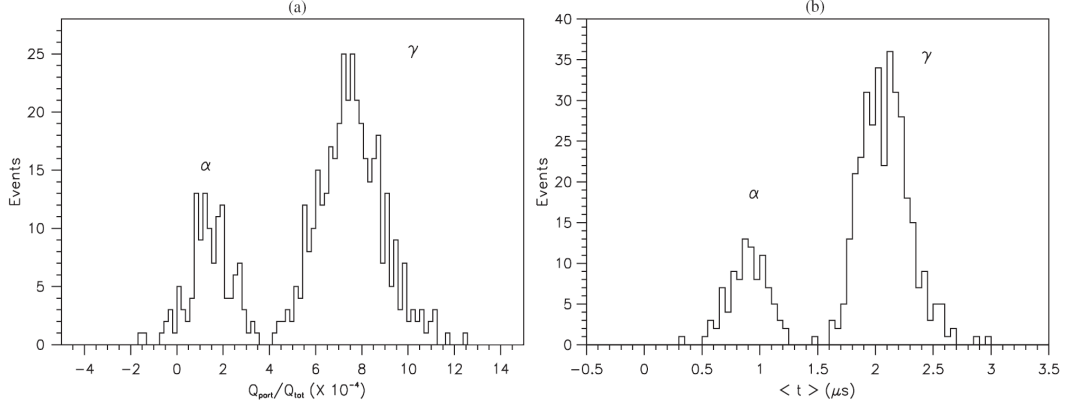


Figure 5.8: Event identification with PSD via (a) the partial charge versus total charge method, and (b) the mean time method. The  $\gamma$  samples from  $^{40}\text{K}$ , while the  $\alpha$  events are with electron equivalence energy of more than 1 MeV. A perfect identification can thus be achieved.

charge ( $Q_{tot}$ )” and “partial charge ( $Q_{par}$ )” are performed.  $Q_{tot}$  and  $Q_{par}$  are defined by integrating the entire pulse from  $-0.75$  to  $12.8 \mu s$ , and the tail from  $5$  to  $12.8 \mu s$ , respectively. The other effective method for the separation of  $\alpha$  events from  $e/\gamma$  one is the “*mean time method*”. The mean time can be defined as;

$$\langle t \rangle = \frac{\sum (A_i t_i)}{\sum A_i} \quad (5.3)$$

where  $A_i$  is the FADC-amplitude at the time bin  $t_i$ . The PSD performance for both methods in  $MeV$  range are shown in Figure 5.8, indicating excellent separation between  $\alpha$  and  $e/\gamma$  events[83].

The suppression, control and understanding of the background play a very

important role in low energy low background experiments. The CsI(Tl) scintillator crystal features like high  $\gamma$ -rays capture efficiency and good energy resolution together with PSD capabilities for  $\alpha$ -particles and the detector design as well, can provide important diagnostic tools for understanding the physical process and the background of the system. Once the background channels are identified and understood, measurement and subtraction of their associated effects can be performed. For instance, by measuring of the  $\gamma$ -peaks due to  $^{40}\text{K}$ ,  $^{60}\text{Co}$ , and  $^{137}\text{Cs}$  their associated  $\beta$  background can be accurately accounted for and subtract off[79]. For further discussion on intrinsic and environmental background understanding and suppression methods will be given in Chapter 6 in detail.

## 5.2 Calibration Methods

As we discussed in the Section 5.1 the light output are read out at the both ends ( $Q_L$  and  $Q_R$ ) by PMTs and the sum of the PMT signals gives information about energy and the difference of both side signals gives information about longitudinal Z-position of the events. Based on these definitions, the calibration procedures can be summarized in three steps:

Step1 : Getting Z-position Calibration Parameters by using high-energetic cosmic rays as a reference. Longitudinal Z-position can be defined as

$$Z = \frac{f_i Q_R - Q_L}{f_i Q_R + Q_L} \quad (5.4)$$

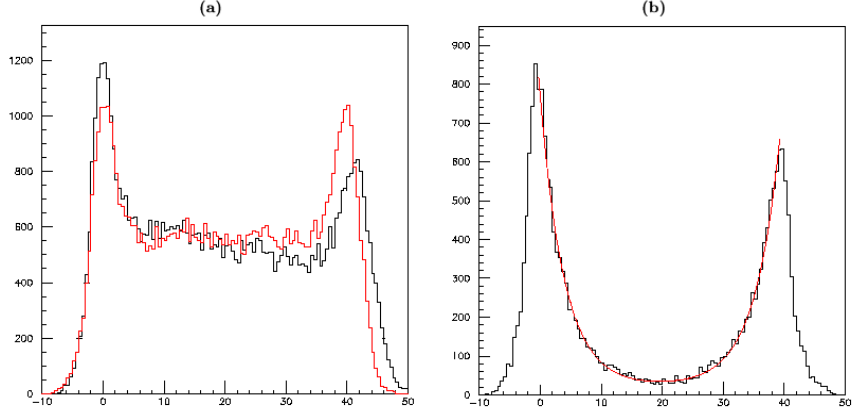


Figure 5.9: The longitudinal Z position distribution of (a)  $^{137}\text{Cs}$  events, red distribution corresponds to after adopting  $F_i$  free parameter making Z-position distribution of  $^{137}\text{Cs}$  events, shown in black, flat in the middle portion of the crystal, (b)  $^{40}\text{K}$  events showing symmetric attenuation for both sides.

where  $f_i$  is the free physical parameter to make  $^{137}\text{Cs}$  Z-distribution uniform in the middle portion of the crystal after few  $\text{cm}$  of veto cut since  $^{137}\text{Cs}$  source is internal to the crystal and  $^{40}\text{K}$  peak attenuation symmetric at the both ends, as well. The longitudinal position distribution of  $^{137}\text{Cs}$  and  $^{40}\text{K}$  peaks after adopting the definition of Equation (5.4) is illustrated in Figure 5.9.

The longitudinal position calibration method is that as shown in Figure 5.10 both side peak means of high-energetic cosmic rays distribution are initially taken as 0 and 40  $\text{cm}$ , respectively and redefine all events Z position accordingly by accepting new Z distribution as  $Z_{cal} = a_z + Z_{noncal} \times b_z$

- Step2 : Getting Light Attenuation Parameter,  $\alpha$ , which depends on the uniformity of the crystal, from non-calibrated energy definition of  $\sqrt{Q_L \times Q_R}$  vs. Z-position distribution, as shown in Figure 5.11.

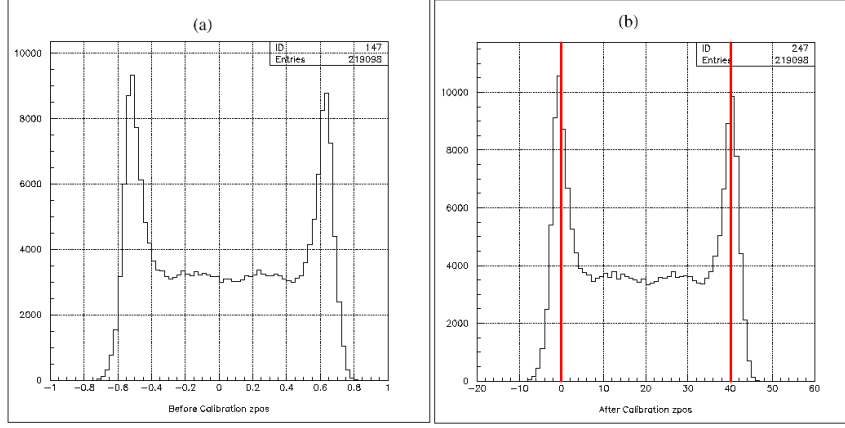


Figure 5.10: Longitudinal position calibration method (a) before calibration the scale is arbitrary and (b) after calibration by taking both side peak means initially 0 and 40 *cm* .

By using light attenuation parameter, the slope in non-calibrated energy vs. Z-position distribution can be tuned. This makes an improvement on the energy resolution significantly.

- Step3 : Getting Energy Calibration Parameters from the definition of Equation (5.5):

The calibrated energy can be defined as

$$E = a + \sqrt{Q_L \times Q_R} \times e^{-\alpha Z} \times b \quad (5.5)$$

where  $a$  and  $b$  are the energy calibration parameters,  $\alpha$  is the light attenuation parameter of the events obtained from Step2 and  $Z$  is the longitudinal position of the events obtained from Step1.

Energy calibration parameters  $a$  and  $b$  can be found by using known energy

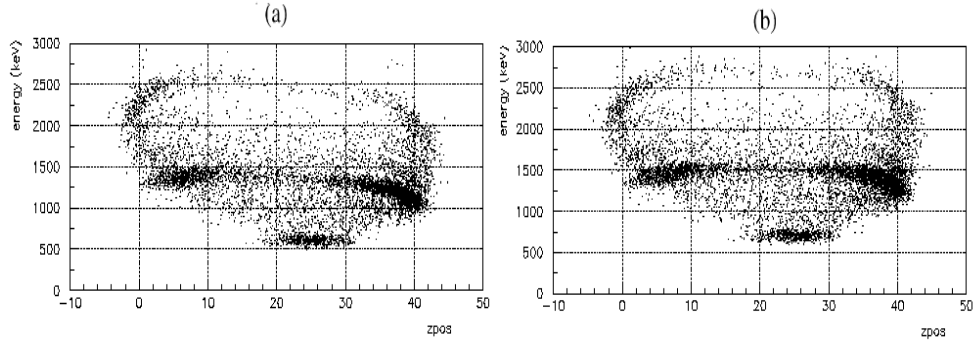


Figure 5.11: The distribution of not calibrated energy vs. z-position for one crystal as an example (a) before and (b) after correction of slope in the distribution which provides getting light attenuation parameter for each crystal.

peaks of natural occurring radioactive isotopes of  $^{137}\text{Cs}$  at  $661.7 \text{ keV}$ ,  $^{40}\text{K}$  at  $1460.8 \text{ keV}$  and  $^{208}\text{Tl}$  at  $2614.53 \text{ keV}$ , as seen in Figure 5.12a. By matching peaks energies of the data with that of natural radioactive isotopes, the energy calibration can be performed using the linearity as shown in Figure 5.12b.

### 5.3 Event Selection and Defining Basic Cuts

Scatterings of  $\bar{\nu}_e - e^-$  inside the CsI(Tl) scintillating crystal target would give a Single-Hit (SH) events. Therefore,  $\bar{\nu}_e - e^-$  lone events were selected from raw data through selection criteria via Anti-Compton Veto (ACV), Cosmic-Ray Veto (CRV) and Pulse Shape Discrimination (PSD). Finally a  $4 \text{ cm}$  Z-position cut is applied to suppress background events due to external background. The background due to non genuine, accidental or unwanted correlated and convoluted events were suppressed by PSD. The ACV and CRV cuts suppressed Compton

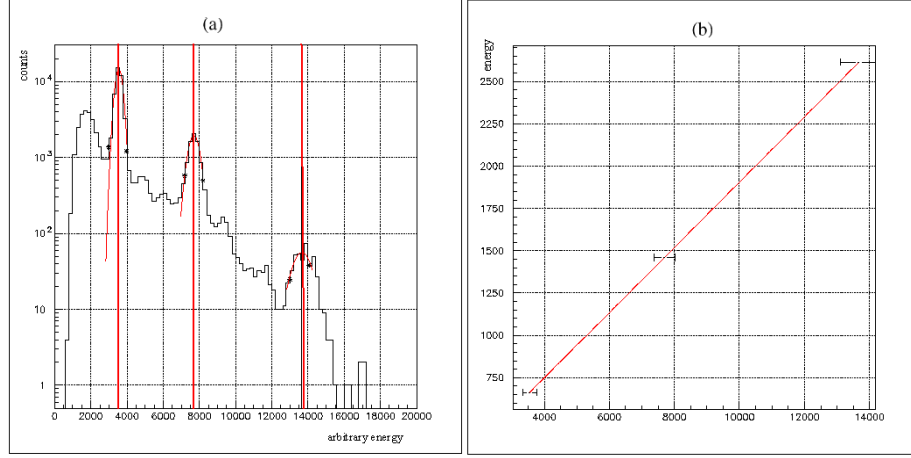


Figure 5.12: Energy calibration method (a) showing the peaks are taken as  $^{137}\text{Cs}$  (662 keV),  $^{40}\text{K}$  (1440 keV) and  $^{208}\text{Tl}$  (2614 keV), respectively (b) linearity and peak position check for choosen energy peak with respect to  $^{137}\text{Cs}$  (662 keV),  $^{40}\text{K}$  (1440 keV) and  $^{208}\text{Tl}$  (2614 keV) actual energies.

Scattering and Cosmic-Ray induced events, respectively. The selection criteria for the genuine events is the following;

### 5.3.1 Single Hit Cut

Since neutrinos interact with matter rarely, the mimic signature of the signal must be Single-Hit. SH is considered as only one uncorrelated interaction happens in the crystal at one time and also only one crystal must be fired at one time, there must be no other fired crystal at the same time. We select only events that both sides of the fired crystal excess the noise level and give a positive charge. In other words, SH is meaning that within total recording time of 500  $\mu\text{s}$  there must be only one uncorrelated interaction. During recording of



the relevant events a 500  $\mu s$  strobe is opened and the events are digitizing after the initial trigger as long as 256 time-bins and wait for another possible events. The timing sequence was described in the Section 4.1 and illustrated in Figure 4.8. If any other interaction happen in the same crystal after 256 time-bins the number of hit (nhit) increase one unit. If any other interaction happen in the other crystal during the 500  $\mu s$  recording time the number of crystal hit (ncrystal) increase one unit. If any other interaction happen in the same crystal within 256 time-bins, the PSD will cut away this kind of double pulse events.

### 5.3.2 Cosmic Ray Veto Cut

The separation of non-cosmic events from cosmic ones is very crucial since cosmic rays can have mimic signature of genuine events in the region of interest. In this sense, the efficiency of tagging cosmic ray plays very important role to reduce background. The veto time is defined as the time gap between the last hit in veto and the trigger. If there is no correlation between events, the veto time is defined as a Poisson distribution given in Equation (5.6). For the limit of  $n \rightarrow 0$  the time decrease exponentially. The cosmic ray veto time can be selected from the kink point of vetotime distribution as shown in Figure 5.13.

$$P_t(n) = \frac{t^n e^{-t}}{n!} \quad (5.6)$$

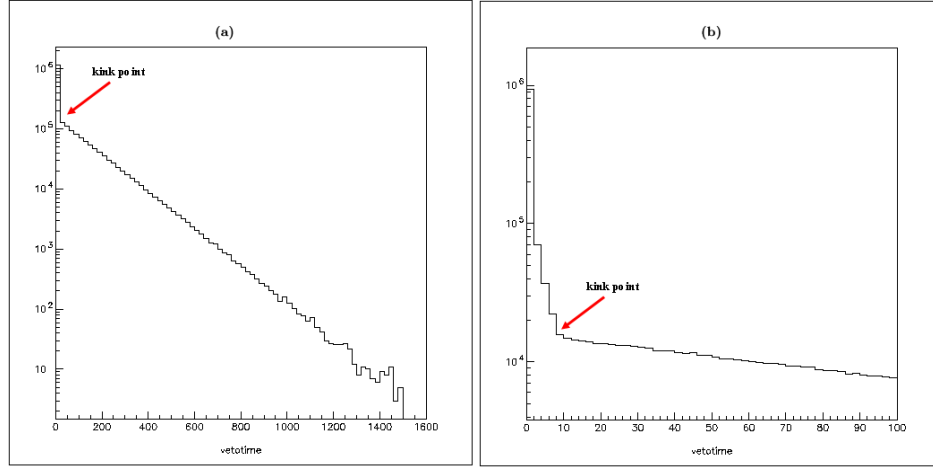


Figure 5.13: The veto time distribution of the events showing the kink point in  $8 \mu s$  due to cosmic ray events.

### 5.3.3 Pulse Shape Discrimination (PSD) Cut

PSD Cut is based on the correlation between partial charge and amplitude for unsaturated events for both left and right side as shown in Figure 5.14a, and correlation between partial charge and saturation length for saturated events for both left and right side as shown in Figure 5.14b. In the figure red plus dots represent all data after basic cuts, green star dots represent  $Tl - 208$   $2614 \text{ keV}$  energy range events and circle blue dots represent above  $3 \text{ MeV}$  events. It can be seen in the graphs these selection criteria provide very powerful separation between gamma and alpha or narrow pulse events. Non genuine accidental or unwanted events such as double pulse events or combination of  $\beta - \gamma$  or  $\beta - \alpha$  kind events can be cut away by the PSD technique. Some example of these kind of events cut by PSD are depicted in Figure 5.15.

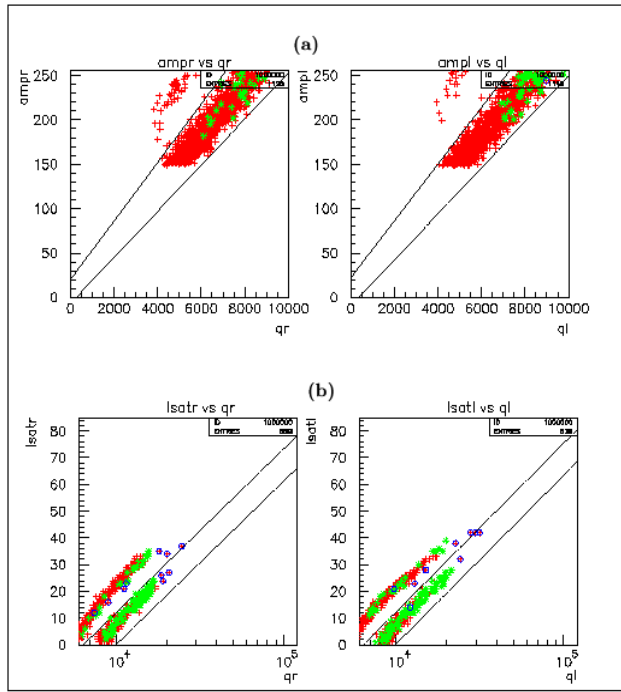


Figure 5.14: PSD selection criteria for (a) unsaturated events and (b) for saturated events. Red plus dots represent all data after basic cuts of CRV, ACV. Green star dots represent Tl-208 2614 keV energy range events and circle blue dots represent above 3 MeV events.

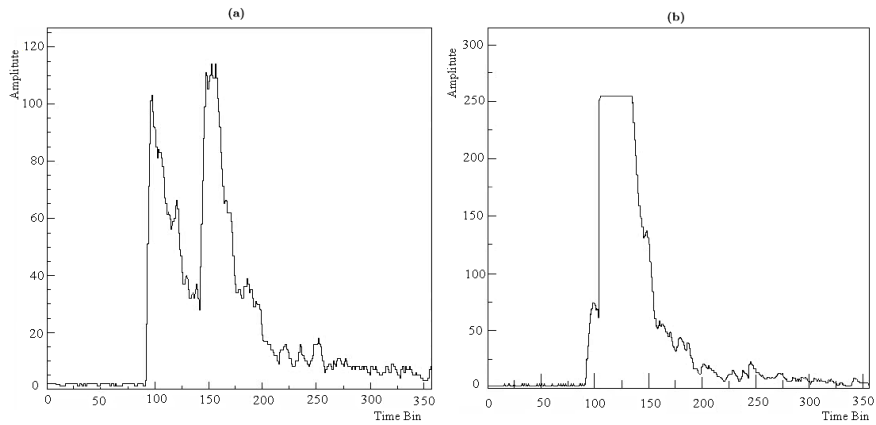


Figure 5.15: A sample of (a) double pulse events (b)  $\beta - \gamma$  kind events which are cut by PSD.

#### 5.3.4 Z-position Cut

Since CsI(Tl) scintillating crystal provides strong attenuation for  $\gamma$ 's, few *cm* active veto cut is enough to get rid of events due to external background. For this purpose from both ends 4 *cm* Z-cut was applied in our analysis.

#### 5.3.5 The Cut Efficiency and Suppression Factors

For the efficiency calculations the random trigger was used since there is no correlation between random trigger and event trigger time. A random trigger events are generated every 10 seconds and it must survive after applying cuts. Therefore, random trigger is an useful tool for calculating the cut efficiencies. Efficiency factors can be calculated by taking ratio of number of counts after and before the cuts. The 4 *cm* z-cut at both sides over all 40 *cm* crystal length corresponds to  $32/40 = 80\%$  efficiency. Stability of efficiency factor was studied for Period-II and Period-III and the fit to the constant value was taken as an efficiency factor of that cut. From the stability of the efficiency factors we can estimate our systematic error due to each cut, as well. The stabilities of each cut for Period-II and Period-III are shown in Figure 5.16 and Figure 5.17, respectively. In the figures each point represent one data set efficiency factor. It can be seen from the stability figures that all the cut efficiencies are very stable.

The energy spectra of Reactor *OFF* data after applying CRV, ACV, PSD and Z-position cuts for Period-II and Period-III are illustrated in Figure 5.18a

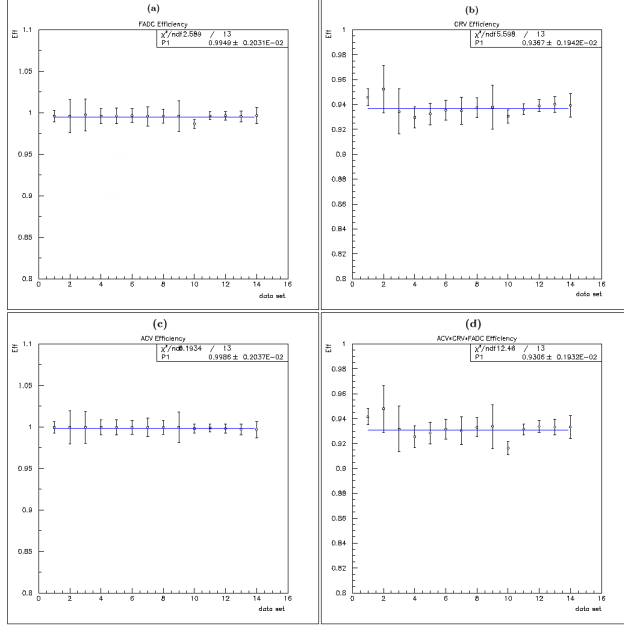


Figure 5.16: For Period-II the stability of efficiency factors of (a) FADC (b) CRV (c) ACV and (d) total which is product of each efficiency factor.

and Figure 5.18b, respectively. Suppression factors was calculated based on taking ratio of number of events before cut and that of surviving events after cut. The background suppressions in Reactor *OFF* in  $cpd$  ( $kg^{-1} \times day^{-1}$ ) unit and the efficiencies of each cut in  $3 - 8$  MeV energy region are listed in Table 5.2. In order to study data stability we chose  $Tl - 208$  2614 keV peak event rates. As illustrated in Figure 5.19a and Figure 5.19b the data is rather stable for Period-II and Period-III data taking time, respectively.

For the possible sources for systematic error we studied on cut efficiencies, data stability and time measurement. The DAQ live times were accurately measured to  $< 5 \times 10^{-4}$  through the ratios of generated to recorded random

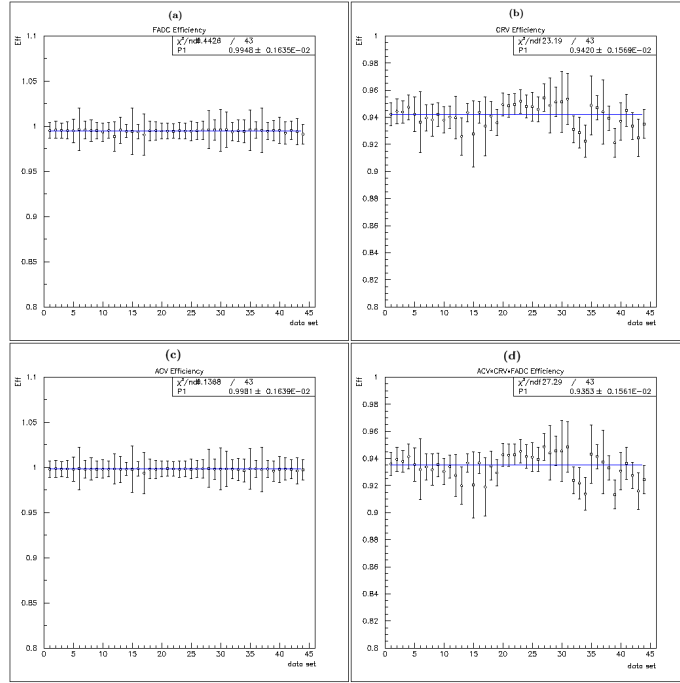


Figure 5.17: For Period-III the stability of efficiency factors of (a) FADC (b) CRV (c) ACV and (d) total which is product of each efficiency factor.

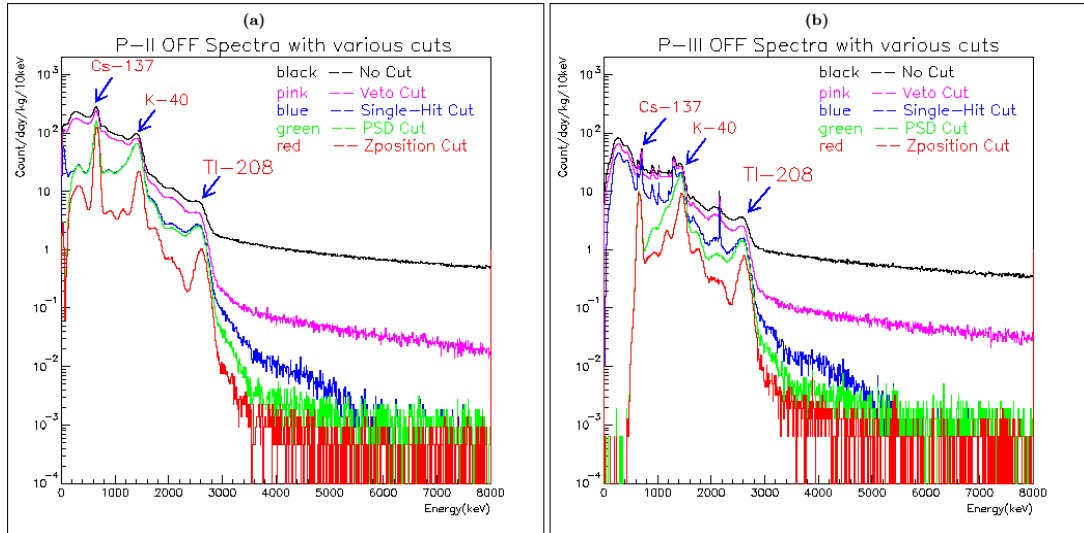


Figure 5.18: The spectral response to the various cuts in (a) Period-II and (b) Period-III data taking time, showing the effects of each cut on the spectrum.

Table 5.2: Summary of the background suppression and efficiency factors of various cuts.

Event Selection	Efficiency		Suppression ( $3 - 8 \text{ MeV}$ ) $cpd (kg^{-1} \times day^{-1})$	
	II	III	II	III
Raw Data	1.0	1.0		
Live Time	88.78%	93.53%	1.0	1.0
FADC>3	> 99%	> 99%	350.493	245.935
CRV	93.67%	94.20%	23.027(6.57%)	28.824(11.72%)
Single Hit	99.86%	99.81%	3.682(15.99%)	3.103(10.76%)
PSD	$\sim 100\%$	$\sim 100\%$	1.235(33.54%)	1.112(35.83%)
Z-position	80%	80%	0.447(36.19%)	0.508(45.71%)
Combined	74.83%	75.22%	0.1076%	0.207%

trigger events[56]. The stabilities were obtained shown in Figure 5.16 and 5.17 as 0.208% ( $0.9306 \pm 0.0019$ ) and 0.167% ( $0.9353 \pm 0.0016$ ) for Period-II and Period-III, respectively. The data stabilities were obtained from Tl-208 energy peak shown in Figure 5.19 as 0.87% ( $2.002 \pm 0.0173$ ) and 0.80% ( $1.498 \pm 0.0123$ ) for Period-II and Period-III, respectively. The various sources of systematic uncertainties and their stability are listed in Table 5.3.

After suppression of cosmic-induced background, anti-Compton vetoes, convoluted and accidental events by Pulse Shape Discrimination (PSD), and external background by Z-position cut, in  $3 - 8 \text{ MeV}$  a background level of  $0.4470 \pm 0.0141 \text{ kg}^{-1} \text{ day}^{-1}$  and  $0.5082 \pm 0.0179 \text{ kg}^{-1} \text{ day}^{-1}$  were achieved for Period-II and Period-III, respectively. The spectra for Single-Hit events after applying all cuts based on  $2244.01 \text{ kg} \times \text{days}$  Reactor *OFF* data taking in Period-II and  $1581.56 \text{ kg} \times \text{days}$  in Reactor *OFF* data taking in Period-III are illustrated in Figure 5.20a and Figure 5.20b, respectively.

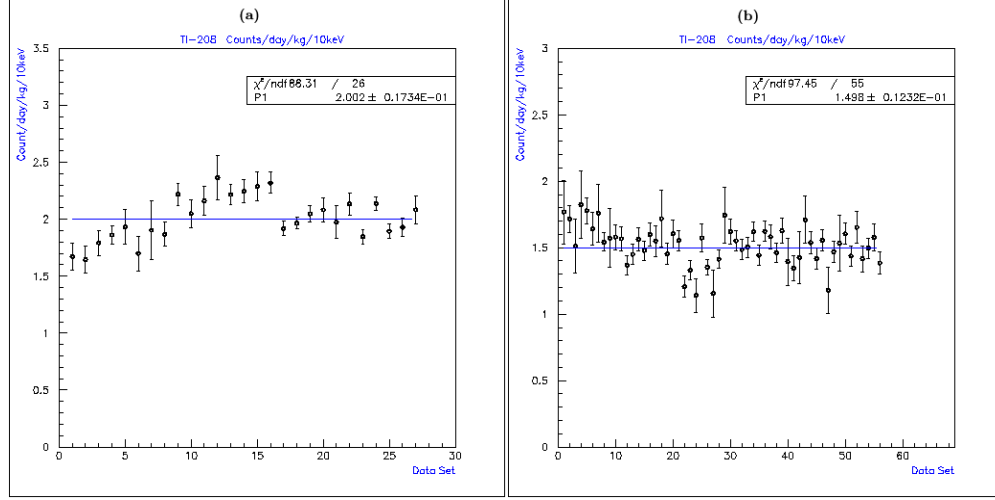


Figure 5.19: Data stability of (a) Period-II and (b) Period-III data taking time of  $Tl - 208$  2.614 MeV peak events, showing that during the period data is rather stable.

Table 5.3: The various sources of the systematic uncertainties and their stability level.

Period	II	III
Sources	Stability	
Neutrino Spectrum	$\sim 5\%$	
DAQ Life Time	$< 10^{-4}$	
FADC only	0.204%	0.164%
CRV only	0.207%	0.167%
ACV only	0.204%	0.164%
Combined Cut	0.208%	0.167%
Data Stability	0.87%	0.80%



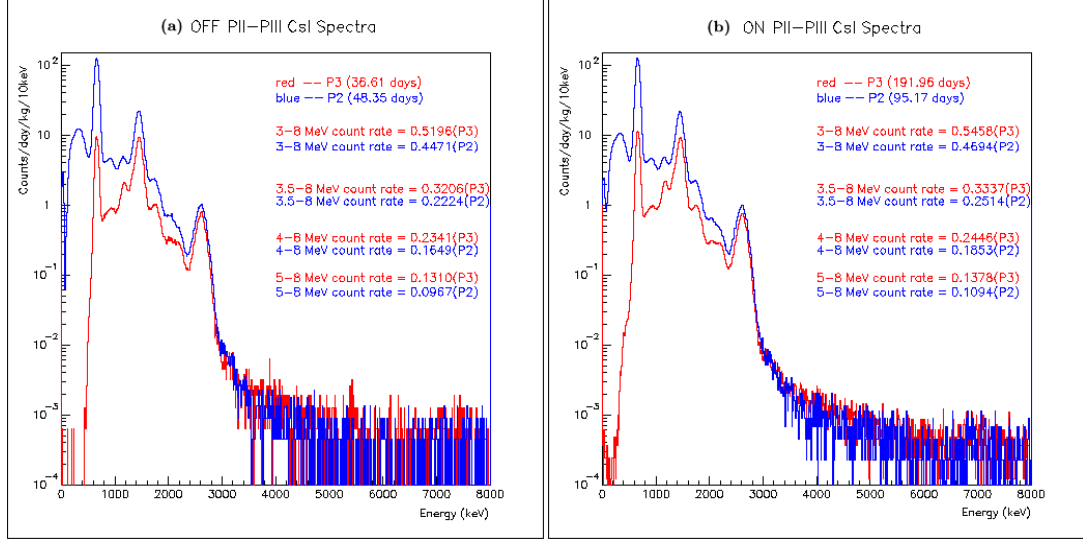


Figure 5.20: The comparison of Single-Hit spectra of P-II and P-III data taking for (a) Reactor OFF and (b) Reactor ON, after applying all cuts, showing the background level of both periods.

After getting Reactor *ON* and *OFF* event rate, one can perform *ON* – *OFF* subtraction to get neutrino signal by accepting background is Reactor *OFF*. In Table 5.4 and Table 5.5 Reactor *ON*, *OFF* and the *ON* – *OFF* residue event rates are listed for Period-II and Period-III, respectively. After performing all the cuts still we have quite high background level. Since we have limited Reactor *OFF* data taking time the statistical errors are also quite big. In this sense understanding the nature of the background is very critical. Only in this way we can suppress the background more in order to achieve a reasonable level of statistical error in the measurement. In the next chapter we will discuss about the origin of the background and suppression methods, thereby making some estimation on background.

Table 5.4: The event rate ON, OFF and The Residue ON-OFF in  $cpd \times kg^{-1} \times 10keV^{-1}$  unit for P-II Period .

<i>Energy</i> ( <i>MeV</i> )	<i>ON</i> $\times 10^{-2}$	<i>OFF</i> $\times 10^{-2}$	<i>ON - OFF</i> $\times 10^{-2}$
3.0 – 3.5	$21.808 \pm 0.703$	$22.465 \pm 1.001$	$-0.658 \pm 1.223$
3.5 – 4.0	$6.612 \pm 0.387$	$5.750 \pm 0.506$	$0.862 \pm 0.637$
4.0 – 4.5	$4.393 \pm 0.315$	$4.101 \pm 0.428$	$0.292 \pm 0.531$
4.5 – 5.0	$3.193 \pm 0.269$	$2.719 \pm 0.348$	$0.474 \pm 0.440$
5.0 – 5.5	$2.672 \pm 0.246$	$1.917 \pm 0.292$	$0.755 \pm 0.382$
5.5 – 6.0	$1.834 \pm 0.204$	$1.426 \pm 0.252$	$0.408 \pm 0.324$
6.0 – 6.5	$1.246 \pm 0.168$	$1.159 \pm 0.227$	$0.866 \pm 0.283$
6.5 – 7.0	$1.812 \pm 0.203$	$1.560 \pm 0.264$	$0.252 \pm 0.333$
7.0 – 7.5	$1.721 \pm 0.197$	$1.828 \pm 0.285$	$-0.106 \pm 0.347$
7.5 – 8.0	$1.653 \pm 0.193$	$1.783 \pm 0.282$	$-0.130 \pm 0.342$

Table 5.5: The event rate ON, OFF and the Residue ON-OFF in  $cpd \times kg^{-1} \times 10keV^{-1}$  unit for P-III Period .

<i>Energy</i> ( <i>MeV</i> )	<i>ON</i> $\times 10^{-2}$	<i>OFF</i> $\times 10^{-2}$	<i>ON - OFF</i> $\times 10^{-2}$
3.0 – 3.5	$20.637 \pm 0.501$	$19.653 \pm 1.118$	$0.984 \pm 1.225$
3.5 – 4.0	$8.558 \pm 0.322$	$8.459 \pm 0.733$	$0.099 \pm 0.801$
4.0 – 4.5	$6.094 \pm 0.272$	$6.042 \pm 0.620$	$0.052 \pm 0.677$
4.5 – 5.0	$4.140 \pm 0.224$	$4.134 \pm 0.513$	$0.005 \pm 0.560$
5.0 – 5.5	$3.096 \pm 0.194$	$3.180 \pm 0.450$	$-0.085 \pm 0.490$
5.5 – 6.0	$2.391 \pm 0.170$	$1.781 \pm 0.337$	$0.611 \pm 0.377$
6.0 – 6.5	$2.076 \pm 0.159$	$1.336 \pm 0.291$	$0.740 \pm 0.332$
6.5 – 7.0	$2.355 \pm 0.169$	$1.972 \pm 0.354$	$0.383 \pm 0.392$
7.0 – 7.5	$1.894 \pm 0.152$	$2.544 \pm 0.402$	$-0.650 \pm 0.430$
7.5 – 8.0	$1.663 \pm 0.142$	$1.717 \pm 0.330$	$-0.054 \pm 0.360$

## CHAPTER 6

### BACKGROUND UNDERSTANDING AND SUPPRESSION METHODS

In general, we can say there are two different kind of background, i.e. internal and external. The internal background can be due to contaminations of naturally occurring isotopes mainly  $^{137}\text{Cs}$  and some radioactive decay series of Thorium and Uranium, long-lived fission products and cosmic-induced unstable nuclei. The external background is originated mainly cosmic ray muons, products of cosmic ray muons, spallation neutrons, reactor related radioactive materials like  $^{60}\text{Co}$ , present as dust in the environment and some natural radioactive isotopes which are the contaminations occurring nearly in all materials, like  $^{40}\text{K}$ , and  $^{208}\text{Tl}$ . The background due to external  $\gamma$ 's such as those from the readout device, electronic components, construction materials, or radon contamination on the outer surfaces can thus be attenuated and vetoed by the outer active volume. If the background is originated externally from cosmic-ray induced neutrons, which have little attenuation with high Z-nuclei, their effects can be

minimized by a cosmic veto. When the dominant background contributions are from internal contaminants, two complementary strategies can be deployed for the background control: (i) consistent background subtraction, using the measured spurious  $\alpha$  or  $\gamma$  peaks which indicates residual radioactivity inside the crystal and (ii) the conventional Reactor *ON* – *OFF* subtraction. The background count rate will be stable and unaffected by external parameters such as ambient radon concentrations and details of surrounding equipment configurations. Most background from internal radioactivity come as  $\beta + \gamma$ 's in coincidence, like decays of  $^{214}\text{Bi}$  and  $^{208}\text{Tl}$  from the  $^{238}\text{U}$  and  $^{232}\text{Th}$ , respectively. Hence, they will produce multiple hits with high probability. Therefore, they can easily be eliminated from the data to obtain final energy spectrum since the interesting signals are single-site events. Similarly neutron capture events by the target isotopes manifest as  $(n, \gamma)$  interactions, giving rise to a burst of multiple hits with known total energy. The neutron capture rate can therefore be measured, such that the background due to subsequent decays of the unstable daughter nuclei can be subtracted off[79].

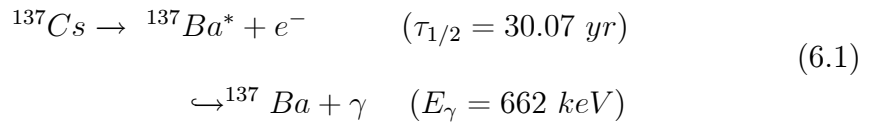
The pulse shape discrimination capability of the CsI(Tl) scintillating crystal gives us a opportunity to measure the intrinsic radiopurity of  $^{137}\text{Cs}$  as well as  $^{235}\text{U}$ ,  $^{238}\text{U}$  and  $^{232}\text{Th}$  decay series. To understand the contribution of radioactive contaminants to the background, the motivation is monitoring of timing and position information for  $\beta - \alpha$  or  $\alpha - \alpha$  events. The main purpose is to estimate

the abundance of intrinsic contamination of  $^{137}\text{Cs}$ ,  $^{235}\text{U}$ ,  $^{238}\text{U}$  and  $^{232}\text{Th}$  and derive the contribution of this contamination to the background. The contamination levels of CsI(Tl) scintillating crystals were measured in data taken with CsI(Tl) scintillating crystal detector at Kuo-Sheng Reactor Neutrino Laboratory by using the correlated events from  $\beta - \alpha$  and  $\alpha - \alpha$  decay sequences.

### 6.1 Study of the Intrinsic Radiopurity in the CsI(Tl) crystal[83]

For the measurement of intrinsic radiopurity one can derived the contamination level of  $^{137}\text{Cs}$  as well as  $^{235}\text{U}$ ,  $^{238}\text{U}$  and  $^{232}\text{Th}$  decay series since the intrinsic radiopurity measurement play a very important role in low energy low background neutrino as well as Dark matter experiments.

The isotope  $^{137}\text{Cs}$  is produced artificially as fission waste from power reactors and atomic weapon tests. Once produced, there is no chemical way to separate  $^{137}\text{Cs}$  from the stable  $^{133}\text{Cs}$ . This is the dominant background in the Dark Matter experiments which use the CsI(Tl) crystal as a target.  $^{137}\text{Cs}$  decays via



with the emission of a  $\gamma$ -ray of energy 662 keV.

A total of 31.3 kg \* day data taken with CsI(Tl) scintillating crystal at Kuo-Sheng Reactor neutrino Laboratory was analyzed. The spectrum is displayed in Figure 6.1a with a distinct line at this energy with a RMS resolution of 5.1%.

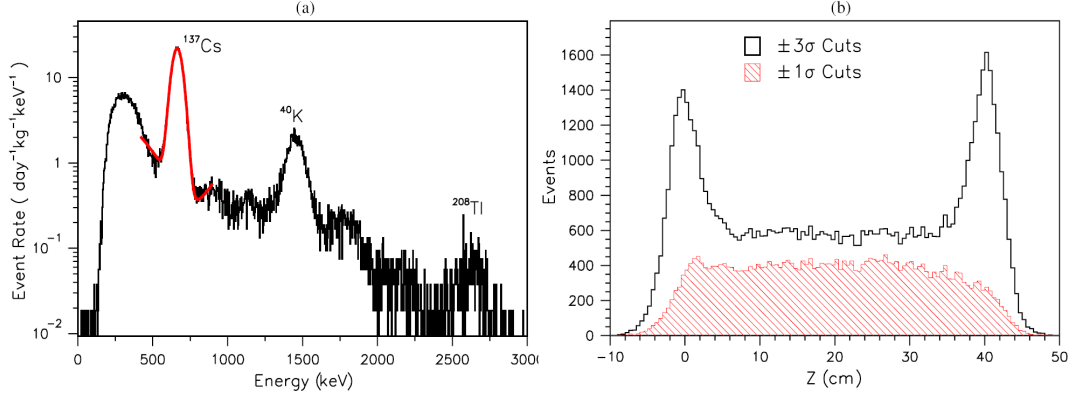


Figure 6.1: (a) Energy spectrum of entire range showing  $^{137}\text{Cs}$ ,  $^{40}\text{K}$  and  $^{208}\text{Tl}$   $\gamma$ -energy peaks (b) Z-position distribution of the  $^{137}\text{Cs}$  events of 31.3  $\text{kg} - \text{day}$  of data.

Other natural background  $\gamma$ -peaks from  $^{40}\text{K}$  at 1460  $\text{keV}$  and  $^{208}\text{Tl}$  at 2614  $\text{keV}$  also appear. The Z-distribution of  $^{137}\text{Cs}$  events after  $\pm 3\sigma$  and  $\pm 1\sigma$  cuts are shown in Figure 6.1b. The uniform Z-distribution after  $\pm 1\sigma$  cut indicates that the source of  $^{137}\text{Cs}$  is internal to the crystal. Accordingly, an average activity of  $61 \pm 2 \text{ mBq kg}^{-1}$ , or equivalently contamination level of  $(1.55 \pm 0.05) \times 10^{-17} \text{ g/g}$  was derived for the CsI(Tl) crystals. Alternatively, the radiopurity of the CsI(Tl) powder have been measured with HPGe detector consistently as  $(1.7 \pm 0.3) \times 10^{-17} \text{ g/g}$ .

All materials contain  $^{235}\text{U}$ ,  $^{238}\text{U}$  and  $^{232}\text{Th}$  radioactive elements in their nature. A sensitive measurement of the spatially and temporally correlated events related to these radioactive elements in CsI(Tl) crystals was performed. A total of 40 CsI(Tl) crystals with a data size of 1725  $\text{kg} * \text{day}$  data taken at KS neutrino laboratory was studied. The event configuration and selection criteria based on

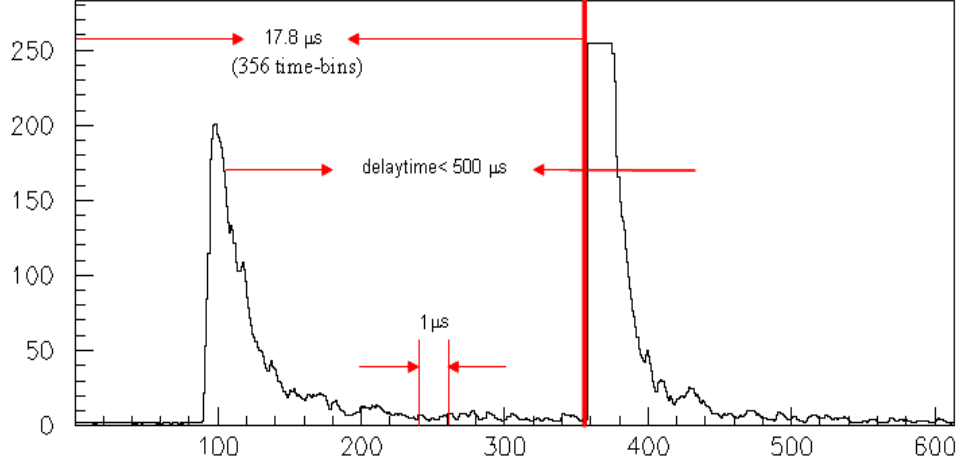
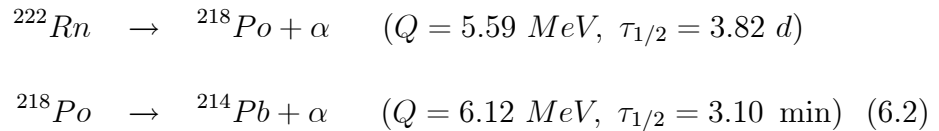


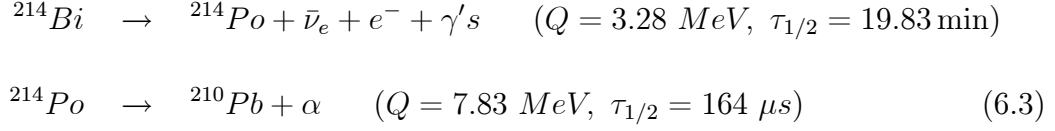
Figure 6.2: The event configuration and selection criteria for selecting correlated  $\beta - \alpha$  and  $\alpha - \alpha$  events.

the timing sequence in a typical event, as schematically shown in Figure 4.8, are illustrated in Figure 6.2. The measured activities were translated to contamination levels of their long-lived parent isotopes in the crystal assuming in the secular equilibrium. To find out the abundance of Uranium and Thorium contamination inside the crystal, five decay sequences (DS) were examined. These are given as follows:

1. within  $^{238}\text{U}$  series;
  - (DS<sub>1</sub>) the  $\alpha - \alpha$  signature from  $^{222}\text{Rn}$  via;

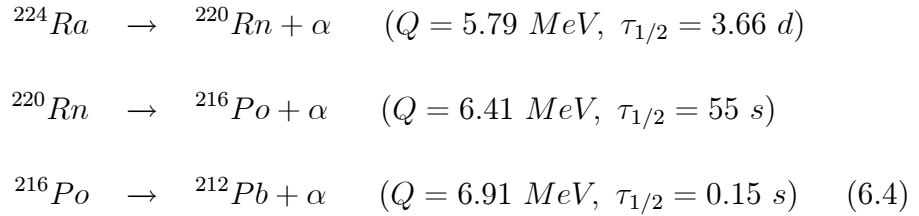


(DS<sub>2</sub>) the  $\beta - \alpha$  signature from  $^{214}\text{Bi}$  via;

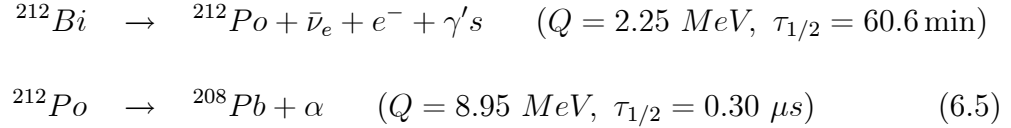


2. within  $^{232}\text{Th}$  series whose decay chain is shown in Figure 6.3;

- (DS<sub>3a,3b</sub>) the  $\alpha - \alpha - \alpha$  signature from  $^{224}\text{Ra} \rightarrow ^{220}\text{Rn} \rightarrow ^{216}\text{Po}$  via;

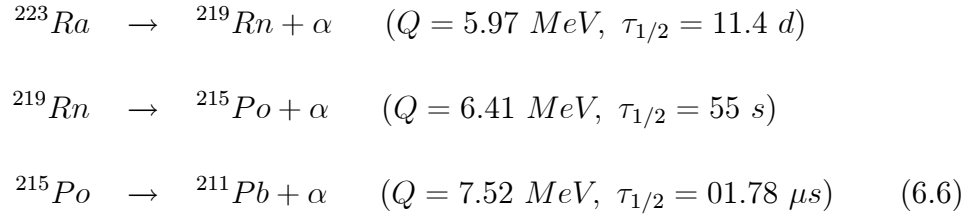


- (DS<sub>4</sub>) the  $\beta - \alpha$  signature from  $^{212}\text{Bi}$  via;



3. within  $^{235}\text{U}$  series;

(DS<sub>5a,5b</sub>) the  $\alpha - \alpha - \alpha$  signature from  $^{223}\text{Ra} \rightarrow ^{219}\text{Rn} \rightarrow ^{215}\text{Po}$  via;





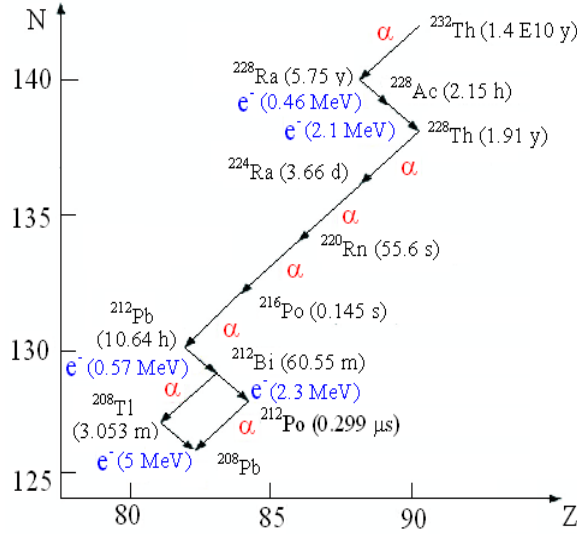


Figure 6.3: The schematic drawing of decay chain of Thorium,  $^{232}\text{Th}$ .

The energy spectrum of  $\alpha$ -events is depicted in Figure 6.4. The small peak at around 6  $\text{MeV}$  is due to the energy sum of those  $\beta - \alpha$  pairs in  $\text{DS}_4$  whose  $\Delta t$  is too small to be de-convoluted. Apart from this structure,  $\alpha$ -energy spectrum shows a broad peak at about 2.5  $\text{MeV}$ .

From time-dilation ( $\Delta t$ ) distribution of the correlated-events from  $\text{DS}_{1,2,3a,3b}$  decay half-lives measured in a good agreement with the nominal values. The  $\Delta t$  distributions of  $\text{DS}_{1,2,3a,3b}$  are shown in Figure 6.5a-d, respectively.

The sequence  $\text{DS}_4$  has  $\tau_{1/2}$  of 300  $\text{ns}$ , such that both pulses appear convoluted within the same readout time window of 12.5  $\mu\text{s}$ . An example of such signature is displayed in Figure 6.6a. The cascade was therefore selected not by timing but by pulse shape analysis. The time difference between the  $\beta$  and  $\alpha$  leading edges is displayed in Figure 6.6b where the best fit  $\tau_{1/2}$  is  $283 \pm 37 \text{ ns}$ , also in

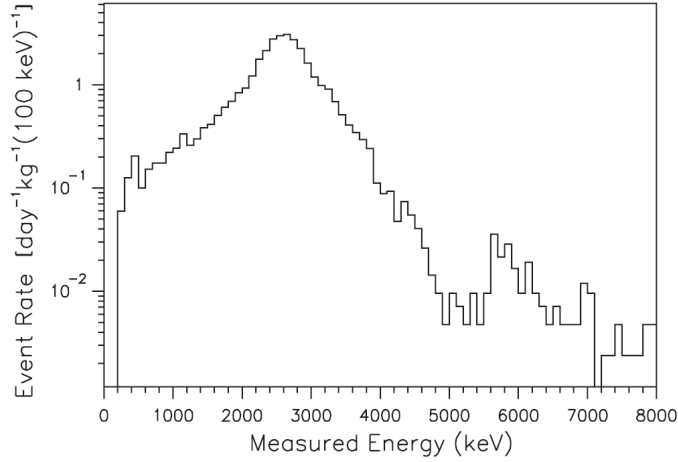


Figure 6.4: Measured energy spectrum for the  $\alpha$ -events.

good agreement with the reference value.

The sequence  $DS_{5a,5b}$  is another triple  $\alpha$ -cascade. However, the second delay with  $\tau_{1/2} = 1.78 \text{ ms}$  is well inside the DAQ dead time window (starting from  $500 \mu\text{s}$  after the trigger for a duration of about  $5 \text{ ms}$ ), such that this can not be measured. On the other hand, first decay with  $\tau_{1/2} = 3.96 \text{ s}$  is measurable. The time-difference plot is shown in Figure 6.7. No evidence of an exponential decay was observed, such that only an upper limit to the  $^{235}\text{U}$  series can be derived. The efficiencies, background level and the best fit half-lives are listed in Table 6.1. The measured activities and the derived contaminations of the four decay sequences of  $DS_{1,2,3a,3b,4,5a,5b}$  is given in Table 6.2. The measured activity in  $\text{mBqkg}^{-1}$  is converted to radiopurity level in units of gram per gram ( $\text{g/g}$ ) of the parent isotopes in CsI(Tl) crystal. Assuming secular equilibrium, the contamination levels of  $^{238}\text{U}$  and  $^{232}\text{Th}$  is listed in Table 6.2.

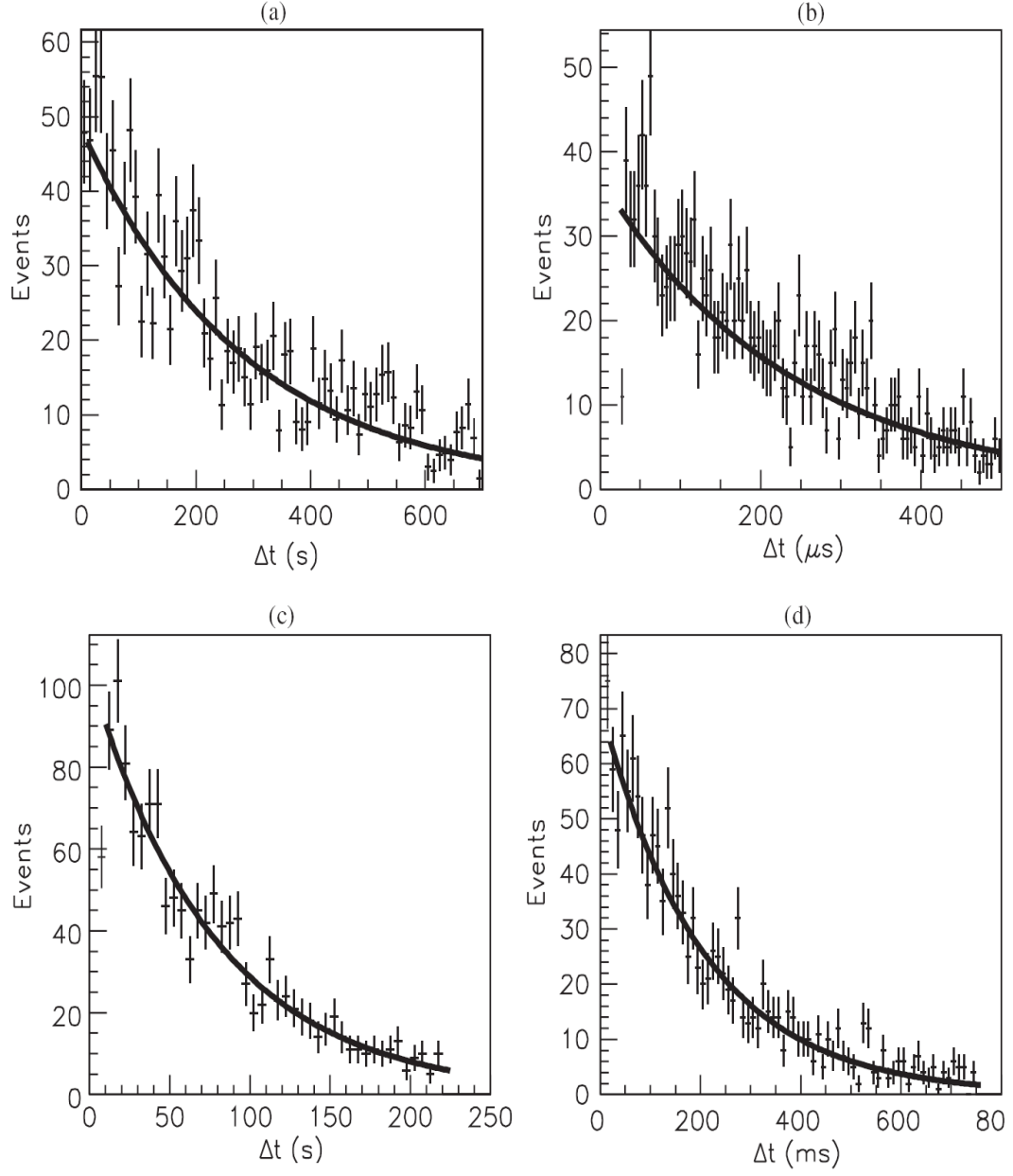


Figure 6.5: Delay time ( $\Delta t$ ) distributions for (a)  $\alpha - \alpha$  events from  $^{222}\text{Rn} \rightarrow ^{218}\text{Po} \rightarrow ^{214}\text{Pb}$  in  $\text{DS}_1$  (b)  $\beta - \alpha$  events from  $^{214}\text{Bi} \rightarrow ^{214}\text{Po} \rightarrow ^{210}\text{Pb}$  in  $\text{DS}_2$  (c)  $\alpha - \alpha$  events from  $^{224}\text{Ra} \rightarrow ^{220}\text{Rn} \rightarrow ^{216}\text{Po}$  in  $\text{DS}_{3a}$  (d)  $\alpha - \alpha$  events from  $^{220}\text{Rn} \rightarrow ^{216}\text{Po} \rightarrow ^{212}\text{Pb}$  in  $\text{DS}_{3b}$ .

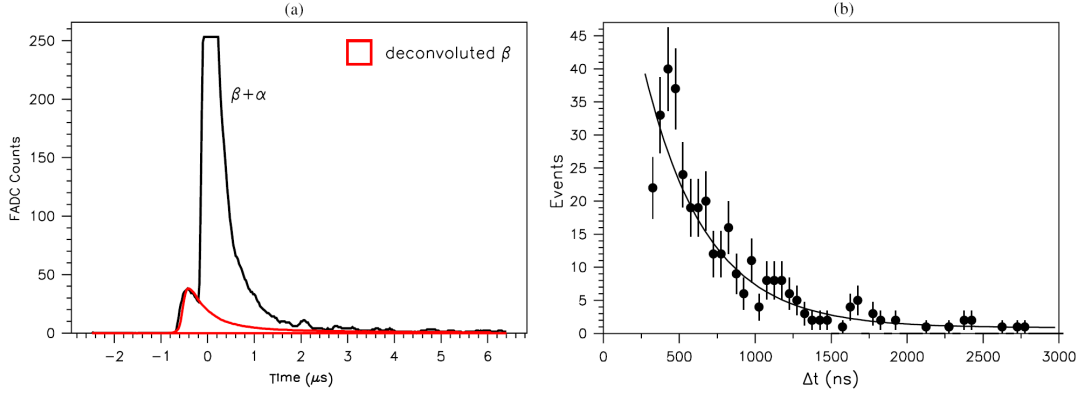


Figure 6.6: (a) Typical  $\beta - \alpha$  signal of cascade  $^{212}\text{Bi} \rightarrow ^{212}\text{Po} \rightarrow ^{208}\text{Pb}$  (b) the measured time difference between the leading edges in  $\beta$  and  $\alpha$  pulses.

Table 6.1: Summary of the selection efficiencies, background levels and measured half-lives of the decay sequences.

DS	Signature	Selection Efficiency	Background -to-signal	Half - life ( $\tau_{1/2}$ )	
				Nominal	Measured
1	$\alpha - \alpha$	0.93	0.51	3.10 min	$3.2 \pm 0.2$ min
2	$\beta - \alpha$	0.77	$3.2 \times 10^{-3}$	164 $\mu\text{s}$	$163 \pm 8$ $\mu\text{s}$
3a	$\alpha - \alpha$	0.86	—	55 s	$54.4 \pm 2.4$ s
3b	$\alpha$	0.97	$9 \times 10^{-5}$	0.15 s	$0.141 \pm 0.006$ s
4	$\beta - \alpha$	0.37	$3 \times 10^{-5}$	299 ns	$283 \pm 37$ ns
5a	$\alpha - \alpha$	0.78	—	3.96 s	No signal
5b	$\alpha$	—	—	1.78 ms	DAQ inactive

Table 6.2: Measured activities and derived contaminations of the four decay sequences.

DS	Measured activity ( $\text{mBqkg}^{-1}$ )	Contaminations of long-lived parents ( $\text{g/g}$ )	Contaminations of series ( $\text{g/g}$ )
1	$0.0107 \pm 0.0004$	$^{226}\text{Ra} : (2.92 \pm 0.11) \times 10^{-19}$	$^{238}\text{U} : (0.86 \pm 0.03) \times 10^{-12}$
2	$0.0102 \pm 0.0003$	$^{226}\text{Ra} : (2.79 \pm 0.07) \times 10^{-19}$	$^{238}\text{U} : (0.82 \pm 0.02) \times 10^{-12}$
3a, 3b	$0.0090 \pm 0.0002$	$^{228}\text{Th} : (2.97 \pm 0.08) \times 10^{-22}$	$^{232}\text{Th} : (2.23 \pm 0.06) \times 10^{-12}$
4	$0.0061 \pm 0.0003$	$^{228}\text{Th} : (3.1 \pm 0.2) \times 10^{-22}$	$^{232}\text{Th} : (2.3 \pm 0.1) \times 10^{-12}$
5a, 5b	$< 0.003$	$^{227}\text{Th} : < 1.6 \times 10^{-21}$	$^{235}\text{U} : < 4.9 \times 10^{-14}$

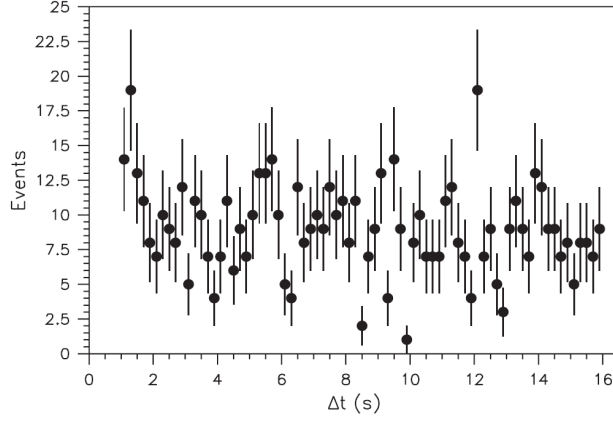


Figure 6.7: Delay time ( $\Delta t$ ) distribution for candidate  $\alpha - \alpha$  events for  $^{223}\text{Ra} \rightarrow ^{219}\text{Rn} \rightarrow ^{215}\text{Po}$  in DS<sub>5</sub>. No time-correlated events are identified in such that only an upper limit to decay rates can be set.

From the contamination levels of  $^{238}\text{U}$  and  $^{232}\text{Th}$  listed in Table 6.2 we can calculate the background contribution of intrinsic radiopurity in the region of above  $3\text{MeV}$ . Regarding very low level contamination (order of  $10^{-12}\text{g/g}$ ) of  $^{238}\text{U}$  and relatively lower total energy of all relevant decay chain (total energy around  $3\text{MeV}$ ), we can totally neglect the  $^{238}\text{U}$  effect in the region of interest. However, the  $^{232}\text{Th}$  contamination can contribute to the background via  $Tl-208$  decay chain shown in Figure 6.3. We can calculate the event rate of  $Tl-208$  (with 36% BR) by accepting measurement of the activity in the sequence of DS<sub>3a,3b</sub> given in Table 6.2 and using the efficiency factor of  $< 1\%$  from simulation in the case of electron and  $Tl-208$  decay chain gammas absorbing in the same crystal giving total energy of  $3 - 5\text{MeV}$ . The event rate of  $Tl-208$  is then  $< 0.009\text{mBqkg}^{-1} \times 36\% (BR) \times 1\% (sim) \simeq < 0.0032\text{cpd} (kg^{-1} \times day^{-1})$  which is also

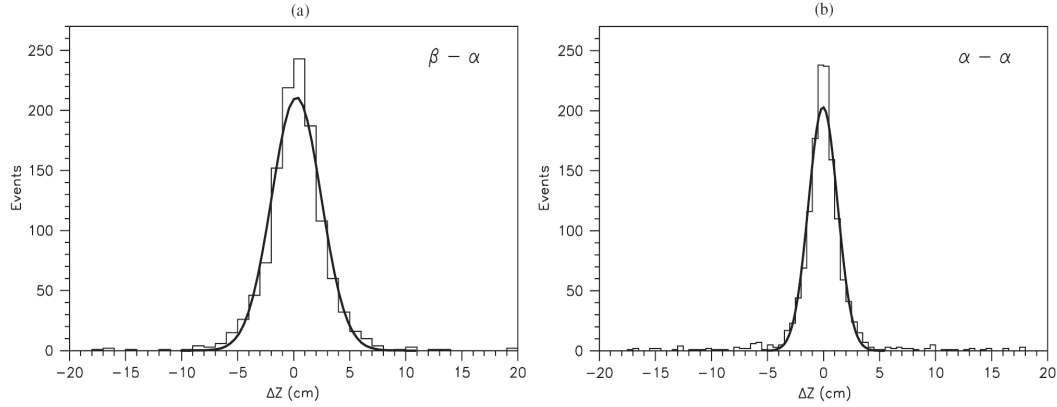


Figure 6.8: The  $\Delta Z$  distributions from a typical CsI(Tl) crystal on (a)  $\beta - \alpha$  and (b)  $\alpha - \alpha$  events, from which the Z resolutions  $\sigma_Z$  can be derived.

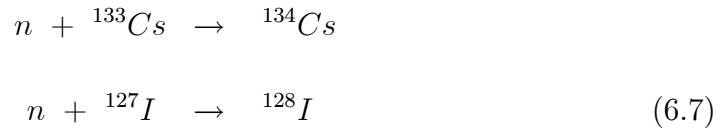
negligible level of background compared to our background level of about 0.4 in  $3 - 5$  MeV region.

Data taken with external collimated  $\gamma$ -sources prior to installation provided measurements of the Z-resolutions of 2 cm above 400 keV. This approach is limited by the intrinsic spread of the photon interaction sites within the crystal due to multiple Compton scatterings. A better in situ method is through the study of the measured position difference ( $\Delta Z$ ) of the correlated  $\beta - \alpha$  and  $\alpha - \alpha$  pairs which are emitted at the same site. The  $\Delta Z$  distributions of  $\beta - \alpha$  from DS<sub>2</sub> and the two  $\alpha - \alpha$  pairs from DS<sub>3a;3b</sub> for the combined data are depicted in Figure 6.8a,b. Both are centered at  $\Delta Z = 0$ , indicating that the selected pair of events were indeed originated at the same site. The resolution  $\sigma_Z$ , as given by the RMS of the distributions, are 2.2 cm and 1.3 cm for the  $\beta - \alpha$  and  $\alpha - \alpha$  events, respectively.

The  $\alpha - \alpha$  samples provide a more accurate description in the studies of the intrinsic spatial resolution, since both of the  $\alpha$ -pairs are originated at the same site. The  $\beta$ -events in DS<sub>2</sub>, on the other hand, are accompanied by other  $\gamma$ -emissions such that their exact vertices are not well-defined. This explains the worse  $\Delta Z$  distribution for the  $\beta - \alpha$  samples[83].

## 6.2 Understanding Environmental Background

Although ambient neutron is slowed down and stop by boron-loaded polyethylene, they still have probability to penetrate to the shielding and capture by the CsI(Tl) crystal target. Cosmic-induced neutrons originated from the target itself have high probability of leaving the target but residual neutrons can be captured by the target nuclei  $^{133}\text{Cs}$  and  $^{127}\text{I}$  via



with relatively large cross-section. The daughter isotope  $^{134}\text{Cs}$  ( $\tau_{1/2} = 2.05 \text{ yr}$ ,  $Q = 2.06 \text{ MeV}$ ) decays with 70% branching ratio by beta decay (end point 658  $\text{keV}$ ), plus the emission of two  $\gamma$ 's of 605 and 796  $\text{keV}$ . Therefore, it will not give rise to single hit at the low-energy region. By studying multi-hit events giving total energy of around 2  $\text{MeV}$ , we observed the signature of  $^{134}\text{Cs}$  in the CsI(Tl) data at the low energy region. The energy spectrum of 2-hit in that energy region as well as the Z distribution of these events are shown in

Figure 6.9. The uniform Z-distribution of  $\gamma$ 's due to  $^{134}\text{Cs}$  shows us the source is internal to the crystal. The isotope  $^{128}\text{I}$  ( $\tau_{1/2} = 25$  min,  $Q = 2.14$  MeV) on the other hand, has a branching ratio of 79% having a lone beta decay, which will mimic the single hit signature. The neutron capture rate by the CsI(Tl) target can be measured by tagging  $\gamma$  bursts of energy 6.8 MeV. Knowing the capture rate, the contributions to the low-energy background due to  $^{128}\text{I}$  can be evaluated and subtract off[55]. By analyzing the mulhi-hit spectra we also observed signature of the  $^{60}\text{Co}$  energy peaks of 1173 keV (99.86%) and 1332 keV (99.98%) in the 2 – hit individual energy spectrum of events having total energy of 2 – 3 MeV region. The energy spectrum and Z distribution of these events are shown in Figure 6.10. In this energy region we clearly observed the two energy peaks of  $^{60}\text{Co}$  at 1173 keV and 1332 keV and also  $^{208}\text{Tl}$  originated pair production one-escape peaks of 511 and 2105 keV in the energy spectrum. The uniform  $^{60}\text{Co}$  Z-distribution along the crystal shows  $^{60}\text{Co}$  spread out all around the surface via dust in the environment. The Z distribution of the other peaks related to  $^{208}\text{Tl}$  pair-production is consistent with external source behavior.

When we study higher energies of non-cosmic events up to around 4 MeV via multi-hit analyzing, shown in Figure 6.11 we concluded that all energy peaks are related to  $^{208}\text{Tl}$  decay chain of 2614.53 keV (99%), 510.77 keV (25%), 583.19 keV (86.2%), 860.56 keV (12.77%)[84]<sup>1</sup> and their combinations. This phenomenon indicates that  $^{208}\text{Tl}$  can contribute to the background up to around 4 MeV.

---

<sup>1</sup> Generated at NNDC by WebTREND Sun Oct 22 22:00:23 2006



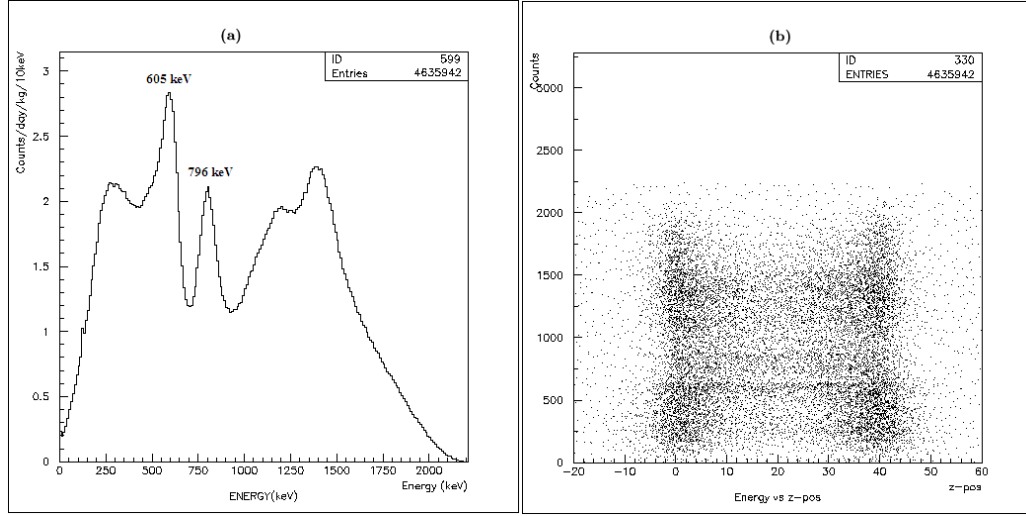


Figure 6.9: (a) The energy spectrum of 2 – *hit* non-cosmic events, total energy is 1 – 2 *MeV* showing  $^{134}\text{Cs}$  signature in CsI(Tl) data (b) Z-distribution of these events, uniform distribution indicates the source is internal to the crystal.

To understand the phenomenon of multiple-hit in the detector deeply, one must understand the nature of the decay process of the sources and must consider the angular correlation between successive gamma cascade transitions. We have studied angular correlation of gamma cascades from *Co*–60 and *Tl*–208 theoretically. Simulation results based on the theoretical formalism are very consistent with the data.

### 6.3 Angular Correlation of Gamma Radiation[85]

The angular correlation of successive nuclear gamma radiation can be expressed in terms of initial angular momentum  $j_1$ , successive transformations either emitting or absorbing gamma radiations through intermediate nuclear

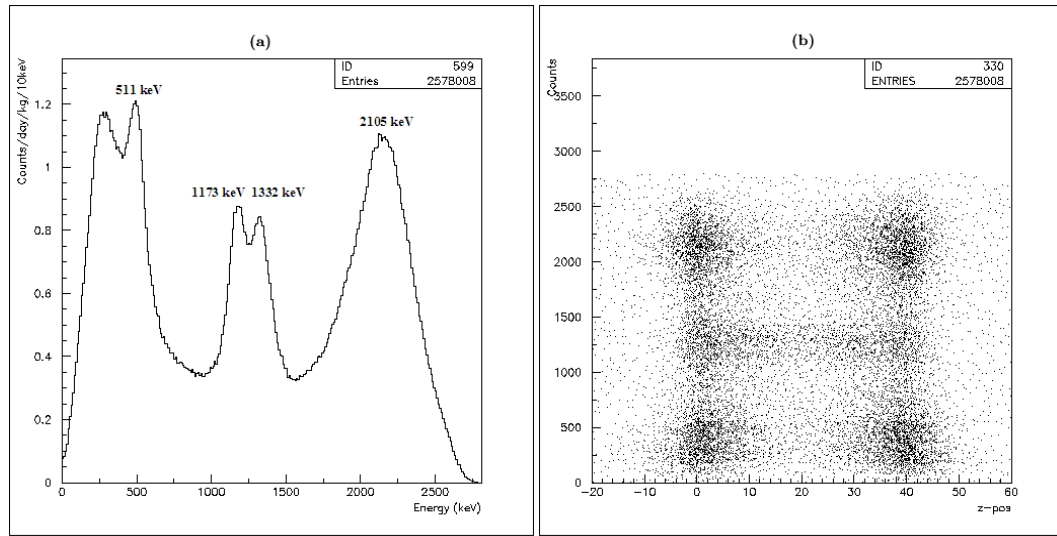


Figure 6.10: (a) The energy spectrum of 2 – *hit* non-cosmic events, total energy is 2 – 3 MeV showing  $^{60}\text{Co}$  signature and  $^{208}\text{Tl}$  pair-production one escape peaks in CsI(Tl) data (b) Z-distribution of these events showing  $^{208}\text{Tl}$  source external to the crystal and  $^{60}\text{Co}$  source spread out along the crystal as dust.

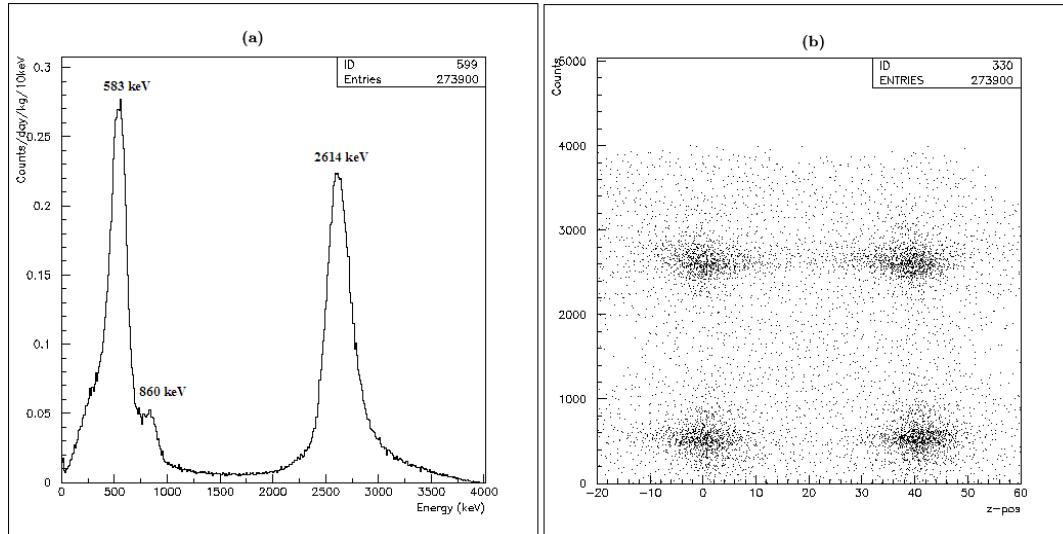


Figure 6.11: (a) The energy spectrum of 2 – *hit* non-cosmic events, total energy is 3 – 4 MeV showing  $^{208}\text{Tl}$  signature in CsI(Tl) data (b) Z-distribution of these events, non-uniform distribution indicates the source is external to the crystal.

states  $j$  and final angular momentum  $j_2$ . In the general formulation the initial and final nuclear states are taken as randomly oriented. The  $\gamma - \gamma$  correlation function is

$$\begin{aligned}
W(\theta) = & \sum \langle j_1 | L_1 | j \rangle \langle j_1 | L'_1 | j \rangle \langle j_2 | L_2 | j \rangle \langle j_2 | L'_2 | j \rangle \\
& \times C(L_1 L'_1 \nu; 1 - 1) C(L_2 L'_2 \nu; 1 - 1) \\
& \times W(jj L_1 L'_1; \nu j_1) W(jj L_2 L'_2; \nu j_1) \\
& \times [(2L_1 + 1)(2L'_1 + 1)(2L_2 + 1)(2L'_2 + 1)]^{\frac{1}{2}} \times P_\nu(\cos \theta) \quad (6.8)
\end{aligned}$$

$W(\theta)$  is the probability that the angle between the directions of two cascade  $\gamma$ -rays is  $\theta$ . The sum is over  $L_1 L'_1$ ,  $L_2 L'_2$  and  $\nu$ . Here  $C(L_1 L'_1 \nu; 1 - 1)$  is the Clebsch-Gordan parameters and  $W(jj L_1 L'_1; \nu j_1)$  is the Racah parameters which are the sum of products of the Clebsch-Gordan parameters.

The  $\gamma - \gamma$  correlation function for pure  $2^{L_1} - 2^{L_2}$  multipoles can be written in terms of functions of Legendre polynomial as

$$W(\theta) = \sum_{n=0} A_{2n}(L_1, L_2) P_{2n}(\cos \theta) \quad (6.9)$$

where  $A_\nu = F_\nu(L_1 j_1 j) F_\nu(L_2 j_2 j)$ , renormalized so that  $A_0 = 1$  and

$$F_\nu(L j_1 j) = (-)^{j_1 - j - 1} (2j + 1)^{\frac{1}{2}} (2L + 1) C(LL \nu; 1 - 1) W(jj LL; \nu j_1) \quad (6.10)$$

so that also  $F_0 = 1$ .

For the correlation in which one  $\gamma$ -ray is not pure, the correlation function

can be simplified as

$$W(\theta) = W_I(\theta) + \delta^2 W_{II}(\theta) + 2\delta W_{III}(\theta) \quad (6.11)$$

where  $\delta^2$  is the ratio of intensities of the  $2^{L'_1}$  pole to that of the  $2^{L_1}$  pole and

$$\begin{aligned} W_I(\theta) &= \sum_{n=0} A_{2n}(L_1, L_2) P_{2n}(\cos \theta) \\ W_{II}(\theta) &= \sum_{n=0} A_{2n}(L'_1, L_2) P_{2n}(\cos \theta) \\ W_{III}(\theta) &= (-)^{j-j_1-1} [(2j+1)(2L_1+1)(2L_2+1)]^{\frac{1}{2}} \\ &\quad \times \sum_{n=0} G_{2n}(L_1 L'_1 j_1 j) F_{2n}(L_2 j_2 j) P_{2n}(\cos \theta) \end{aligned} \quad (6.12)$$

where  $F_\nu$  is given in Equation (6.10) and  $G_\nu$  is

$$G_\nu(L_1 L'_1 j_1 j) = C(L_1 L'_1 \nu; 1-1) W(jj L_1 L'_1; \nu j_1) \quad (6.13)$$

symmetric in  $L_1$  and  $L'_1$ .

*Co-60* decays mainly by beta decays to the  $4^+$  state in *Ni-60*, which then decays by the cascade  $4^+(E2)2^+(E2)0^+$  to the ground state of *Ni-60*. The successive 1173 keV and 1332 keV  $\gamma-\gamma$  transitions are pure  $2^2-2^2$  multipoles. Then theoretical correlation is[86],

$$\begin{aligned} W(\theta) &= 1 + F_2(2, 4, 2) F_2(2, 0, 2) P_2(\cos \theta) + F_4(2, 4, 2) F_4(2, 0, 2) P_4(\cos \theta) \\ &= 1 + 0.102 P_2(\cos \theta) + 0.009 P_4(\cos \theta) \\ W(\theta) &= (1 + 0.1250 \cos^2 \theta + 0.0417 \cos^4 \theta) \times const. \end{aligned} \quad (6.14)$$

where  $F_2$  and  $F_4$  functions are calculated by using Equation (6.10).

$^{208}\text{Tl}$  decay chain of 583.19  $\text{keV}$  and 2614.53  $\text{keV}$  gamma transitions via  $5^-(E2)3^-(E3)0^+$  are pure  $2^2 - 2^2$  multipoles. Then theoretical correlation is

$$\begin{aligned} W(\theta) &= 1 + F_2(2, 5, 3)F_2(3, 0, 3)P_2(\cos \theta) + F_4(2, 5, 3)F_4(3, 0, 3)P_4(\cos \theta) \\ &= 1 + 0.1786P_2(\cos \theta) - 0.0043P_4(\cos \theta) \\ W(\theta) &= (1 + 0.3125 \cos^2 \theta - 0.0208 \cos^4 \theta) \times \text{const.} \end{aligned} \quad (6.15)$$

$^{208}\text{Tl}$  decay chain of 860.56  $\text{keV}$  and 2614.53  $\text{keV}$  gamma transitions via  $4^-(M1 + E2)3^-(E3)0^+$  are not pure but first transition mix  $2^1 - 2^2$  multipoles.  $\delta$ , the ratio between the intensities of the  $2^1$  pole and that of the  $2^2$  pole is  $\delta = 0.014$ . Then theoretical correlation is

$$\begin{aligned} W_I(\theta) &= 1 + F_2(1, 4, 3)F_2(3, 0, 3)P_2(\cos \theta) \\ W_{II}(\theta) &= 1 + F_2(2, 4, 3)F_2(3, 0, 3)P_2(\cos \theta) + F_4(2, 4, 3)F_4(3, 0, 3)P_4(\cos \theta) \\ W_{III}(\theta) &= (7 \times 3 \times 5)^{1/2}(G_2(1, 2, 4, 3)F_2(3, 0, 3)P_2(\cos \theta) \\ W(\theta) &= W_I(\theta) + \delta^2 W_{II}(\theta) + 2\delta W_{III}(\theta) \\ &= 1 - 0.125P_2(\cos \theta) + (0.014)^2[1 - 0.2679P_2(\cos \theta) + 0.03175P_4(\cos \theta)] \\ &\quad + 2(0.014)[-0.62498P_2(\cos \theta)] \\ W(\theta) &= (1 - 0.1996 \cos^2 \theta + 0.000025 \cos^4 \theta) \times \text{const.} \end{aligned} \quad (6.16)$$

$^{208}\text{Tl}$  decay chain of 510.77  $\text{keV}$  and 583.19  $\text{keV}$  gamma transitions via  $5^-(M1 + E2)5^-(E2)3^-$  are not pure but first transition mix  $2^1 - 2^2$  multipoles.

$\delta$ , the ratio between the intensities of the  $2^1$  pole and that of the  $2^2$  pole is  $\delta = -0.051$ . Then theoretical correlation is

$$\begin{aligned}
W_I(\theta) &= 1 + F_2(1, 5, 5)F_2(2, 3, 5)P_2(\cos \theta) \\
W_{II}(\theta) &= 1 + F_2(2, 5, 5)F_2(2, 3, 5)P_2(\cos \theta) + F_4(2, 5, 5)F_4(2, 3, 5)P_4(\cos \theta) \\
W_{III}(\theta) &= -(11 \times 3 \times 5)^{1/2}(G_2(1, 2, 5, 5)F_2(2, 3, 5)P_2(\cos \theta) \\
W(\theta) &= W_I(\theta) + \delta^2 W_{II}(\theta) + 2\delta W_{III}(\theta) \\
&= 1 + 0.186P_2(\cos \theta) + (-0.051)^2[1 - 0.119P_2(\cos \theta) + 0.127P_4(\cos \theta)] \\
&\quad + 2(-0.051)[-0.115P_2(\cos \theta)] \\
W(\theta) &= (1 + 0.3257 \cos^2 \theta + 0.0016 \cos^4 \theta) \times const. \tag{6.17}
\end{aligned}$$

The angular correlation functions of successive  $\gamma - \gamma$  transitions for  $Co - 60$  and  $Tl - 208$  are shown in Figure 6.12.

Since both sources of  $Co - 60$  and  $Tl - 208$  are external to the crystal, in the simulation study we generate uniformly distributed gammas from outside. For  $Co - 60$  we generate isotropic, spherically symmetric gammas and for  $Tl - 208$  we generate uniformly distributed gammas in the crystal side since candidate sources are located in the PMT and its bases. The simulation results of correlated successive  $Co - 60$  and  $Tl - 208$  decay gammas are shown in Figure 6.13. The simulation results are in good agreement with the data shown in Figure 6.10 and Figure 6.11. These simulation results show the successive decay gammas hit the same crystal at the same time giving total energy of 2505  $keV$  for  $Co - 60$

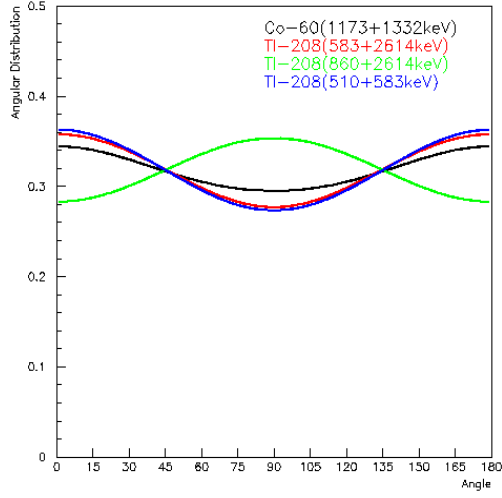


Figure 6.12: Angular correlation function distribution of Tl-208 and Co-60 gamma cascades.

and up to around 4  $MeV$  for  $Tl - 208$ .

#### 6.4 Single Hit (SH) Prediction via Multiple Hit (MH) Analysis

According to the multi-hit analysis which is based on taking ratio of multiple-hit cosmic events with non-cosmic events, nearly all of the background is originated by cosmic rays in 4 – 6.5  $MeV$  region. The comparison of spectra due to cosmic and non-cosmic events with respect to energies through 3 – 8  $MeV$  are illustrated in Figure 6.14. From Figures 6.14a-b it can be seen that cosmic and non-cosmic spectra for energy region of 3 – 3.5  $MeV$ , 3.5 – 4  $MeV$ , respectively do not match well since the event origins are different (due to effect of  $Tl - 208$  radioactivity). In 3 – 3.5  $MeV$  energy region  $Tl - 208$  decay chain gammas of 583.19  $keV$  and 2614.53  $keV$  are dominant and also it can be seen the effect

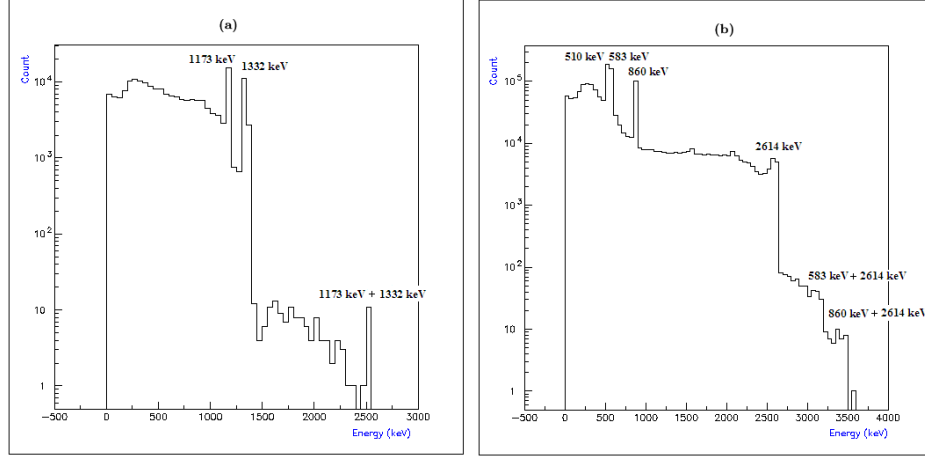


Figure 6.13: The simulation results of correlated (a) Co-60 successive decay gammas (b) Tl-208 successive decay gammas, showing very good agreement with the multiple-hit data analysing.

of  $860.56 \text{ keV}$  and  $2614.53 \text{ keV}$  as well. In the  $3.5 - 4 \text{ MeV}$  energy region it can be seen  $Tl - 208$  decay chain gammas of  $860.56 \text{ keV}$  and  $2614.53 \text{ keV}$  and cosmic effect mix together. In this energy region except  $Tl - 208$  decay chain gammas, cosmic and non-cosmic events match very well. That means after elimination of  $Tl - 208$  contribution, one can make SH estimation in the  $3 - 4 \text{ MeV}$  energy region due to cosmic ray inefficiency. On the other hand, from the Figures 6.14c-d for energy region of  $4 - 6 \text{ MeV}$  cosmic and non-cosmic spectra match very well showing the event origins are totally only cosmic rays. From the Figures 6.14e-f the cosmic and non-cosmic events match but with different normalization factor. This is an evidence of presence of another source in this energy region. Actually, as it can be seen in the Figure 5.20 there is a peak in the  $SH$  energy spectra in the  $6.5 - 8 \text{ MeV}$  energy region. This effect is nothing



but due to copper, which is abundant in the shielding materials, de-excitation gammas. Unlike the  $Tl - 208$ , copper de-excitation gammas are not correlated and just burst of many high energetic gammas of  $6.5 - 8 \text{ MeV}$ .

We can formulate the event rate  $R$  for  $\bar{\nu}_e e$  scattering in Reactor  $ON$  as

$$R(ON) = R_{SM}(\sin^2 \theta_W) + R(BKG) \quad (6.18)$$

where  $R(ON)$ ,  $R(OFF)$  and  $R(BKG)$  are the event rate of Reactor  $ON$ , Reactor  $OFF$  and Background, respectively. We can consider  $R(BKG)$  as  $R(OFF)$  or event rate of  $SH$  prediction  $R(SH_{pred.})$ .

One can make estimation of background in  $3 - 8 \text{ MeV}$  energy region due to cosmic ray inefficiency and  $Tl - 208$ , we can perform  $ON - SH_{pred.}$  instead of Reactor  $ON - OFF$  method. By using this idea we can make a background estimation based on Reactor  $ON$  data itself instead of time limited Reactor  $OFF$  data, leading us to achieve better results. By using Reactor  $ON$  data itself to obtain background level also give the opportunity of making a measurement without worrying about stability, systematic errors due to reactor, detector, software, hardware etc. since we are using the same data sets in both cases. By using the definition below given in Equation (6.19) to make estimation of background due to cosmic ray veto efficiency, for the statistical error we used binomial error definition since the prediction formula is an binomial expression.

$$\frac{(MH)_{non-cos}}{(MH)_{Tot}} = 1 - \varepsilon = \frac{SH_{pred.}}{(SH)_{Tot}} \quad (6.19)$$

where  $\varepsilon$  is cosmic ray veto efficiency factor;  $(MH)_{\text{cos}}$  is the number of multiple-hit of cosmic events,  $(MH)_{\text{non-cos}}$  is the number of multiple-hit of non-cosmic events, and  $(MH)_{\text{Tot}} = (MH)_{\text{cos}} + (MH)_{\text{non-cos}}$ ;  $(SH)_{\text{cos}}$  is the number of single-hit of cosmic events,  $(SH)_{\text{non-cos}}$  is the number of single-hit of non-cosmic events, and  $(SH)_{\text{Tot}} = (SH)_{\text{cos}} + (SH)_{\text{non-cos}}$ .

The expected event rate  $R$  for  $\bar{\nu}_e e$  scattering and the statistical measurement error in Reactor  $ON - OFF$  method can be written in  $cpd$  ( $kg^{-1} \times day^{-1}$ ) unit as given in Equation (6.20).

$$\begin{aligned}
R_{SM}(\sin^2 \theta_W) &= \frac{SH_{on}(E)}{m \times T_{on}} - \frac{SH_{off}(E)}{m \times T_{off}} \\
\delta_{ON-OFF}(E) &= \sqrt{\delta_{on}^2(E) + \delta_{off}^2(E)} \\
&= \sqrt{\frac{SH_{on}(E)}{m^2 \times T_{ON}^2} + \frac{SH_{off}(E)}{m^2 \times T_{OFF}^2}} \quad (6.20)
\end{aligned}$$

The expected event rate  $R$  for  $\bar{\nu}_e e$  scattering and the statistical measurement error in Reactor  $ON - SH_{pred.}$  method can be written in  $cpd$  ( $kg^{-1} \times day^{-1}$ ) unit as given in Equation (6.21) by accepting the binomial distribution mean value of  $Np$  and its standard deviation of  $\sqrt{Npq}$  as shown in Equation (6.22).

$$SH_{pred.} = (SH)_{Tot} \times \frac{(MH)_{non-cos}}{(MH)_{Tot}} \quad (6.21)$$

$$\begin{aligned}
R_{SM}(\sin^2 \theta_W) &= \frac{SH_{on}(E)}{m \times T_{ON}} - \frac{SH_{pred.}(E)}{m \times T_{ON}} \\
\delta_{SH_{pred.}}(E) &= \sqrt{\frac{SH_{Tot}(E)}{m^2 \times T_{ON}^2} \frac{MH_{non-cos}(E)}{MH_{Tot}(E)} \frac{MH_{cos}(E)}{MH_{Tot}(E)}} \\
\delta_{ON-SH_{pred.}}(E) &= \sqrt{\delta_{SH_{pred.}}^2(E) + \delta_{on}^2(E)}. \quad (6.22)
\end{aligned}$$

where  $T$  is the time and  $m$  is the active mass (in  $kg$ ) of the detector, and  $\delta$  is the

statistical error. The mass and time are much more precisely known terms whose errors can be negligible and statistical error only depend on the measurement of the number of count.

For Single-Hit Prediction the measurement based on comparison of pair production  $3 - Hit$  cosmic events with the non-cosmic events for  $3 - 8 \text{ MeV}$  energy region was performed. Since in  $3 - 4 \text{ MeV}$  energy region  $Tl - 208$  effect is present and our estimation is based on the background originates from cosmic rays, the estimation, of course, does not work properly. The physics idea is that due to cosmic ray inefficiency, the cosmic rays give a mimic signature of single hit event resulting an avoidable background in the region of interest. The spectra of Multiple-Hit ( $3 - Hit$ ) of pair production and Single Hit for cosmic and non-cosmic events are shown in Figure 6.15a-b. By taking ratio of multiple hit of non-cosmic and cosmic ray events with respect to energy region, we can calculate the cosmic ray veto efficiency and make a Single-Hit predictions due to cosmic rays in the corresponding energy regions as shown in the expression of (6.19).

From Multi-Hit comparison analysis in Period-II by using Equation (6.19), the cosmic ray veto efficiency factor, which is energy independent factor, was calculated as  $\sim 93\%$ . This efficiency factor lead us to make a prediction of  $SH$  due to cosmic rays shown in Table 6.3. For  $6.5 - 8 \text{ MeV}$  energy region due to copper effect, the efficiency factor drops but our  $SH$  prediction based on

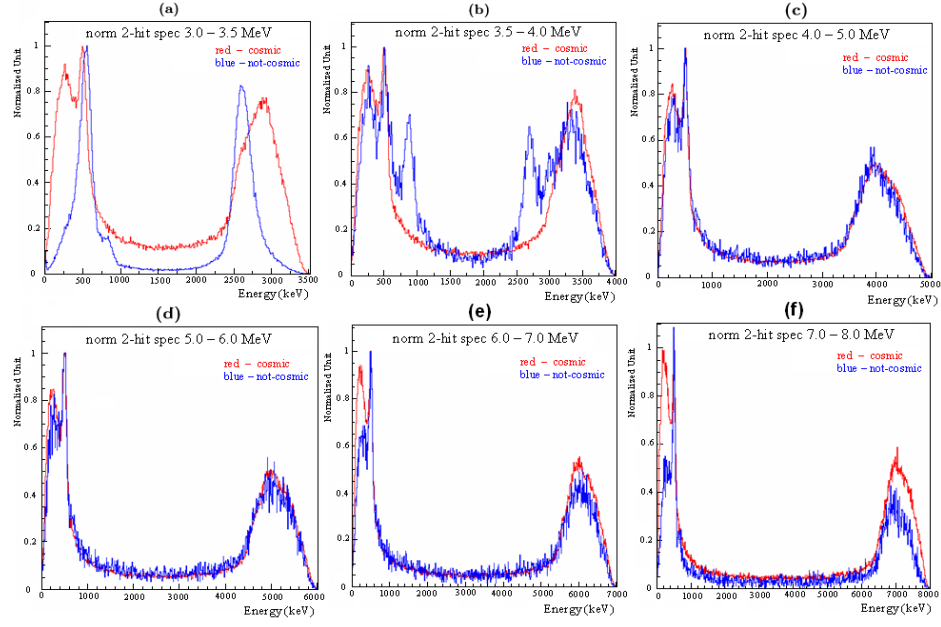


Figure 6.14: Comparison of 2-hit cosmic and non-cosmic events energy spectra with respect to energy region through 3 – 8 MeV (a) 3 – 3.5 MeV (b) 3.5 – 4 MeV (c) 4 – 5 MeV (d) 5 – 6 MeV (e) 6 – 7 MeV (f) 7 – 8 MeV.

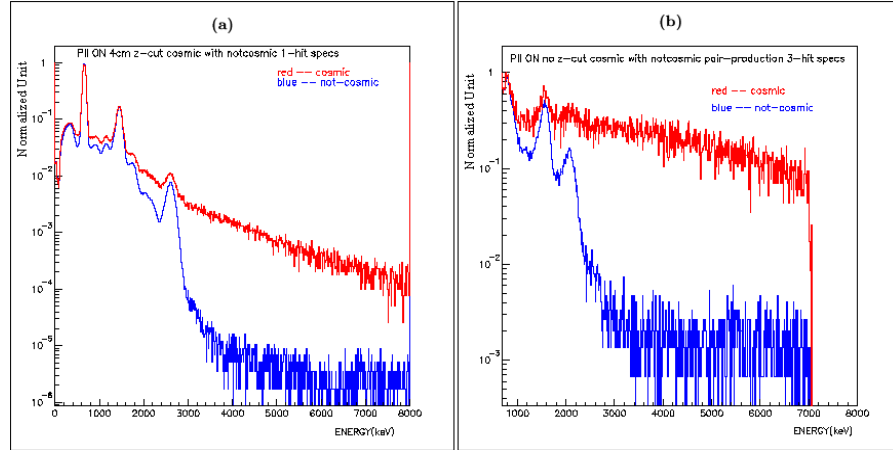


Figure 6.15: The normalized cosmic and non-cosmic energy spectra of (a) Single Hit Events (b) 3-HIT pair-production residue events which are accompanied with  $2 \times 511 \text{ keV}$  back to back gamma events.

Equation (6.19) still works. This can be explained by the effect of copper on  $(MH)_{non-cosmic}$  and  $SH_{pred.}$  are cancel out, since copper emits only one gamma at a time and no correlation between the burst of gammas. However, this effect only gives harmless inevitable efficiency conflict.

In the  $3 - 4 \text{ MeV}$  energy region the estimation does not work since the background is rather complex due to  $Tl - 208$  decay chain gammas. Since there are several combination of  $Tl - 208$  decay chain gammas and the effect of  $(MH)_{non-cosmic}$  and  $SH_{pred.}$  are not cancel out unlike the copper, the prediction must be done for cosmic and  $Tl - 208$  separately.

For the estimation of  $SH$  in the energy region of  $3 - 4 \text{ MeV}$ , we should estimate  $Tl - 208$  contribution as well as cosmic rays. We use Monte Carlo Simulation for the correlated successive gammas of  $Tl - 208$ . We measured the crystal distance of hits in data (seperately for  $2614.53 \text{ keV} + 583.19 \text{ keV}$  hits and  $2614.53 \text{ keV} + 860.56 \text{ keV}$  hits), except *zero* crystal distance (meaning that  $SH$ ). However, in the Monte Carlo we can have all hit points including also *zero* crystal distance. Thus *zero* crystal distance ( $SH$ ) can be predicted from the best fit of simulation to the data.

In the data we can measure no z-cut crystal distance hits of  $Tl - 208$  gammas since our target is now all detector and including  $20 + 20 \text{ cm}$  crystals which we do not have exact z information. However, we want to estimate  $Tl - 208 \text{ SH}$  contribution only in the  $40 \text{ cm}$  crystals as an our target after  $4 \text{ cm}$  z-cut. For

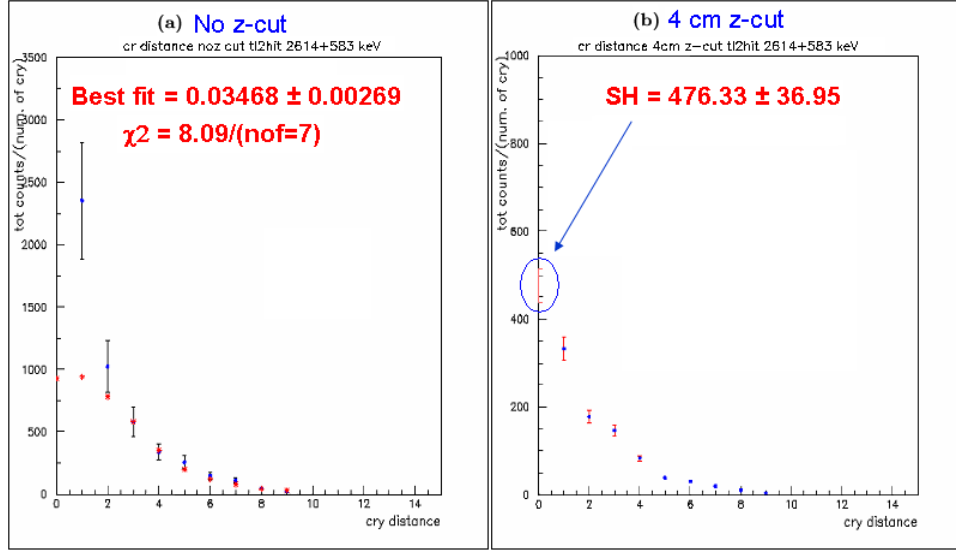


Figure 6.16: For Period-II  $Tl-208$  2614+580  $keV$  successive gamma hits crystal distance distributions of (a) no z-cut to get the parameter from the best fit of simulation with the data (b) simulation of 4 cm z-cut after applying the fitting parameter to make a prediction of SH in 3 – 3.5  $MeV$  region.

this purpose our procedure is that fit simulation with the data for no z-cut distributions and apply the fitting parameter from the best fit to the 4  $cm$  z-cut simulation distribution to predict *zero* crystal distance  $SH$  in our target 40  $cm$  crystals with 4  $cm$  z-cut.

For Period-II Reactor  $ON$  the  $SH$  prediction of  $Tl-208$  successive gammas was done as shown in Figures 6.16, 6.17 and 6.18. In 3 – 3.5  $MeV$  energy region for 2614.53  $keV$  + 583.19  $keV$  combination  $476.33 \pm 36.95$  counts and for 2614.53  $keV$  + 860.56  $keV$  combination  $32.93 \pm 4.77$  counts were estimated. This gives totally  $509.26 \pm 37.26$  counts which is 54% of the background in 3 – 3.5  $MeV$  energy region. In 3.5 – 4  $MeV$  energy region for 2614.53 $keV$  + 860.56  $keV$

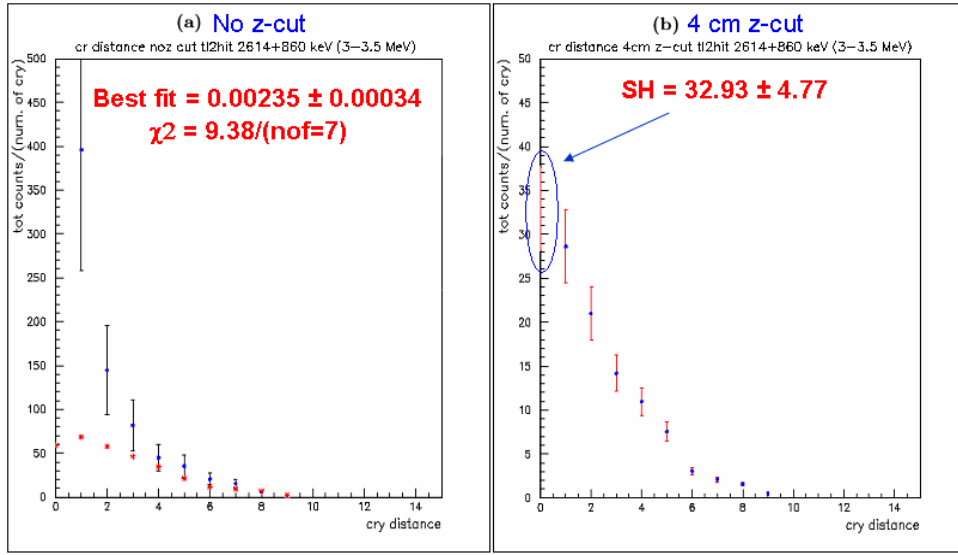


Figure 6.17: For Period-II  $Tl-208$  2614+860  $keV$  successive gamma hits crystal distance distributions of (a) no z-cut to get the parameter from the best fit of simulation with the data (b) simulation of 4 cm z-cut after applying the fitting parameter to make a prediction of SH in 3 – 3.5  $MeV$  region.

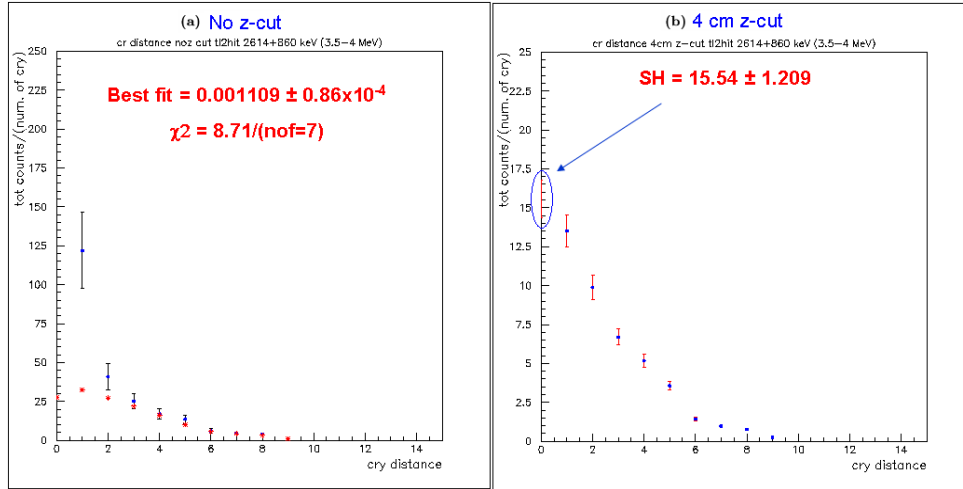


Figure 6.18: For Period-II  $Tl-208$  2614+580  $keV$  successive gamma hits crystal distance distributions of (a) no z-cut to get the parameter from the best fit of simulation with the data (b) simulation of 4 cm z-cut after applying the fitting parameter to make a prediction of SH in 3.5 – 4  $MeV$  region.

Table 6.3: For Period-II the background estimation in Reacor ON due to Cosmic Ray and Tl-208 in 3-8 MeV with 0.5 MeV bin size.

$Energy$ ( $MeV$ )	$ON$ ( $count$ )	$(SH)_{pred.}$ ( $count$ )	$ON - SH_{pred.}$ $cpd (kg^{-1} \times day^{-1}) \times 10^{-2}$
3.0 – 3.5	$961 \pm 31.0$	$937.64 \pm 42.23$	$0.535 \pm 1.200$
3.5 – 4.0	$292 \pm 17.09$	$287.15 \pm 15.93$	$0.111 \pm 0.535$
4.0 – 4.5	$193 \pm 13.89$	$188.63 \pm 13.24$	$0.100 \pm 0.439$
4.5 – 5.0	$141 \pm 11.87$	$128.34 \pm 10.92$	$0.290 \pm 0.369$
5.0 – 5.5	$117 \pm 10.82$	$91.36 \pm 9.21$	$0.587 \pm 0.325$
5.5 – 6.0	$81 \pm 9.0$	$66.41 \pm 7.85$	$0.334 \pm 0.274$
6.0 – 6.5	$55 \pm 7.42$	$50.55 \pm 6.85$	$0.102 \pm 0.231$
6.5 – 7.0	$77 \pm 8.77$	$79.08 \pm 8.26$	$-0.048 \pm 0.276$
7.0 – 7.5	$76 \pm 8.72$	$84.10 \pm 8.26$	$-0.185 \pm 0.275$
7.5 – 8.0	$73 \pm 8.54$	$60.89 \pm 7.07$	$0.277 \pm 0.254$

combination  $15.54 \pm 1.21$  counts were estimated which is 5% of the background.

For Period-II Reactor  $ON$  data taking, the results for  $SH_{pred.}$  based on the prediction for the cosmic rays given in Equation (6.21) and  $Tl-208$  contribution for energy regions are summarized in Table 6.3.

Similarly, from Multi-Hit comparison analysis in Period-III the cosmic ray veto efficiency factor was calculated as  $\sim 86.5\%$  by using Equation (6.19). This efficiency factor shows us cosmic tagging in Period-III is worse than in Period-II. This is the explanation of relatively higher background in Period-III. Using Reactor  $ON$  period data itself to make SH prediction is therefore very important and background level whatever it is can be subtract off successfully.

The  $SH$  prediction of  $Tl-208$  successive gammas for Period-III Reactor  $ON$  was done as shown in Figures 6.19, 6.20 and 6.21. In  $3 - 3.5 MeV$  energy region, for  $2614.53 keV + 583.19 keV$  combination  $471.11 \pm 34.34$  counts and for



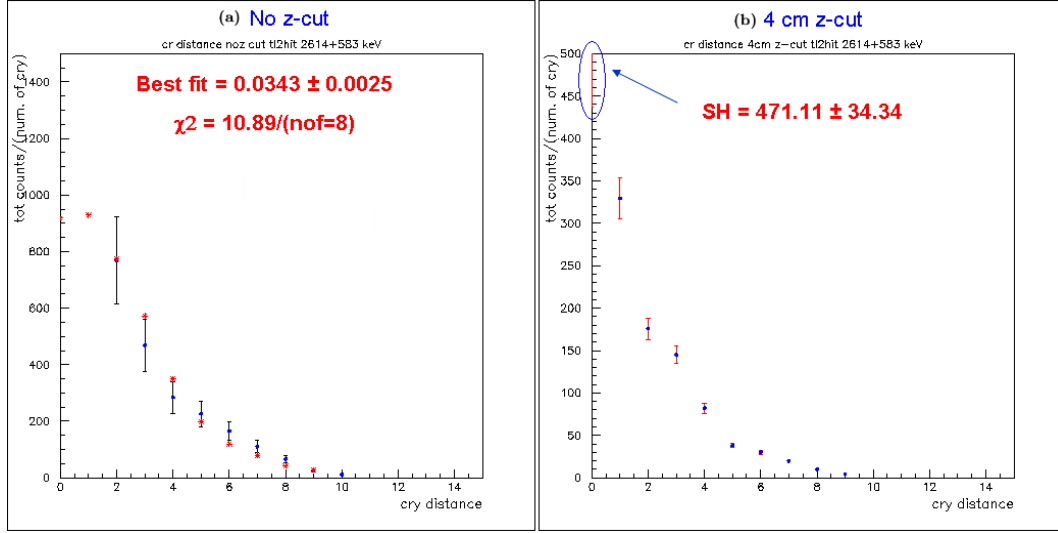


Figure 6.19: For Period-III  $Tl - 208$  2614 + 580  $keV$  successive gamma hits crystal distance distributions of (a) no z-cut to get the parameter from the best fit of simulation with the data (b) simulation of 4 cm z-cut after applying the fitting parameter to make a prediction of SH in 3 – 3.5  $MeV$  region.

2614.53  $keV$  + 860.56  $keV$  combination  $38.17 \pm 2.79$  counts were estimated. This gives totally  $509.28 \pm 34.45$  counts which is 31% of the background in 3 – 3.5  $MeV$  energy region. In 3.5 – 4  $MeV$  energy region for 2614.53 $keV$  + 860.56 $keV$  combination  $18.29 \pm 1.69$  counts were estimated which is 2.5% of the background. For Period-III Reactor *ON* data taking, the results for  $SH_{pred.}$  based on the prediction for the cosmic rays given in Equation (6.21) and  $Tl - 208$  contribution for energy regions are summarized in Table 6.4.

It can be seen that the estimation method is very powerful and through 3 – 8  $MeV$  the  $ON - SH_{pred.}$  result is better compared to that of  $ON - OFF$  method in terms of residue and their errors which are listed in Tables 5.4 and 5.5.

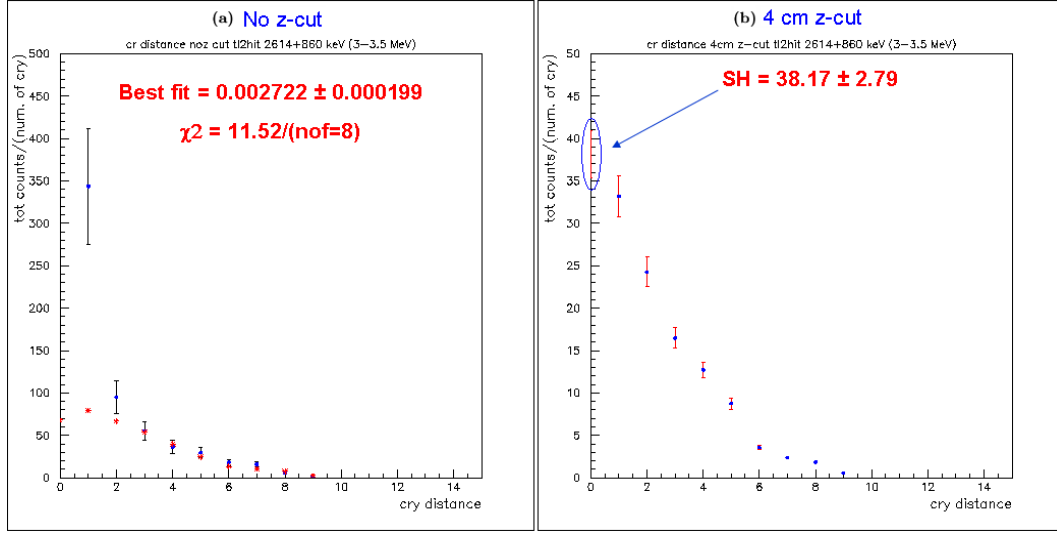


Figure 6.20: For Period-III  $Tl - 208$  2614 + 860 keV successive gamma hits crystal distance distributions of (a) no z-cut to get the parameter from the best fit of simulation with the data (b) simulation of 4 cm z-cut after applying the fitting parameter to make a prediction of SH in 3 – 3.5 MeV region.

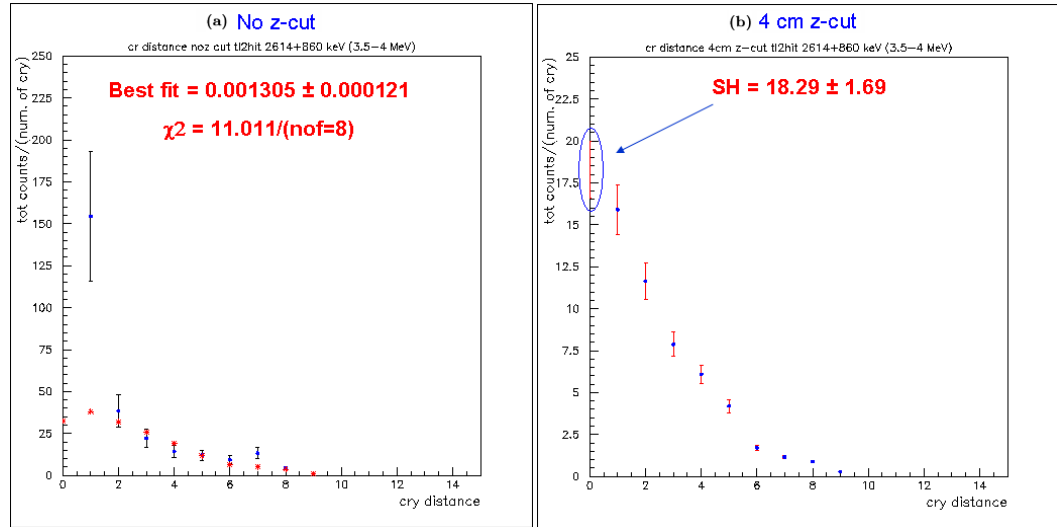


Figure 6.21: For Period-III  $Tl - 208$  2614 + 580 keV successive gamma hits crystal distance distributions of (a) no z-cut to get the parameter from the best fit of simulation with the data (b) simulation of 4 cm z-cut after applying the fitting parameter to make a prediction of SH in 3.5 – 4 MeV region.

Table 6.4: For Period-III the background estimation in Reactor ON due to Cosmic Ray and Tl-208 in 3-8 MeV with 0.5 MeV bin size.

$Energy$ ( $MeV$ )	$ON$ ( $count$ )	$SH_{pred.}$ ( $count$ )	$ON - SH_{pred.}$ $cpd (kg^{-1} \times day^{-1}) \times 10^{-2}$
3.0 – 3.5	$1747 \pm 41.8$	$1641.44 \pm 46.55$	$1.281 \pm 0.759$
3.5 – 4.0	$734 \pm 27.09$	$741.77 \pm 25.08$	$-0.0943 \pm 0.4482$
4.0 – 4.5	$524 \pm 22.89$	$504.32 \pm 20.89$	$0.239 \pm 0.376$
4.5 – 5.0	$356 \pm 18.87$	$368.00 \pm 17.84$	$-0.146 \pm 0.315$
5.0 – 5.5	$263 \pm 16.22$	$270.61 \pm 15.30$	$-0.0924 \pm 0.2707$
5.5 – 6.0	$203 \pm 14.25$	$202.05 \pm 13.22$	$0.01153 \pm 0.2359$
6.0 – 6.5	$175 \pm 13.23$	$175.09 \pm 12.06$	$-0.00114 \pm 0.2173$
6.5 – 7.0	$200 \pm 14.14$	$180.05 \pm 12.01$	$0.242 \pm 0.225$
7.0 – 7.5	$157 \pm 17.53$	$177.00 \pm 11.53$	$-0.243 \pm 0.207$
7.5 – 8.0	$137 \pm 11.70$	$109.90 \pm 9.33$	$0.329 \pm 0.182$

We can check our prediction method by making  $SH$  estimation in  $OFF$  data and performing  $OFF - SH_{pred.}$ . If our estimation procedure is correct the residue and Weinberg angle should be consistent with zero in  $OFF - SH_{pred.}$  subtraction since there is no neutrino production in Reactor  $OFF$  period. For Period-II Reactor  $OFF$  data taking time in 3 – 3.5  $MeV$  energy region, for 2614.53  $keV + 583.19 keV$  combination  $233.63 \pm 27.95$  counts and for 2614.53  $keV + 860.56 keV$  combination  $26.60 \pm 1.54$  counts were estimated. This gives  $260.23 \pm 27.99$  counts totally which is 54% of the background in 3 – 3.5  $MeV$  energy region. In 3.5 – 4  $MeV$  energy region for 2614.53 $keV + 860.56 keV$  combination  $6.91 \pm 0.84$  counts were estimated which is 4.5% of the background. For Period-III  $OFF$  data taking time in 3 – 3.5  $MeV$  energy region, for 2614.53  $keV + 583.19 keV$  combination  $96.79 \pm 7.02$  counts and for 2614.53  $keV + 860.56 keV$  combination  $8.77 \pm 0.63$  counts were estimated. This gives  $105.56 \pm 7.05$

Table 6.5: For Period-II the background estimation in Reactor OFF due to Cosmic Ray and Tl-208 in 3-8 MeV with 0.5 MeV bin size.

$Energy$ ( $MeV$ )	$OFF$ ( $count$ )	$SH_{pred.}$ ( $count$ )	$OFF - SH_{pred.}$ $cpd (kg^{-1} \times day^{-1}) \times 10^{-2}$
3.0 – 3.5	$504 \pm 22.45$	$479.68 \pm 31.41$	$1.084 \pm 1.721$
3.5 – 4.0	$129 \pm 11.36$	$149.82 \pm 11.53$	$-0.928 \pm 0.721$
4.0 – 4.5	$92 \pm 9.59$	$94.00 \pm 9.33$	$-0.0891 \pm 0.5963$
4.5 – 5.0	$61 \pm 7.81$	$65.01 \pm 7.76$	$-0.179 \pm 0.596$
5.0 – 5.5	$43 \pm 6.56$	$47.34 \pm 6.62$	$-0.193 \pm 0.491$
5.5 – 6.0	$32 \pm 5.66$	$32.51 \pm 5.48$	$-0.0226 \pm 0.4153$
6.0 – 6.5	$26 \pm 5.10$	$26.14 \pm 4.92$	$-0.00624 \pm 0.31576$
6.5 – 7.0	$35 \pm 5.92$	$41.25 \pm 5.92$	$-0.279 \pm 0.373$
7.0 – 7.5	$41 \pm 6.40$	$44.67 \pm 6.01$	$-0.0164 \pm 0.3913$
7.5 – 8.0	$40 \pm 6.32$	$38.48 \pm 5.55$	$0.0678 \pm 0.3752$

counts totally which is 33% of the background in 3 – 3.5  $MeV$  energy region. In 3.5 – 4  $MeV$  energy region for 2614.53 $keV$  + 860.56 $keV$  combination  $3.48 \pm 0.32$  counts were estimated which is 5% of the background. For Period-II and Period-III the residue of  $OFF - SH_{pred.}$  subtraction is given in Table 6.5 and Table 6.6, respectively. In both period the residue and Weinberg Angle shown in Figure 7.5 consistent with zero showing that our estimation methods are working quite well.

As a summary the background sources and contributions above 3 MeV range in Period-II and Period-III for Reactor  $OFF$  are summarized in Table 6.7.

Table 6.6: For Period-III the background estimation in Reactor OFF due to Cosmic Ray and Tl-208 in 3-8 MeV with 0.5 MeV bin size.

$Energy$ ( $MeV$ )	$OFF$ ( $count$ )	$SH_{pred.}$ ( $count$ )	$OFF - SH_{pred.}$ $cpd (kg^{-1} \times day^{-1}) \times 10^{-2}$
3.0 – 3.5	$313 \pm 17.69$	$315.51 \pm 15.22$	$-0.159 \pm 1.484$
3.5 – 4.0	$136 \pm 11.66$	$136.25 \pm 10.73$	$-0.0160 \pm 1.008$
4.0 – 4.5	$96 \pm 9.80$	$97.04 \pm 9.17$	$-0.0663 \pm 0.8536$
4.5 – 5.0	$66 \pm 8.12$	$60.92 \pm 7.27$	$0.323 \pm 0.693$
5.0 – 5.5	$52 \pm 7.21$	$49.19 \pm 6.53$	$0.179 \pm 0.619$
5.5 – 6.0	$30 \pm 5.48$	$35.99 \pm 5.59$	$-0.381 \pm 0.498$
6.0 – 6.5	$24 \pm 4.90$	$27.99 \pm 4.93$	$-0.254 \pm 0.442$
6.5 – 7.0	$33 \pm 5.74$	$28.32 \pm 4.88$	$0.298 \pm 0.479$
7.0 – 7.5	$40 \pm 6.32$	$28.20 \pm 4.75$	$0.751 \pm 0.503$
7.5 – 8.0	$27 \pm 5.20$	$16.50 \pm 3.64$	$0.668 \pm 0.404$

Table 6.7: The background sources and their background level in Reactor OFF due to Cosmic Ray, Tl – 208 and Copper in 3-8 MeV.

<i>Reactor OFF</i>				
<i>Period</i>	<i>Period – II</i>		<i>Period – III</i>	
<i>Energy</i> ( $MeV$ )	3 – 5 $MeV$		3 – 5 $MeV$	
	internal Tl – 208 < 0.8%		internal Tl – 208 < 0.6%	
3.0 – 3.5	55% Tl – 208	45% cosmic	30% Tl – 208	70% cosmic
3.5 – 4.0	4.5% Tl – 208	95.5% cosmic	2.5% Tl – 208	97.5% cosmic
4.0 – 6.5	–	~ 100% cosmic	–	~ 100% cosmic
6.5 – 8.0	54% Cu	46% cosmic	47% Cu	53% cosmic

## CHAPTER 7

### RESULTS AND CONCLUSION

Expected event rate for  $\bar{\nu}_e e$  scattering can be written as

$$\begin{aligned} r_{SM}(T) &= \int_{E_\nu} \frac{d\sigma_{SM}}{dT} \frac{d\phi}{dE_\nu} dE_\nu \\ R_{SM} &= \int_T r_{SM}(T) dT = \int_T \int_{E_\nu} \frac{d\sigma_{SM}}{dT} \frac{d\phi}{dE_\nu} dE_\nu dT \end{aligned} \quad (7.1)$$

where  $\phi$  is the neutrino flux,  $E_\nu$  is the energy of neutrino,  $T$  is the recoil electron energy and  $\frac{d\sigma_{SM}}{dT}$  is expected differential cross sections for  $\bar{\nu}_e e$  scattering.

The expected differential cross sections for  $\bar{\nu}_e e$  scattering in Equation (3.4) can be written in terms of Weinberg Angle,  $\sin^2 \theta_W$ , as

$$\frac{d\sigma_{SM}}{dT}(\bar{\nu}_e e) = \frac{G_F^2 m_e}{2\pi} \left\{ \begin{aligned} &4 \sin^4 \theta_W \left[ 1 + \left( 1 - \frac{T}{E_\nu} \right)^2 - \frac{m_e T}{E_\nu^2} \right] \\ &+ 4 \sin^2 \theta_W \left[ \left( 1 - \frac{T}{E_\nu} \right)^2 - \frac{m_e T}{2E_\nu^2} \right] + \left( 1 - \frac{T}{E_\nu} \right)^2 \end{aligned} \right\} \quad (7.2)$$

The event rate  $R$  can be written as

$$R = (\zeta \pm d\zeta) R_{SM} = (\zeta \pm d\zeta) \int_T \int_{E_\nu} \frac{d\sigma_{SM}}{dT} \frac{d\phi}{dE_\nu} dE_\nu dT = A + B \sin^2 \theta_W + C \sin^4 \theta_W \quad (7.3)$$

where  $A$ ,  $B$  and  $C$  can be written as in Equation (7.4). For getting better results one can expect  $\zeta \rightarrow 1$  and  $d\zeta \rightarrow 0$ .

$$\begin{aligned}
A &= \frac{G_F^2 m_e}{2\pi} \int_T \int_{E_\nu} \left(1 - \frac{T}{E_\nu}\right)^2 \frac{d\phi}{dE_\nu} dE_\nu dT \\
B &= \frac{G_F^2 m_e}{2\pi} \int_T \int_{E_\nu} 4 \left[ \left(1 - \frac{T}{E_\nu}\right)^2 - \frac{m_e T}{2E_\nu^2} \right] \frac{d\phi}{dE_\nu} dE_\nu dT \\
C &= \frac{G_F^2 m_e}{2\pi} \int_T \int_{E_\nu} 4 \left[ 1 + \left(1 - \frac{T}{E_\nu}\right)^2 - \frac{m_e T}{E_\nu^2} \right] \frac{d\phi}{dE_\nu} dE_\nu dT \quad (7.4)
\end{aligned}$$

From Equation (7.3) the error for  $\sin^2 \theta_W$  can be obtained as

$$d(\sin^2 \theta_W) = \left( \frac{R_{SM}}{B + 2C \sin^2 \theta_W} \right) d\zeta \quad (7.5)$$

We can use two different methods to get  $\zeta \pm d\zeta$ . We can approximate  $r_{SM}(T)$  to a polynomial  $P(T)$  to get  $\zeta \pm d\zeta$  value from the best fit. Also we can use least-square fit method by defining  $\chi^2$  function to get  $\zeta$  and error  $d\zeta$  as

$$\chi^2 = \sum_{i=1}^{10} \left( \frac{R_i - \zeta R_i^{SM}}{\sigma_i} \right)^2 \quad (7.6)$$

After getting  $\zeta \pm d\zeta$  we can use Equation (7.3) to calculate  $\sin^2 \theta_W$  and Equation (7.5) to calculate the error of  $\sin^2 \theta_W$ .

We can rearrange the differential cross sections of  $\bar{\nu}_e e$  scattering in the Equation (7.2) in terms of  $g_V$  and  $g_A$ , one can obtain an elliptical form of

$$R = (\zeta \pm d\zeta) \times R_{SM} = ax^2 + by^2 + cxy.$$

$$\frac{d\sigma_{SM}}{dT}(\bar{\nu}_e e) = \frac{G_F^2 m_e}{2\pi} \left\{ \begin{array}{l} (g_V + 1)^2 \left[ 1 + \left( 1 - \frac{T}{E_\nu} \right)^2 - \frac{m_e T}{E_\nu^2} \right] \\ + (g_A + 1)^2 \left[ 1 + \left( 1 - \frac{T}{E_\nu} \right)^2 + \frac{m_e T}{E_\nu^2} \right] \\ - (g_V + 1)(g_A + 1) \left[ 2 - 2 \left( 1 - \frac{T}{E_\nu} \right)^2 \right] \end{array} \right\} \quad (7.7)$$

The event rate  $R$  can be written as in terms of  $g_V, g_A$  as in Equation (7.8)

$$\begin{aligned} R &= (\zeta \pm d\zeta) R_{SM} = (\zeta \pm d\zeta) \int_T \int_{E_\nu} \frac{d\sigma_{SM}}{dT} \frac{d\phi}{dE_\nu} dE_\nu dT \\ &= a(g_V + 1)^2 + b(g_A + 1)^2 - c(g_V + 1)(g_A + 1) \end{aligned} \quad (7.8)$$

where a, b and c are given in Equation (7.9).

$$\begin{aligned} a &= \frac{G_F^2 m_e}{2\pi} \int_T \int_{E_\nu} \left[ 1 + \left( 1 - \frac{T}{E_\nu} \right)^2 - \frac{m_e T}{E_\nu^2} \right] \frac{d\phi}{dE_\nu} dE_\nu dT \\ b &= \frac{G_F^2 m_e}{2\pi} \int_T \int_{E_\nu} \left[ 1 + \left( 1 - \frac{T}{E_\nu} \right)^2 + \frac{m_e T}{E_\nu^2} \right] \frac{d\phi}{dE_\nu} dE_\nu dT \\ c &= \frac{G_F^2 m_e}{2\pi} \int_T \int_{E_\nu} \left[ 2 - 2 \left( 1 - \frac{T}{E_\nu} \right)^2 \right] \frac{d\phi}{dE_\nu} dE_\nu dT \end{aligned} \quad (7.9)$$

Using Kuo-Sheng nuclear power plants as a source of  $\bar{\nu}_e$  in the TEXONO Experiment with the 186 kg of CsI(Tl) scintillating crystal in Period-II the measurement was done based on 95.18 days in Reactor *ON* and 48.36 days in Reactor *OFF* data. By using neutrino flux as an input given Figure 3.5 in Chapter-III, for 3 – 8 MeV the expected event rate was calculated as  $R_{SM} = 0.0119703$  and the parameters were obtained as  $A = 0.2424 \times 10^{-2}$ ,  $B = 0.2052 \times 10^{-2}$ ,  $C = 0.1697$  and  $a = 0.04241$ ,  $b = 0.05006$ ,  $c = 0.08277$ .



As shown in Figure 7.1 both polynomial and least-square ( $\chi^2$ ) best fit methods give similar results on the measurement of the event rate. In the  $ON - OFF$  method, the event rate of  $(\zeta \pm d\zeta) \times R_{SM}$  was obtained as  $(1.786 \pm 1.297) \times R_{SM}$  from the least-square ( $\chi^2$ ) fit with  $\chi^2 = 8.09/(nof = 9)$  and corresponding  $\sin^2 \theta_W$  value was obtained as  $0.328 \pm 0.137$  consequently. In addition the  $ON - SH_{pred.}$  given in Table 6.3 the event rate of  $(\zeta \pm d\zeta) \times R_{SM}$  was obtained as  $(1.194 \pm 1.451) \times R_{SM}$  from  $\chi^2$  fit with  $\chi^2 = 6.44/(nof = 9)$  and corresponding  $\sin^2 \theta_W$  value was obtained as  $0.259 \pm 0.153$ . Since we have better errors in the  $ON - SH_{pred.}$  method, we can get better results on the measurement of cross-section and accordingly in  $\sin^2 \theta_W$  value with better error. This results also show that  $ON - SH_{pred.}$  method is more powerful and accurate than  $ON - OFF$  method since  $SH_{pred.}$  is done based on Reactor  $ON$  data itself instead of time limited Reactor  $OFF$  data. As a summary, for Period-II the event rate of  $R(\bar{\nu}_e e)$  and  $\sin^2 \theta_W$  value for  $ON - OFF$  and  $ON - SH_{pred.}$  methods are;

$$\begin{array}{ll}
\text{'ON - OFF' } (\chi^2 = 8.09/9) & \rightarrow 3.0 < E_e < 8.0 \text{ MeV} \\
R(\bar{\nu}_e e) = (1.786 \pm 1.297) \times R_{SM} & \sin^2 \theta_W = 0.328 \pm 0.137 \\
\text{'ON - SH}_{pred.}\text{' } (\chi^2 = 6.44/9) & \rightarrow 3.0 < E_e < 8.0 \text{ MeV} \\
R(\bar{\nu}_e e) = (1.194 \pm 1.451) \times R_{SM} & \sin^2 \theta_W = 0.259 \pm 0.153
\end{array} \tag{7.10}$$

Furthermore, if we combine  $OFF$  and  $SH_{pred.}$ , we can achieve the best estimation on background and we can perform  $ON - BKG$  by combining  $ON - OFF$

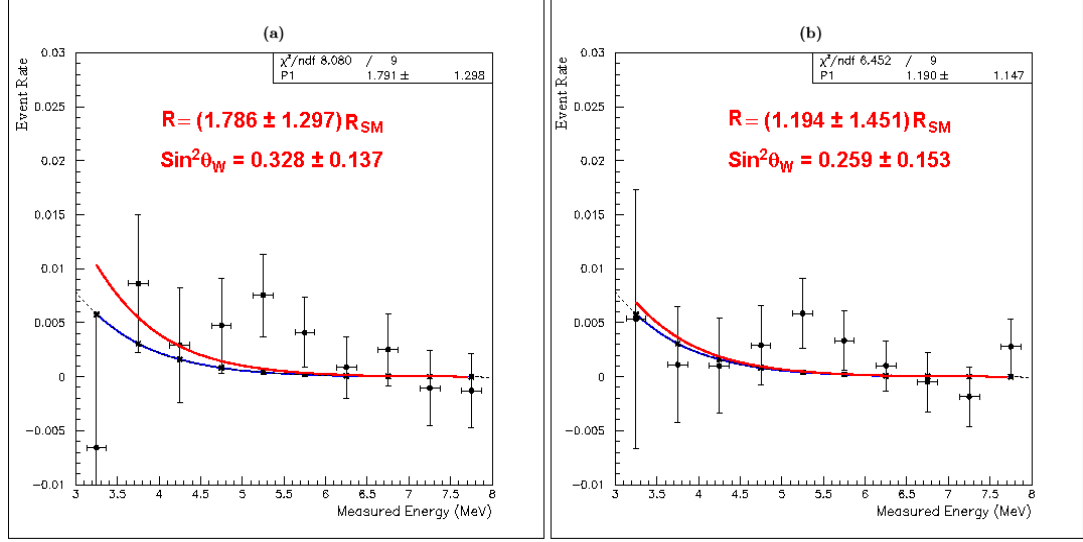


Figure 7.1: In Period-II the measurement of scattering cross section of  $\zeta \pm d\zeta$  for (a) 'ON - OFF' (b) 'ON -  $(SH)_{pred.}$ ' where best fit is shown in red line, blue line corresponds to SM, dash line corresponds to the 5<sup>th</sup> order polynomial fit on SM data.

and  $ON - SH_{pred.}$  residues bin by bin. After performing  $ON - BKG$ , from the best fit we can get the event rate and  $\sin^2 \theta_W$  value afterwards given in Equation (7.11). The  $ON - BKG$  which is combination results of  $ON - OFF$  and  $ON - SH_{pred.}$  for Period-II is shown in Figure 7.2a and the corresponding schematic drawing of the ellipse for  $\bar{\nu}_e e$  scattering cross section in the  $(g_V, g_A)$  plane is shown in Figure 7.2b.

$$\begin{aligned}
 &\text{for PII 'ON - BKG'} && 3.0 < E_e < 8.0 \text{ MeV} \\
 &(\chi^2 = 11.59/9) && \rightarrow \\
 &R(\bar{\nu}_e e) = (1.454 \pm 0.859) \times R_{SM} && \sin^2 \theta_W = 0.291 \pm 0.102 \quad (7.11)
 \end{aligned}$$

Similarly, in Period-III with the 200 kg of CsI(Tl) scintillating crystals the

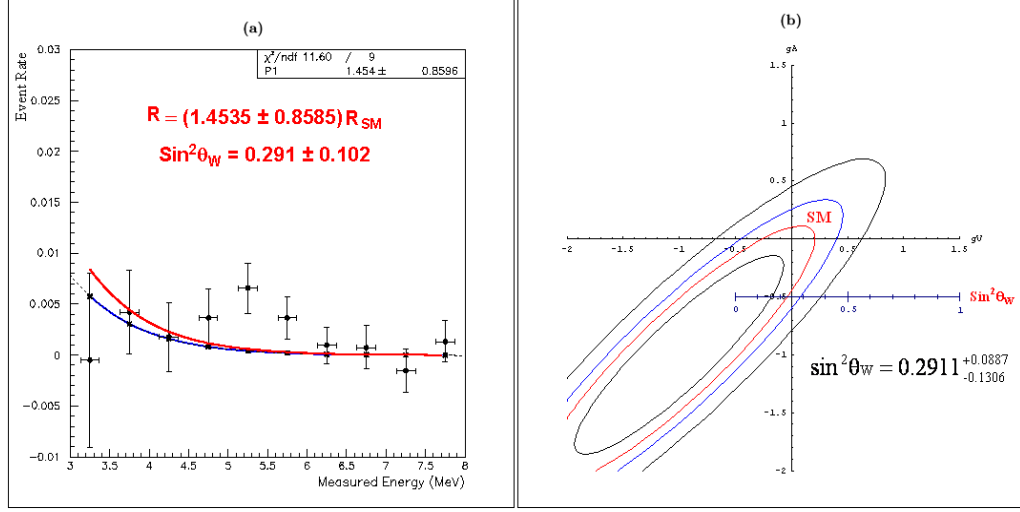


Figure 7.2: In Period-II (a) the measurement of scattering cross section of  $\zeta \pm d\zeta$  for the combination of 'ON-OFF' and 'ON-(SH)<sub>pred.</sub>' where best fit is shown in red line, the blue line corresponds to SM, dash line corresponds to the 5<sup>th</sup> order polynomial fit on SM data and (b) the schematic drawing of the ellips for  $\bar{\nu}_e e$  scattering cross section in the  $(g_V, g_A)$  plane.

measurement was done based on 191.96 days in Reactor *ON* and 36.61 days in Reactor *OFF* data. By using neutrino flux as an input given Figure 3.5 in Chapter-III, for 3 – 8 MeV the expected event rate was calculated as  $R_{SM} = 0.01159$  and the parameters were obtained as  $A = 0.2343 \times 10^{-2}$ ,  $B = 0.1928 \times 10^{-2}$ ,  $C = 0.1647$  and  $a = 0.04117$ ,  $b = 0.04861$ ,  $c = 0.08041$ .

As shown in Figure 7.3 both polynomial and  $\chi^2$  best fit methods give similar results on the measurement of the event rate. In the *ON-OFF* method, the event rate of  $(\zeta \pm d\zeta)R_{SM}$  was obtained as  $(1.278 \pm 1.413)R_{SM}$  from the  $\chi^2$  fit with  $\chi^2 = 10.83/(nof = 9)$  and corresponding  $\sin^2 \theta_W$  value was obtained as  $0.272 \pm 0.179$  consequently. In addition the *ON-SH<sub>pred.</sub>* given in Table 6.4 the

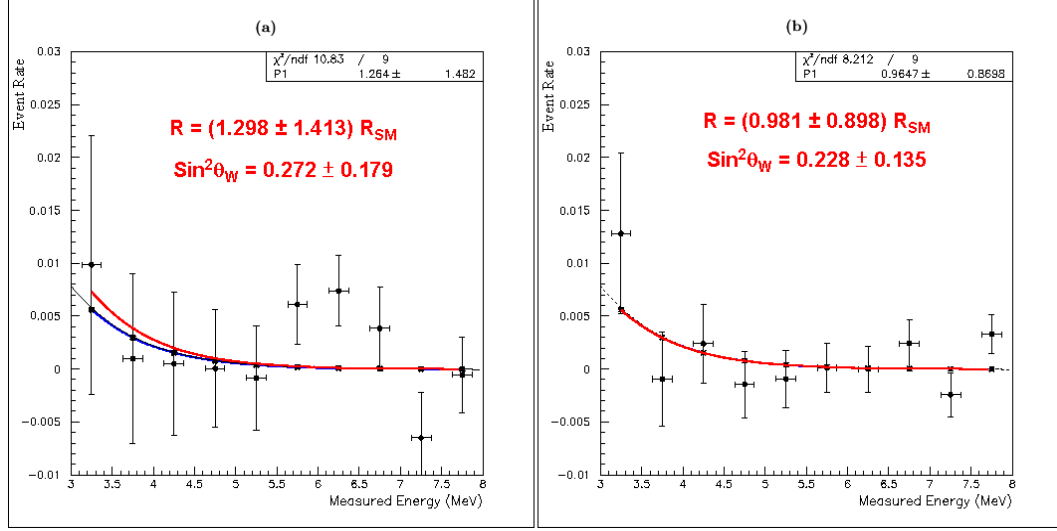


Figure 7.3: In Period-III the measurement of scattering cross section of  $\zeta \pm d\zeta$  for (a) 'ON - OFF' (b) 'ON -  $(SH)_{pred.}$ ' where best fit is shown in red line, blue line corresponds to SM, dash line corresponds to the 5<sup>th</sup> order polynomial fit on SM data.

event rate of  $(\zeta \pm d\zeta) \times R_{SM}$  was obtained as  $(0.981 \pm 0.898) \times R_{SM}$  from the  $\chi^2$  fit with  $\chi^2 = 8.25/(nof = 9)$  and corresponding  $\sin^2 \theta_W$  value was obtained as  $0.228 \pm 0.135$ . Since we have better errors in the  $ON - SH_{pred.}$  method like in Period-II, we have better results on the measurement of cross-section and accordingly in  $\sin^2 \theta_W$  value with better error. As a summary, for Period-III the event rate of  $R(\bar{\nu}_e e)$  and  $\sin^2 \theta_W$  value for  $ON - OFF$  and  $ON - SH_{pred.}$  are;

$$\begin{aligned}
 & \text{'ON - OFF' } (\chi^2 = 10.83/9) & \rightarrow & 3.0 < E_e < 8.0 \text{ MeV} \\
 & R(\bar{\nu}_e e) = (1.298 \pm 1.413) \times R_{SM} & & \sin^2 \theta_W = 0.272 \pm 0.179 \\
 & \text{'ON - } SH_{pred.} \text{' } (\chi^2 = 8.25/9) & \rightarrow & 3.0 < E_e < 8.0 \text{ MeV} \\
 & R(\bar{\nu}_e e) = (0.981 \pm 0.898) \times R_{SM} & & \sin^2 \theta_W = 0.228 \pm 0.135
 \end{aligned} \tag{7.12}$$

Furthermore, like in Period-II if we combine  $OFF$  and  $SH_{pred.}$ , we can achieve the best estimation on background and we can perform  $ON - BKG$  by combining  $ON - OFF$  and  $ON - SH_{pred.}$  residues bin by bin given in Equation (7.13). The combination results of  $ON - OFF$  and  $ON - SH_{pred.}$  for Period-III is shown in Figure 7.4a and the corresponding schematic drawing of the ellipse for  $\bar{\nu}_e e$  scattering cross section in the  $(g_V, g_A)$  plane is shown in Figure 7.4b.

$$\begin{aligned}
&\text{for PIII 'ON - BKG' } && 3.0 < E_e < 8.0 \text{ MeV} \\
&(\chi^2 = 11.88/9) && \rightarrow \\
&R(\bar{\nu}_e e) = (1.062 \pm 0.774) \times R_{SM} && \sin^2 \theta_W = 0.240 \pm 0.111 \quad (7.13)
\end{aligned}$$

For checking our SH prediction method we can also perform  $OFF - SH_{pred.}$  and get the  $SM$  scattering cross section from the best fit. It must be consistent with zero as shown in Figures 7.5a and Figures 7.5b for Period-II and Period-III, respectively. From the Figures it can be seen that there is no excess and Weinberg Angle is consistent with zero for  $OFF - SH_{pred.}$ .

As well as combining Period-II and Period-III results on  $SM$  scattering cross section and  $\sin^2 \theta_W$  value statistically, we can combine the neutrino flux in Period-II and Period-III based on their  $kg \times day$  weighted average to get the total neutrino flux and corresponding parameters. By combining Period-II and Period-III neutrino flux, the expected event rate was calculated as  $R_{SM} = 0.0117254$  and by using Equations 7.4 and 7.9 the parameters for total neutrino flux in  $3 - 8 \text{ MeV}$  were obtained as  $A = 0.2371 \times 10^{-2}$ ,  $B = 0.1972 \times 10^{-2}$ ,  $C =$

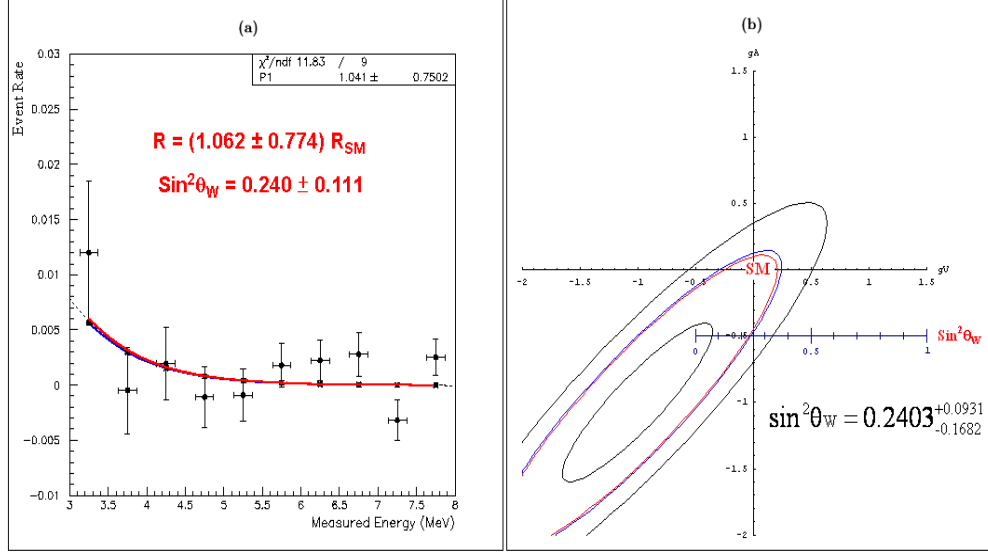


Figure 7.4: In Period-III (a) the measurement of scattering cross section of  $\zeta \pm d\zeta$  for the combination of 'ON - OFF' and 'ON -  $(SH)_{pred.}$ ' where best fit is shown in red line, blue line corresponds to SM, dash line corresponds to the 5<sup>th</sup> order polynomial fit on SM data and (b) the schematic drawing of the ellips for  $\bar{\nu}_e e$  scattering cross section in the  $(g_V, g_A)$  plane.

0.1664 and  $a = 0.04160$ ,  $b = 0.04912$ ,  $c = 0.08123$ . After we achieved the best estimation on background for Period-II and Period-III separately, we can perform combining Period-II and Period-III residues bin by bin. The 'ON - BKG' which is combination results of  $ON - OFF$  and  $ON - SH_{pred.}$  for (Period-II+Period-III) and the corresponding schematic drawing of the ellipse for  $\bar{\nu}_e e$  scattering cross section in the  $(g_V, g_A)$  plane is shown in Figure 7.6a and Figure 7.6b, respectively. As a summary, for (Period-II+Period-III) the event rate of  $R(\bar{\nu}_e e)$  and  $\sin^2 \theta_W$  value for combination of  $ON - OFF$  and  $ON - SH_{pred.}$  are;

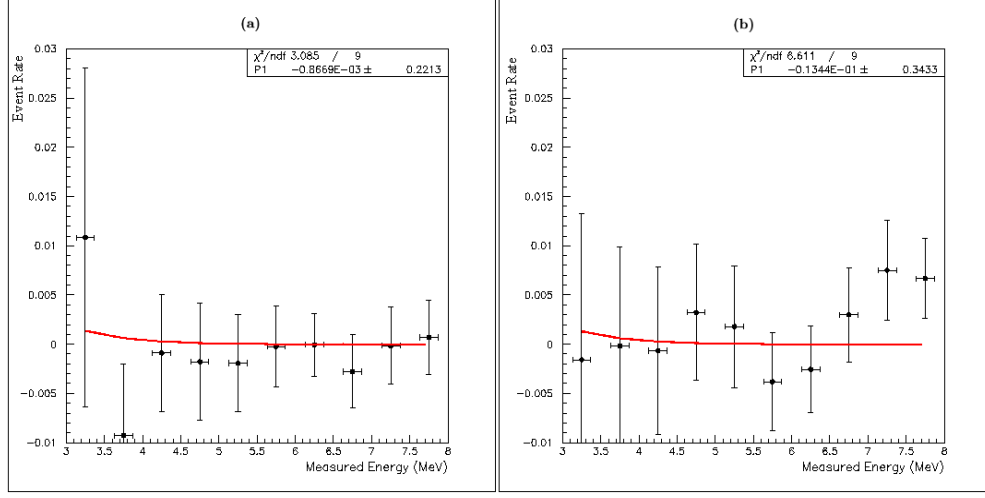


Figure 7.5: The test of  $SH_{pred.}$  method from the best fit in ' $OFF - SH_{pred.}$ ' which is consistent with zero (a) for Period-II (b) for Period-III, showing  $SH_{pred.}$  method is working well.

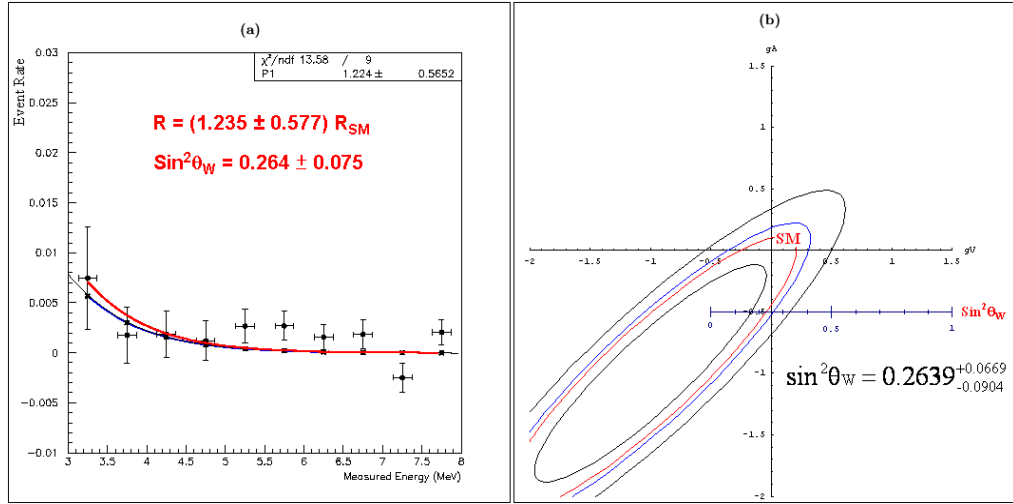


Figure 7.6: (a) the measurement of scattering cross section of  $\zeta \pm d\zeta$  for the combination of ' $ON - OFF$ ' and ' $ON - (SH)_{pred.}$ ' where best fit is shown in red line, blue line corresponds to SM and dash line corresponds to the 5<sup>th</sup> order polynomial fit on SM data and (b) the schematic drawing of the ellips for  $\bar{\nu}_e e$  scattering cross section in the  $(g_V, g_A)$  plane.

$$\begin{aligned}
& \text{from 'ON - BKG'} & 3.0 < E_e < 8.0 \text{ MeV} \\
& (\chi^2 = 13.68/9) & \rightarrow \\
& R(\bar{\nu}_e e) = (1.235 \pm 0.577) \times R_{SM} & \sin^2 \theta_W = 0.264 \pm 0.075 \quad (7.14)
\end{aligned}$$

We can combined the results given in Equation (7.10) and (7.12) for  $ON - OFF$  and  $ON - SH_{pred.}$  seperately for Period-II and Period-III. The combined results only for  $ON - OFF$  and only for  $ON - SH_{pred.}$  are given below and shown in Figure 7.7a and Figure 7.7b, respectively. As a summary, combined results for  $ON - OFF$  and  $ON - SH_{pred.}$  in different combination are listed in Table 7.1. The results are given as a combination of  $ON - OFF$  and  $ON - SH_{pred.}$  seperately for Period-II and Period-III as well as combination of all results.

$$\begin{aligned}
& \text{'ON - OFF' only } (\chi^2 = 11.7/9) & \rightarrow & 3.0 < E_e < 8.0 \text{ MeV} \\
& R(\bar{\nu}_e e) = (1.586 \pm 0.996) \times R_{SM} & & \sin^2 \theta_W = 0.306 \pm 0.112 \\
& \text{'ON - SH}_{pred.}\text{' only } (\chi^2 = 9.3/9) & \rightarrow & 3.0 < E_e < 8.0 \text{ MeV} \\
& R(\bar{\nu}_e e) = (1.059 \pm 0.707) \times R_{SM} & & \sin^2 \theta_W = 0.239 \pm 0.101 \quad (7.15)
\end{aligned}$$

By taking more data as stable and in good condition as Period-II and Period-III, the accuracy of  $\sin^2 \theta_W$  will be improved profoundly statistically alone. By analyzing Period-IV data which is taken from *February* 2006 to *April* 2007 we expect to achieve at least 20% accuracy in the  $\sin^2 \theta_W$  and 33% accuracy in the cross-section measurement statistically alone. For the Period-IV 232  $kg \times day$  data was analyzed and in 3 – 8  $MeV$  about 0.55  $cpd$  ( $kg^{-1} \times day^{-1}$ ) background



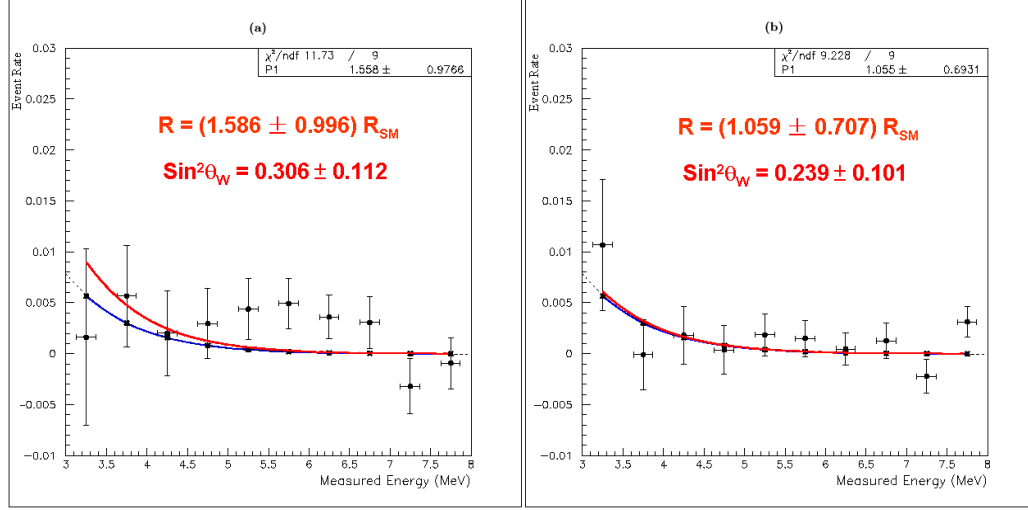


Figure 7.7: The Event Rate and Weinberg Angle for the combination of Period-II and Period-III (a) only  $ON - OFF$  and (b) only  $ON - SH_{pred.}$  methods.

Table 7.1: The summary of the event rate and Weinberg Angle results for Period-II and Period-III including combination of results, horizontal and vertical separately.

	$ON - OFF$	$ON - SH_{pred.}$
Period-II	$(1.786 \pm 1.297) \times R_{SM}$ $\sin^2 \theta_W = 0.328 \pm 0.137$	$(1.194 \pm 1.451) \times R_{SM}$ $\sin^2 \theta_W = 0.259 \pm 0.153$
Period-III	$(1.298 \pm 1.413) \times R_{SM}$ $\sin^2 \theta_W = 0.272 \pm 0.179$	$(0.981 \pm 0.898) \times R_{SM}$ $\sin^2 \theta_W = 0.228 \pm 0.135$
Combined Vertically	$(1.586 \pm 0.996) \times R_{SM}$ $\sin^2 \theta_W = 0.306 \pm 0.112$	$(1.059 \pm 0.707) \times R_{SM}$ $\sin^2 \theta_W = 0.239 \pm 0.101$
Combined Horizontally	$(1.454 \pm 0.859) \times R_{SM}$ $\sin^2 \theta_W = 0.291 \pm 0.102$	$(1.062 \pm 0.774) \times R_{SM}$ $\sin^2 \theta_W = 0.240 \pm 0.111$
Combined All	$(1.235 \pm 0.577) \times R_{SM}$ $\sin^2 \theta_W = 0.264 \pm 0.075$	

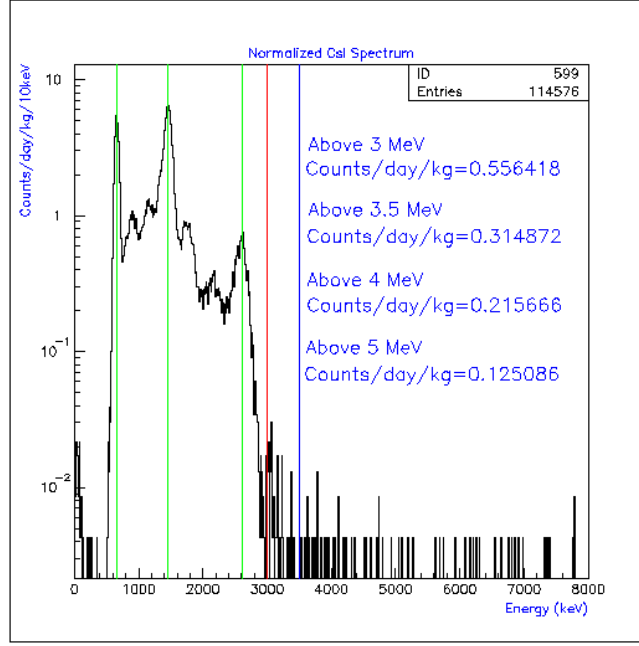


Figure 7.8: The very preliminary results for Period-IV Reactor ON data taking showing that the data is under control and background level as good as previous periods.

level was achieved. The very preliminary spectrum for around 5 *days* Period-IV Reactor ON data illustrated in Figure 7.8. The good energy resolution of known peaks ( $Cs - 137$ ,  $K - 40$  and  $Tl - 208$ ) and flat bakground level above 3 *MeV* shows that Period-IV data is under control and background level is as good as previous periods.

Furthermore, in the future by taking Period-V data and including prediction method as well, we expected to achieve less than 10% accuracy in the  $\sin^2 \theta_W$  and less than 15% accuracy in the cross-section measurement. The accuracy expectations for coming period were obtained by using the same method as

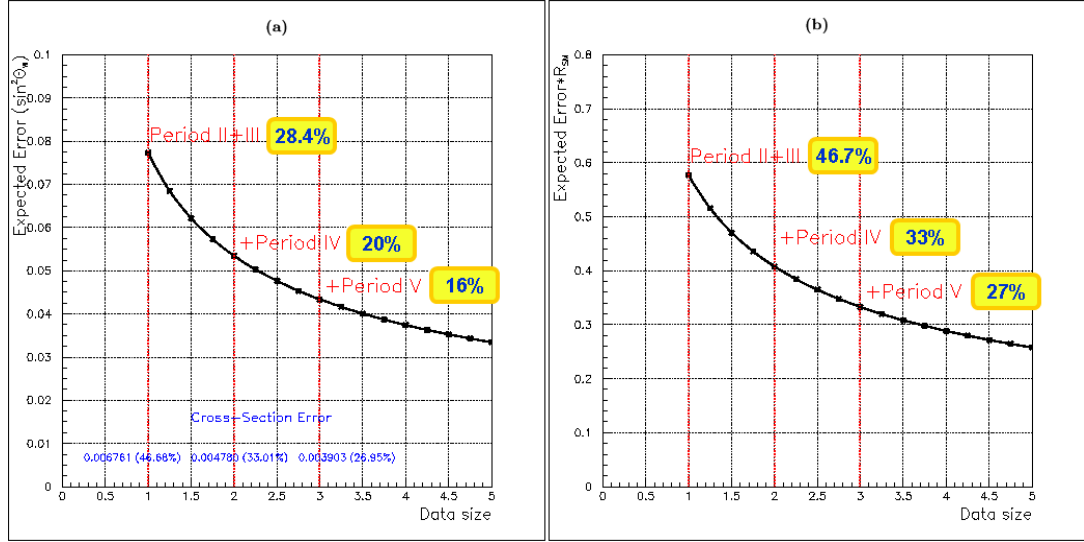


Figure 7.9: Expected accuracy of (a) in the  $\sin^2 \theta_W$  measurement and (b) in the cross section measurement with data size, showing by taking more data as stable and in good condition as before alone, the accuracy will be improved profoundly.

before which is from the best fit by reducing statistical error accordingly with data size. The expected accuracy of  $\sin^2 \theta_W$  and cross-section measurement with data size are illustrated in Figure 7.9a and Figure 7.9b, respectively. There is a linear relationship between the accuracies of  $\sin^2 \theta_W$  and the cross-section, which can be calculated by using Equation (7.5) as 0.1306. From the expectation of accuracies plot shown in Figure 7.10 we can cross check the relationship between accuracies of  $\sin^2 \theta_W$  and the cross-section from the slope which is consistent with the theoretical expectation given in Equation (7.16). As a result, the accuracy relation between  $\sin^2 \theta_W$  and the cross-section can be written in terms

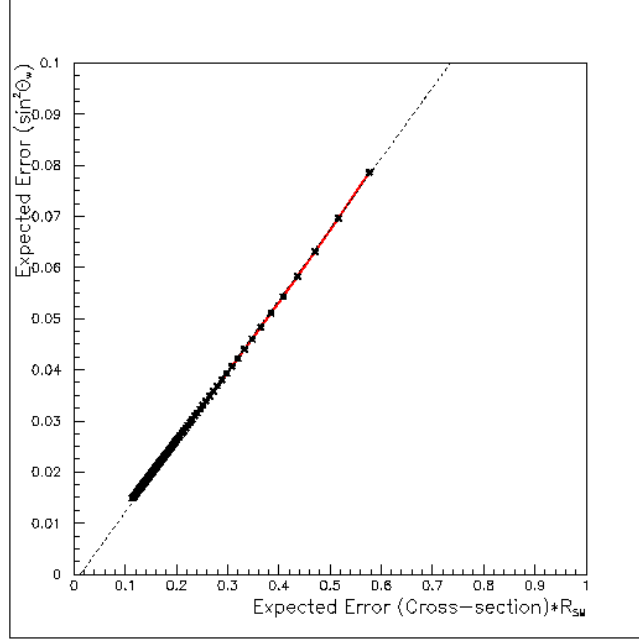


Figure 7.10: The relationship of expected accuracy between  $\sin^2 \theta_W$  and the cross-section obtained from the best fit as before which is linear and totally agree with theoretical value of 0.1306.

of percentage as follows

$$\sigma(\%)_{\sin^2 \theta_W} \simeq 0.60 \times \sigma(\%)_{\bar{\nu}ee} \quad (7.16)$$

Previous reactor experiment situations as well as current status of the TEXONO experiment are listed in Table 7.2. There is no significant measurement of  $\sin^2 \theta_W$  in the low energy region. In the other experiments, the measurement of cross-section is just interpretation since their main physics goal is to study on neutrino magnetic moment. In this study, we attempt to make a measurement of SM antineutrino-electron scattering cross section and thereby Weinberg Angle

Table 7.2: Characteristics of the previous and current  $\bar{\nu}_e - e$  scattering experiments

Experiment	Savannah [58]	Kurchatov [59]	Rovno [60]	NUMU [64, 65]	TEXONO [55]
Target	Plastic Scin.	Fluoro- Carbon Scin.	Si(Li)	CF <sub>4</sub> gas, 5 bar	CsI(Tl) crys.
Fiducial Mass (kg)	15.9	103	37.5	18.4	200
$\phi(\bar{\nu}_e)$ ( $10^{13} cm^{-2} s^{-1}$ )	2.2	0.27	2.0	1.0	0.65
Threshold (MeV)	1.5	3.1	0.6	0.9	3.0
Signal events/day	7.1	0.78	41	10 (expect)	1.0 (expect)
Accuracy of $\sigma(\bar{\nu}_e e)$	29%	53%	49%	50%	46.7%
Accuracy of $\sin^2 \theta_W$	16% $2\sigma$ away	—	—	—	28.4%

$\sin^2 \theta_W$  in untested low energy region. We achieved the world level sensitivities and the best results in the measurement of  $\bar{\nu}_e - e$  scattering cross section and  $\sin^2 \theta_W$  in the low energy region with reactor neutrino.

## REFERENCES

- [1] Respective sections in Review of Particle Physics, Particle Data Group, *J. Phys.* **G 33** (2006), for details and references.
- [2] Proc. of the XXI Int. Conf. on Neutrino Phy. & Astrophys., Paris, ed. J. Dumarchez, *Nucl. Phys.* **B 143** (2005).
- [3] H. T. Wong, "Massive Neutrinos as Dark Matter. An Overview of Experiments", AS-TEXONO/97-04.
- [4] Felix Boehm and Petr Vogel, "Physics of Massive Neutrinos", 2nd Edition, Cambridge University Press (1992).
- [5] O. Lahav and A. R. Liddle, "Review of Particle Physics", *Phys. Letts.* **B 592** (2004) 206;  
Particle Data Group, <http://pdg.lbl.gov/>, May 2007.
- [6] H. T. Wong, "Neutrino Physics and Astrophysics: Highlights", TEXONO/05-05 (2005).
- [7] Kai Zuber, "Neutrino Physics", Series in High Energy Physics, Cosmology and Gravitation IoP Publising (2004).
- [8] H. T. Wong, "The TEXONO Research Program on Neutrino and Astroparticle Physics", *Mod. Phys. Lett.* **A 19** (2004) 1207-1214;  
H. T. Wong and J. Li, "Scintillation Crystal Detector for Low Energy Neutrino Physics", *Mod. Phys. Lett.* **A 15** (2000) 2001.
- [9] S. L. Glashow, *Nucl. Phys.* **22** (1961) 579.
- [10] S. Weinberg, *Phys. Rev. Lett.* **19** (1967) 1264.  
S. Weinberg, *Phys. Rev. Lett.* **27** (1971) 1688.
- [11] A. Salam, Elementary Particle Theory ed N. Swarthohn, Almquist and Wiksell (Stockholm), **p 367** (1968)
- [12] tScholars, <http://www.tscholars.com/encyclopedia/Neutrino>, May 2007.

- [13] J. Chadwick, Verh. der Deutschen Physikalischen Ges. **16** (1914) 383
- [14] K. Winter, “Neutrino Physics”, Cambridge University Press, Cambridge University Press, Cambridge (1991).
- [15] David Griffiths, ”Introduction to Elementary Particles” (1987).
- [16] F. Reines and C. L. Cowan, *Phys. Rev.*, **113** (1958) 273.
- [17] The Reines-Cowan Experiments, Los Alamos Science, Number 25 (1997).
- [18] C. F. Powell, P. H. Fowler, D. H. Perkins, “The Study of Elementary Particles by the Photographic Method”, Pergamon, New York (1959).
- [19] B. Pontecarvo, *Sov. J. Phys.* **10** (1960) 1256.
- [20] G. Danby, et al, *Phys. Rev. Lett.* **9** (1962) 36. See also L. Lederman, Scientific American, (March 1963).
- [21] T. D. Lee and C. N. Yang, *Phys. Rev.*, **104** (1956) 254.
- [22] C. S. Wu et. al., *Phys. Rev. Lett.*, **9** (1962) 36.
- [23] R. L. Garvin, L. M. Ledermann and M. Weinrich, *Phys. Rev.*, **105** (1957) 1415.
- [24] J. D. Bjorken and S. D. Drell “Relativistic Quantum Mechanics”, New York, McGraw-Hill (1964).
- [25] S. Bilenky, and S. T. Petcov, *Rev. Mod. Phys.*, **59** (1987) 671.
- [26] B. M. Bilenky and S.G. Mikhov, “Introduction to Feynman Diagrams and Electroweak Interactions Physics”, Editions Frontiers, France (1994).
- [27] A. Salam, “Elementary Particle Theory”, N. Svartholm, Stockholm (1969).
- [28] S. Weinberg, *Phys. Lett.*, **19** (1967) 1264.
- [29] B. Pontecorvo, *Zh. Eksp. Teor. Fiz.*, **33** (1957) 549.
- [30] Wikipedia, <http://en.wikipedia.org/wiki/Neutrino>, May 2007.
- [31] A. Suziki, “Review of Solar Neutrinos, Atmospheric Neutrinos and Proton Decays”, TOHOKU-HEP-95-03 (3 Oct. 1995).
- [32] K. Nakamura et. al., Kamiokande Collaboration, *Phys. Lett.*, **B 327** (1994) 377.

- [33] J. N. Bahcall, "Neutrino Astrophysics", Cambridge University Press (1989).
- [34] CERN, "<http://choruswww.cern.ch/Public/context.html>", a summary by P.Strolin and A. Ereditato, May 2007.
- [35] B. Kayser, Neutrino Physics as Explored by Flavor Change, Fermilab (2002)
- [36] Athanassopoulos et al, "The Liquid Scintillator Neutrino Detector and LAMPF Neutrino Source", *Nucl. Instrum. Meth.* **A 388** (1997) 149-172, nucl-ex/9605002.
- [37] E. Kearns, in Proc. of the 30th Int. Conf. on High Energy Physics, World Scientific, Singapore, 2001, p 172.
- [38] B. Achkar et al., *Nucl. Phys.* **B 434** (1995) 503;  
M. Apollonio et al., *Phys. Lett.* **B 466** (1999) 415;  
F. Boehm et al., *Phys. Rev.* **D 64** (2001) 112007.
- [39] Y. Ashie et al., Super-Kamiokande Coll., *Phys. Rev. Lett.* **D 71** (2005) 71.
- [40] T. Kajita, presented at the 18th Int. Workshop on Weak Interactions and Neutrinos, Christchurch, January 2002.
- [41] K. Nishikawa, presented at XXth Int. Conf. on Neutrino and Astrophysics, Munich, May 2002,  
E. Aliu et al, K2K Coll., *Phys. Rev. Lett.* **94** (2005) 081802.
- [42] Q. R. Ahmad et al., SNO Coll., *Phys. Rev. Lett.* **89** (2002) 011301;  
B. Aharmim et al., SNO Coll., nucl-ex/0502021 (2005).
- [43] K. Eguchi et al., KamLAND Coll., *Phys. Rev. Lett.* **90** (2003) 021802;  
T. Araki et al., KamLAND Coll., *Phys. Rev. Lett.* **94**, (2005) 081801.
- [44] Daniela Macina, "The CHORUS Experiment", *Nucl. Phys.* **B 48** (Proc. Suppl.) (1996) 183-187.
- [45] E. Eskut et. al., CHORUS Collab., "The CHORUS Experiments to Search for  $\nu_\mu \rightarrow \nu_\tau$  Oscillation", *Nucl. Instrum. Meth.* **A 401** (1997) 7-44.
- [46] E. Eskut et. al., CHORUS Collab., "A Search for  $\nu_\mu \rightarrow \nu_\tau$  Oscillation", *Phys. Lett.* **B 424** (1998) 202.



- [47] E. Eskut et. al., CHORUS Collab., “New results for  $\nu_\mu \rightarrow \nu_\tau$  and  $\nu_e \rightarrow \nu_\tau$  Oscillation ”, *Phys. Lett. B* **497** (2001) 8-22.
- [48] L. Ludovici, *Nucl. Phys. B* **91** (Proc. Suppl.) (2001) 177.
- [49] J. Altegoer, et al., *Nucl. Inst. and Meth. A* **404** (1998) 96.
- [50] P. Astier, et al., *Nucl. Phys. B* **605** (2001) 3,  
P. Astier et al., *Nucl. Phys. B* **611** (2001) 3.
- [51] E. Eskut, et al., CHORUS Collab., *Phys. Lett. B* **503** (2001) 1-9.
- [52] B. Achkar et al., *Nucl. Phys. B* **434** (1995) 503;  
M. Apollonio et al., CHOOZ Coll., *Phys. Rev. Lett. B* **466** (1999) 415;  
F. Boehm et al., *Phys. Rev. D* **64** (2001) 112007.
- [53] Dayabay, <http://dayawane.ihep.ac.cn/docs/experiment.html>, May 2007.
- [54] N. Schmitz, NeutrinoPhysik, Stuttgart: Teubner (1997).
- [55] H. B. Li et al., ”A CsI(Tl) scintillating crystal detector for the studies of low-energy neutrino interactions”, *Nucl. Instr. and Meth. A* **459** (2001) 93-107.
- [56] H. T. Wong, et al., ”Search of Neutrino Magnetic Moments with a High-Purity Germanium Detector at the Kuo-Sheng Nuclear Power Station”,  
H. T. Wong, et al, TEXONO Collaboration, *Phys. Rev. D* **75**, 012001 (2007).
- [57] B. Achkar et al., Bugey Collaboration, *Phys. Lett. B* **374** (1996) 243.
- [58] F. Reines, H. S. Gurr, H. W. Sobel, ”Detection of  $\bar{\nu}_e - e$  Scattering”, *Phys. Rev. Lett.* **37** (1976) 315.
- [59] G. S. Vidyakin et al., *JETP Lett.* **55** (1992) 206.
- [60] A. I. Derbin et al., *JETP Lett.* **57** (1993) 796.
- [61] T. L. Jenkins, F. E. Kinard, F. Reines, *Phys. Rev.* **185** (1969) 1599.
- [62] G. S. Vidyakin et al., *JETP Lett.* **49** (1988) 151,  
G. S. Vidyakin et al., *JETP Lett.* **51** (1990) 279.
- [63] P. Vogel and J. Engel, *Phys. Rev. D* **39** (1989) 3378,  
B. Kayser et al., *Phys. Rev. D* **20** (1979) 87.

- [64] C. Brogini et al., *Nucl. Inst. and Meth.* **A 311** (1992) 319.
- [65] C. Amsler et al., *Nucl. Inst. and Meth.* **A 396** (1997) 115.
- [66] H. B. Li and H. T. Wong, "Sensitivities of low energy reactor neutrino experiments", *J. Phys. G: Nucl. Part. Phys.* **28** (2002) 1453, and references therein.
- [67] H. T. Wong, et al., "Highlights of the TEXONO Research Program on Neutrino and Astroparticle Physics", Proceedings of the Int. Symp. on Neutrino and Dark Matter in Nucl. Phys. (NDM03), Nara, Japan (2003).
- [68] H. T. Wong, "Low energy neutrino physics at the Kuo-Sheng Reactor Neutrino Laboratory at Taiwan", *Nucl. Phys.* **B** (Proc. Suppl.) **138** (2005) 333-336.
- [69] B. R. Davis et al., *Phys. Rev.* **C 19** (1979) 2259;  
P. Vogel et al., *Phys. Rev.* **C 24** (1981) 1543;  
H. V. Klapdor and J. Metzinger, *Phys. Rev. Lett.* **48** (1982) 127;  
H. V. Klapdor and J. Metzinger, *Phys. Rev. Lett.* **B 112** (1982) 22.
- [70] K. Shreckenbach et al., *Phys. Lett.* **B 160** (1980) 325;  
A. A. Hahn et al., *Phys. Lett.* **B 218** (1989) 365.
- [71] B. Xin, et al., "Production of electron neutrinos at nuclear power reactors and the prospects for neutrino physics", TEXONO Coll., *Phys. Rev.* **D 72** (2005) 012006.
- [72] FISC/SOF Ver 1.0, W. S. Tong, 08-4-MAN-036-001-1.1, Institute of Nuclear Energy Research (2001);  
FISSRATE Ver 2.0, W. S. Kuo, 08-4-MAN-036-002-1.0, Institute of Nuclear Energy Research (2001).
- [73] COSMO-3 Ver 4.84, Malte Edenius et al., STUDSVIK/SOA-94/9, Studsvik Scanspower (1994);  
SIMULATE-3 Ver 6.07.08, Lorne Covington et al., STUDSVIK/SOA-95/15 Rev. 2, Studsvik Scanspower (2001).
- [74] TEXONO, <http://hepmail.phys.sinica.edu.tw/~texono>, May 2007.
- [75] H.B. Li et al., "Limits on the Electron Neutrino Magnetic Moment from Kuo-Sheng Reactor Experiment", *Phys. Rev. Lett.* **90** (2003) 13.

- [76] W. P. Lai, et al., "The Electronics and Data Acquisition Systems of a CsI(Tl) Scintillating Crystal Detector for Low Energy Neutrino Experiment", *Nucl. Instr. and Meth.* **A 465** (2001) 550-565.
- [77] Q. Yue, et al., "Effective Dynamic Range in Measurements with Flash Analog-to-Digital Converter", *Nucl. Instr. and Meth.* **A 511** (2003) 408-416.
- [78] Y. Liu, et al., "Studies of prototype CsI(Tl) crystal scintillators for low-energy neutrino experiments", *Nucl. Instr. and Meth.* **A 482** (2002) 125-143.
- [79] H. T. Wong, et al., "Prospects of Scintillating Crystal Detector in Low-Energy Low-Background Experiments", *Astroparticle Phys.* **14** (2000) 141-152.
- [80] H. T. Wong, et al., "Highlights of the TEXONO Research Program on Neutrino and Astroparticle Physics", hep-ex/0307001, Proceedings of the Int. Symp. on Neutrino and Dark Matter in Nucl. Phys. (NDM03), Nara, Japan (2003).
- [81] S. C. Wu, et al., "Near Threshold pulse shape discrimination techniques in scintillating CsI(Tl) crystals", *Nucl. Instr. and Meth.* **A 523** (2004) 116-125.
- [82] C. L. Morris, et al., *Nucl. Instr. and Meth.* **A 299** (1990) 281.
- [83] Y. F. Zhu et al., "Measurement of the intrinsic radiopurity of  $^{137}\text{Cs}/^{235}\text{U}/^{238}\text{U}/^{232}\text{Th}$  in CsI(Tl) crystal scintillators", *Nucl. Instr. and Meth.* **A 557** (2006) 490-500.
- [84] Evaluated Nuclear Structure Data File (ENSDF), <http://www.nndc.bnl.gov/ensdf/>, May 2007.
- [85] L. C. Biedenharn and M. E. Rose, "Theory of Angular Correlation of Nuclear Radiations", *Rev. Mod. Phys.*, **25** (1953) 729;  
S. P. Llyod, "Explicit  $\gamma - \gamma$  Angular Correlation", *Phys. Rev.* **83** (1951) 716.
- [86] E. Segre, Editor, Experimental Nuclear Physics, Volume III, "Gamma Rays", p373 (1959).

## CURRICULUM VITAE

### PERSONAL INFORMATION

**Surname, Name :** Deniz, Muhammed

**Phone:** + 90 312 321 69 72

**Fax:** +90 312 210 1281

**email:** deniz.phys.sinica.edu.tw

Middle East Technical University

Faculty of Art and Science, Department of Physics

TR-06531 Ankara, Turkey

### EDUCATION

Degree	Institution	Year of Graduation
M. S.	METU, Department of Physics	Sept. 2000
B. S.	METU, Department of Physics	Jan. 1998

**Thesis:** "White Kink Background in the CHORUS Experiment ", METU – CERN, Geneva (2000)

**Project:** Parity Violation (1996-1997) and Nuclear Anapole Moment (1997-1998)

### PUBLICATIONS

1. "Search for Axions from the Kuo-Sheng Nuclear Power Reactor with a High-Purity Germanium Detector", C. M. Chang, et al., TEXONO Collaboration, Phys. Rev. D 75, 052004 (2007).
2. "Search of Neutrino Magnetic Moments with a High-Purity Germanium Detector at the Kuo-Sheng Nuclear Power Station", H. T. Wong, et al., TEXONO Collaboration, Phys. Rev. D 75, 012001 (2007).
3. "Measurement of the Intrinsic Radiopurity of Cs-137/U-235/U-238/Th-232 in CsI(Tl) Scintillators", Y.F.Zhu, et al., TEXONO Collaboration, Nucl. Instrum. Methods A 557, 490 (2006).

## CONFERANCES & SEMINAR PRESENTATIONS

1. Participate in 20th Spring School on Particle and Fields , National Taiwan University (NTU), Taipei, Taiwan, April 1-4 2007.
2. “Measurement of Neutrino-Electron Scattering Cross-Section, Status Report”, The Physical Society of Republic of China (PSRoC), National Central University (NCU), Taipei, Taiwan, January 23 – 25, 2007.
3. Participate in the meeting of International Symposium on Neutrino Physics and Neutrino Cosmology, The Chinese University of Hong Kong (CUHK), Hong Kong, China January 8 – 10, 2007.
4. “Background Understanding and Suppression of the CsI(Tl) Experiment to Study Neutrino-Electron Scattering”, 1st Sino-Korean Workshop on Dark Matter Search, Beijing, China, Oct. 11 - 13, 2006.
5. “Study of Neutrino-Electron Scattering with CsI(Tl) Crystal Scintillator”, 2006 Workshop on the Underground Experiment at Yangyang, an extension of TEXONO – KIMS (The Korea Invisible Mass) collaboration meeting, Phoenix Park, Korea, February 6 – 8, 2006
6. “Study of Neutrino-Electron Scattering with a Fine-Grained CsI(Tl) Scintillating Crystal Detector”, The Physical Society of Republic of China (PSRoC), National Taiwan University (NTU), Taipei, Taiwan, January 16 – 18, 2006.
7. Participate in the meeting of 3rd. International Conference on Flavor Physics, National Central University (NCU), Chung-Li, Taiwan October 3 – 8, 2005.
8. Participate in the 16th meeting of “Consultative Committee for Ionizing Radiation CCRI (I) at Bureau International des Poids et Mesures (BIPM), Paris, France, May 21 – 24, 2003.
9. Participate in “Summer School Lectures and Conferances, CERN, Geneva, Switzerland, July 1999 – January 2000.

## TECHNICAL EXCURSIONS

1. Institute of High Energy Physics (IHEP), Beijing China, October, 2006.
2. China Institute of Atomic Energy (CIAE), Beijing, China, October, 2006.

## **RESEARCH EXPERIENCE**

1. Visiting Scholar, The TEXONO Collaboration, Institute of Physics, Academia Sinica (AS), Taipei, Taiwan (2004 – 2007).
2. Researcher, The Scientific and Technical Research Council of Turkey (TUBITAK), National Metrology Institute of Turkey (UME), Kocaeli, Turkey (2002 – 2004).
3. Researcher, The Scientific and Technical Research Council of Turkey (TUBITAK), National Research Institute of Electronics and Cryptology (UEKAE), Kocaeli, Turkey (2001 – 2002).
4. Visiting Scholar, The CHORUS Collaboration, CERN, Geneva, Switzerland (1999 – 2000).

## **FIELD OF INTEREST**

Experimental and theoretical/phenomenological studies on high energy and particle physics, neutrino physics, nuclear physics and detector systems.

## **LANGUAGES**

Turkish, English

## **COMPUTER SKILLS**

Windows, Office Programs, UNIX, Linux; C++, FORTRAN, Mathematica, PAW, Root, GEANT